

UNIVERSITÀ DEGLI STUDI DI CAGLIARI

Study of the Performances of the Muon Arm Slat  
Chambers in ALICE.

Tesi di Dottorato di Ricerca  
di  
Elisabetta Siddi

Tutori

Prof. Sergio Serchi

Dott. Corrado Cicalò

Contro-relatore

Prof. Yves Le Bornec

XIV CICLO

Anni Accademici 1998-2001



*In the fabrication and operation of a chamber people seem to use a mixture of competence, technical skill and magic rites, of the kind "I do not know why I'm doing this but somebody told me to do so."*

*F.Sauli [Sau77]*



# Contents

<b>Acknowledgements</b>	<b>1</b>
<b>Introduction</b>	<b>5</b>
<b>1 Quark Gluon Plasma</b>	<b>7</b>
1.1 MIT Bag Model . . . . .	8
1.1.1 QGP at high temperatures . . . . .	9
1.1.2 QGP at high baryonic density . . . . .	10
1.2 Lattice QCD . . . . .	12
1.3 How to study QGP . . . . .	15
1.3.1 Collision centrality . . . . .	17
1.3.2 Initial energy density . . . . .	18
1.3.3 System temperature . . . . .	19
1.4 Thermal dileptons . . . . .	21
1.5 Strangeness enhancement . . . . .	22
1.6 Charmonia suppression . . . . .	25
1.7 Have we found the QGP? . . . . .	30
1.8 The present (RHIC) and the future (LHC) . . . . .	31
<b>2 The ALICE experiment</b>	<b>33</b>
2.1 The ALICE detector . . . . .	34
2.2 The central barrel . . . . .	36
2.2.1 Inner Tracking System (ITS) . . . . .	36
2.2.2 Time Projection Chamber (TPC) . . . . .	38
2.2.3 Transition Radiation Detector (TRD) . . . . .	39
2.2.4 Time Of Flight (TOF) . . . . .	39
2.2.5 High Momentum Particle Identification Detector (HMPID) . . . . .	40
2.2.6 Photon Spectrometer (PHOS) . . . . .	40
2.3 The forward detectors . . . . .	40
2.3.1 Photon Multiplicity Detector (PMD) . . . . .	41

2.3.2	Zero Degree Calorimeters (ZDC)	42
2.4	The forward dimuon spectrometer	42
2.4.1	The absorbers	43
2.4.2	Dipole magnet	45
2.4.3	Trigger chambers	45
2.4.4	V0 detector	46
2.4.5	Tracking chambers	46
<b>3</b>	<b>ALICE tracking chambers</b>	<b>49</b>
3.0.6	Number of hits and trigger rates	49
3.0.7	Mass resolution	51
3.0.8	Required detector performances	52
3.0.9	Detector choice	55
3.1	Gaseous ionization detectors	56
3.1.1	Energy loss in thin detectors	56
3.1.2	Primary and total ionization	57
3.1.3	Drift of charges in gas	59
3.1.4	Avalanche formation	63
3.2	Multiwire proportional chambers	65
3.2.1	Operating principles	65
3.2.2	Choice of the filling gas	69
3.2.3	Readout methods	70
<b>4</b>	<b>The Muon Arm Tracking System</b>	<b>71</b>
4.1	CSC's geometrical parameter	71
4.2	Station 1 and 2	73
4.3	Station 3, 4 and 5	74
4.3.1	Slat structure	78
4.3.2	Strip sizes	81
4.3.3	Special slats	84
4.3.4	Ghost hits	84
4.4	Readout electronics	86
4.4.1	GASSIPLEX	88
4.4.2	MANAS-16	91
4.4.3	The test electronics	91
4.4.4	The final readout system: MANU	94
<b>5</b>	<b>Slat chamber optimization</b>	<b>99</b>
5.1	Gain dependence on mechanical tolerances	100
5.1.1	Anode wires	101
5.1.2	Cathode planes planarity	105

5.1.3	HV system . . . . .	106
5.2	Edge wires . . . . .	107
5.3	Electric field near the spacer . . . . .	113
5.4	Conclusions . . . . .	119
<b>6</b>	<b>Study of a large CSC prototype</b>	<b>123</b>
6.1	Prototype characteristics . . . . .	123
6.1.1	Cathode planes . . . . .	123
6.1.2	Carbon fiber planes . . . . .	127
6.1.3	Insulating foils . . . . .	127
6.1.4	Anode wires . . . . .	127
6.1.5	Spacers . . . . .	128
6.2	Assembly procedure . . . . .	128
6.2.1	Gluing . . . . .	128
6.2.2	Wires soldering . . . . .	130
6.2.3	Detector cleaning . . . . .	132
6.2.4	Detector sealing . . . . .	132
6.2.5	Checks on mechanical features . . . . .	133
6.3	Test at CERN PS . . . . .	134
6.3.1	Experimental set-up . . . . .	134
6.3.2	The readout system . . . . .	135
<b>7</b>	<b>Data analysis</b>	<b>137</b>
7.1	Results . . . . .	137
7.1.1	Pedestal study . . . . .	137
7.2	Study of bending and non bending plane response . . . . .	142
7.2.1	Bending plane . . . . .	142
7.2.2	Non bending plane . . . . .	147
7.3	Software alignment of silicon detectors . . . . .	147
7.3.1	Position reconstruction . . . . .	152
7.4	Efficiency . . . . .	153
7.5	Estimation of spatial resolution and event selection . . . . .	161
7.5.1	Bending plane resolution . . . . .	163
7.5.2	Non bending plane resolution . . . . .	166
7.6	Cross talk effects . . . . .	167
7.7	Summary . . . . .	170
<b>8</b>	<b>A prototype with large size strips</b>	<b>175</b>
8.1	Prototype characteristics . . . . .	175
8.1.1	Cathode planes . . . . .	176
8.1.2	Sandwich panels . . . . .	181

8.1.3	Insulating foils . . . . .	181
8.1.4	Anode wires . . . . .	181
8.1.5	Spacers . . . . .	181
8.1.6	Assembly and first checks on prototype . . . . .	182
8.2	Test with $^{90}\text{Sr}$ source . . . . .	182
8.3	Data analysis . . . . .	184
8.3.1	Electronics noise . . . . .	184
8.4	Test with source setup . . . . .	186
8.4.1	Charge distribution . . . . .	186
8.4.2	Number of hits . . . . .	194
8.5	Event selection and efficiency study . . . . .	194
8.6	Gas study . . . . .	201
8.7	Main results of the test at CERN PS (June 2001) . . . . .	201
8.8	Summary . . . . .	208
<b>9</b>	<b>Last results and conclusions</b>	<b>211</b>
9.1	Study of the noise . . . . .	212
9.2	Bending plane performances . . . . .	213
9.2.1	Gain dependence on position . . . . .	213
9.2.2	Resolution for inclined tracks . . . . .	215
9.3	Conclusions and perspectives . . . . .	215



# List of Figures

1.1	<i>Phase transition originated by a high temperature and/or a high baryonic number density. . . . .</i>	9
1.2	<i>Phase diagram of nuclear matter. . . . .</i>	11
1.3	<i>Energy density in units of <math>T^4</math> for QCD with 3 dynamical light quark flavors, extrapolated to zero quark mass and to the continuum. . .</i>	13
1.4	<i>Phase transition for a <math>16^3 \times 4</math> lattice. . . . .</i>	14
1.5	<i>Simplified picture of Pb-Pb collisions. . . . .</i>	16
1.6	<i>Time evolution of fireball. . . . .</i>	16
1.7	<i>Schematic view of a central (left) and peripheral (right) nucleus-nucleus collision. . . . .</i>	17
1.8	<i>Correlation between particle mass and <math>m_T</math> spectra inverse slope <math>T</math> for Pb-Pb collisions. . . . .</i>	20
1.9	<i>Inclusive <math>e^+e^-</math> mass spectra obtained from the '95 and '96 analysis. The data are compared to the sum of the expected contributions from hadron decays [Len99]. . . . .</i>	22
1.10	<i>Inclusive <math>e^+e^-</math> invariant mass spectrum at 40 AGeV compared to the expectations from know hadronic souces in heavy ion collisions (left) and to several model calculations (right) [App01]. . . . .</i>	23
1.11	<i>Hadrons and hyperon yields relative to p-Be collisions as a function of participant nucleons from WA97 for all measured particle (closed symbols) and from NA57 for <math>\Xi^-</math> and <math>\Xi^+</math> (open symbols) [Eli01]. .</i>	24
1.12	<i>Debye radius as a function of <math>T/T_c</math>. The lines correspond to the critical Debye radius for different charmonium states. . . . .</i>	26
1.13	<i><math>J/\Psi</math> cross section per nucleon-nucleon collisions as a function of the AB product of the projectile and target atomic mass numbers. .</i>	27
1.14	<i>The ratio <math>J\Psi/DY</math> as a function of the energy released in the Zero Degree Calorimeter is shown. A two step-pattern, foreseen for a deconfinement scenario, is visible ( [Arn00], [Abr01]). . . . .</i>	28
1.15	<i><math>J/\Psi/DY</math> ratio as a function of <math>E_T</math>. The Pb-Pb data are compared to several theoretical calculations. . . . .</i>	29
2.1	<i>View of LHC accelerator. . . . .</i>	34

2.2	General layout of ALICE experiment. . . . .	37
2.3	Forward dimuon spectrometer lateral view. . . . .	44
3.1	Number of hits per unitary area, for the five tracking Stations and the first trigger Station, versus Station radius [MUOAD]. . . . .	50
3.2	Mass spectrum for the $\Upsilon$ -family. The lower curve represents the muons coming from open beauty decays [ALIAD]. . . . .	52
3.3	Muon Arm schematic view in the yz plane. The tracking Stations 1 and 2 are placed before the magnet, the Station 3 is inside the dipole and the last two are located before the filter. The muon deflection is visible. . . . .	53
3.4	Mass resolution, in the $\Upsilon$ region, as a function of tracking chamber spatial resolution [MUO]. . . . .	53
3.5	Mass resolution, in the $\Upsilon$ mass region, as a function of each tracking chamber thickness [MUO]. . . . .	54
3.6	Energy loss distribution for a thin absorber. . . . .	58
3.7	Ion mobility vs $E$ , for a gas mixture made by Ar 80 % and CO <sub>2</sub> 20 %, at normal conditions. . . . .	60
3.8	Drift electron velocity vs $E$ , for a gas mixture made by Ar 80 % and CO <sub>2</sub> 20 %, at normal conditions. . . . .	61
3.9	Diffusion coefficients (transverse, in dark grey; longitudinal, in light grey) vs $E$ , for a gas mixture made by Ar 80 % and CO <sub>2</sub> 20 %, at normal conditions. . . . .	62
3.10	Townsend coefficient (in light grey) and attachment coefficient (in dark grey) as a function of the electric field, for a gas mixture made by Ar 80 % and CO <sub>2</sub> 20 %, at normal conditions. . . . .	64
3.11	Electric field lines in a multiwire proportional chamber. The numbers in the field lines refer to the potential value. . . . .	66
3.12	Electron drift lines from a particle crossing the chamber. . . . .	67
3.13	Electric field shape near a wire: the field is radial. . . . .	68
4.1	Schematic view of the Cathode Strip Chamber geometrical parameters. . . . .	72
4.2	Station 1 and 2 layout. . . . .	74
4.3	General design of a Station 1 quarter. The milled Rohacell layer and some connectors are visible. . . . .	75
4.4	Strip sizes (top) and occupancy level as a function of the radius (bottom) for both chambers 1 (full line) and 2 (dashed line) of Station 1. . . . .	76

4.5	Strip sizes (top) and occupancy level as a function of the radius (bottom) for both chambers 1 (full line) and 2 (dashed line) of Station 2. . . . .	77
4.6	Definition of $\alpha$ (a) and $\theta$ (b) angles. . . . .	78
4.7	Standard slat design. The upper and lower PCB regions host the electronics, the squared ones represent the active area. On the right, a slat cross section is displayed [Ors01]. . . . .	79
4.8	Slat overlapping in Station 3 [Ors01]. . . . .	80
4.9	Occupancy level as a function of the radius for both chambers 1 (full line) and 2 (dashed line) of the last three Stations. . . . .	82
4.10	Schematic view of a chamber of Station 3, 4, and 5 respectively with the different strip densities. . . . .	83
4.11	Half moon slat needed for the Station 3 (chamber 5) [Ors01]. . . . .	84
4.12	Round shaped slat for Station 3 (chamber 5) [Ors01]. . . . .	85
4.13	Round shaped slats for Stations 4 and 5 [Ors01]. . . . .	85
4.14	Ghost hits originated by two true hits. . . . .	86
4.15	Correlation between charges induced in bending and non bending plane. . . . .	87
4.16	Ratio of the charges induced in bending and non bending plane. . . . .	87
4.17	GASSIPLEX functional blocks. . . . .	89
4.18	Timing of the GASSIPLEX signals. . . . .	90
4.19	Representation of a single MANAS-16 channel. . . . .	91
4.20	Top side view of GAS64. The four GASSIPLEX chips are shown. . . . .	93
4.21	Schematical view of MANU architecture (top) and top side view of MANU345 (bottom). . . . .	96
4.22	Bus LVTTTL and LVDS connection between PCBs. . . . .	97
5.1	Exploded view of a CSC: from center to top (or bottom) the anode wire frame, the PCB planes and the carbon fiber panels are shown. . . . .	99
5.2	Gain variation as a function of High Voltage. . . . .	101
5.3	Enlarged view of a 20 $\mu\text{m}$ gold plated wire. The pictures (4500 enlargements on top, 1500 on bottom) show a good uniformity in gold coating. . . . .	103
5.4	Gain variation as a function of wire diameter variation. . . . .	104
5.5	Gain variation as a function of gap variation. . . . .	105
5.6	Gain variation as a function of HV variation. . . . .	106
5.7	Gain value near the border (only the first seven 20 $\mu\text{m}$ wires are shown). In the x axis the wire number is displayed. Wire zero is the closest to the end of the chamber. . . . .	108
5.8	Gain value near the border (one 50 $\mu\text{m}$ edge wire). . . . .	109
5.9	Gain value near the border (two 70 $\mu\text{m}$ edge wires). . . . .	110

5.10	Gain behaviour as a function of edge wire diameter, using only one edge wire. . . . .	111
5.11	Gain behaviour as a function of 2 edge wires diameter. . . . .	112
5.12	Gain behaviour as a function of 3 edge wires diameter. . . . .	113
5.13	Slat chamber cross section (near the border). . . . .	114
5.14	Step model cell. . . . .	115
5.15	No step model cell. The spacer is, in this model, a simple parallelpiped. . . . .	116
5.16	Potential profile (step model), as obtained with Garfield. The numbers in the field lines refer to the potential value. . . . .	117
5.17	Potential profile (no step model). The numbers in the field lines refer to the potential value. . . . .	118
5.18	Ion path from a particle crossing the chamber (step model). . . .	119
5.19	Ion path from a particle crossing the chamber (no step model). . .	120
6.1	Enlarged view of a PCB quarter. The connecting lines are clearly shown. The upper region is dedicated to the readout electronics. .	125
6.2	PCB non bending plane design. The two strip sizes are displayed, together with the corresponding connecting lines. . . . .	126
6.3	Mechanical design of spacers. An enlarged view of the printed circuit on which wires are soldered is displayed. It has been glued on the bending plane. . . . .	129
6.4	X plane after gluing procedure. . . . .	131
6.5	Bending plane view. Cathode plane, spacer, sandwich panel and translator logic are visible. . . . .	131
6.6	20 $\mu\text{m}$ W+Re gold plated wires put under tension. Under the wires the printed circuit (comb-shaped) for wires soldering is visible.	132
6.7	Experimental set-up. . . . .	134
6.8	Schematic representation of a GASSIPLEX-based operation system.	135
7.1	Pedestal value (in ADC ch.) as a function of channel number, for bending and non bending plane. The channels greater than 192 are not connected. . . . .	138
7.2	Sigma pedestal behaviour as a function of channel number, for both planes. The channels greater than 192 are not connected. . .	139
7.3	Correlation between connecting line length and pedestal sigma (non bending plane) for channels connected to different GAS64. .	140
7.4	Correlation between line length and pedestal sigma (bending plane) for channels connected to different GAS64. . . . .	141
7.5	Number of clusters for two HV values. . . . .	143

7.6	Number of hit strips, in the first cluster, as a function of High Voltage. . . . .	144
7.7	Hit strip distribution for cluster from first to fourth, for two voltage values (1600 V at left, 1700 V at right). . . . .	145
7.8	First cluster charge distribution ( $HV = 1600$ V). . . . .	145
7.9	Charge distributions for different clusters and different voltages. .	146
7.10	Most probable value of first cluster charge (in ADC channels) as a function of High Voltage. . . . .	147
7.11	Induced charge on the central strip (top) and in the neighbouring two (center and bottom). . . . .	148
7.12	Fraction of charge induced in each of the three strips, with respect to the first cluster total charge, as a function of High Voltage (central strip: top). . . . .	149
7.13	Number of cluster in the non bending plane ( $HV=1600$ V). . . . .	150
7.14	Non bending plane. Number of hit strips in the first cluster. . . .	151
7.15	Correlation between charge induced in bending and non bending plane. . . . .	152
7.16	Silicon planes displacement from zero position (left: x coordinate, right: y coordinate). . . . .	153
7.17	Residual distribution, in x direction, for the first silicon detector plane. . . . .	154
7.18	Beam projection on to the chamber. . . . .	155
7.19	x (left) and y (right) beam coordinates extrapolated from silicon detectors (top). The same distributions, obtained from the CSC, are plotted on bottom. . . . .	156
7.20	Correlation between track coordinates extrapolated by silicon detectors and those reconstructed by the CSC. On left: x coordinate (non bending plane), on right: y coordinate (bending plane). . . .	157
7.21	Events with at least one cluster, as a function of the particle impact point on the chamber. . . . .	157
7.22	y coordinate distribution without any requirements on the number of hit strips (left). The same distribution, obtained by requiring a cluster made by more than two fired strips, is showed in the plot at right. . . . .	158
7.23	Ratio of events with a cluster made by more than two hits to the events without requirements on hit strips, as a function of y track coordinate. . . . .	159
7.24	Bidimensional view of the coordinate distribution without any cut on fired strip number (left). The same plot, but with the requirement of a cluster made by more than two hit strips, is represented on right. . . . .	159

7.25	<i>x</i> coordinate distribution, extrapolated from silicon detectors (on left). One hit strip in the cluster has been required. On right: ratio of tracks with more than one strip in the first cluster to all events reconstructed by silicon telescope. . . . .	160
7.26	Efficiency curve as a function of high voltage, for two different event selection. . . . .	161
7.27	Reconstruction efficiency as a function of High Voltage. The events have been selected requiring a cluster with, at least, three hit strips and no saturated measured charges (bending plane). . . . .	162
7.28	Residual distribution as a function of the coordinate measured by means of the chamber (bending plane). . . . .	164
7.29	Corrected residual distribution (bending plane) fitted to a gaussian fit (on left). The resolution obtained from the gaussian fit to the not corrected residual distribution is shown on right. . . . .	165
7.30	Bending plane resolution as a function of High Voltage. . . . .	165
7.31	Residual distribution for a cluster made by 3 (solid line) or 4 (dashed line) hit strips. . . . .	166
7.32	Bending plane resolution after the cut on the $\chi^2$ fit of the track. .	167
7.33	Residual behaviour as a function of the <i>x</i> coordinate, measured by means of the chamber. . . . .	168
7.34	Residual distribution (not corrected) for the non bending plane (left). On right the same distribution is shown after the correction.	169
7.35	On left the number of hit strips for the second cluster is shown. The charge distribution for the same cluster is presented on right.	170
7.36	Correlation between the number of hit strips in the first and in the second cluster. . . . .	171
7.37	Position of the second cluster with respect to the first (left). . . .	172
7.38	Pins connector scheme. Each number corresponds to a different line and so to a different strip. . . . .	172
7.39	Position of the second cluster relative to first, when both are made by more than two hit strips. . . . .	173
8.1	LVTTL and LVDS buses. . . . .	177
8.2	Cross section of a PCB plane. Each geometrical parameters involved in LVTTL impedance calculation is indicated. . . . .	177
8.3	Bending plane strip array. The two strip dimensions are indicated.	178
8.4	Non bending plane strip array. The two strip dimensions are indicated. . . . .	179
8.5	Efficiency to identify the hit wire as a function of strip width. . .	180
8.6	Comparison between the characteristics of the large (2000 year) and the small (2001 year) prototypes. . . . .	182

8.7	Schematic view of the experimental setup used in Cagliari laboratories. . . . .	183
8.8	Experimental setup at INFN Cagliari. . . . .	183
8.9	Sigma pedestal (in ADC channels) for the 10 bit ADC noise only. . . . .	185
8.10	Sigma pedestal (in ADC channels) of the 10 bit ADC + GASSI- PLEX chips system. . . . .	185
8.11	Pedestal value (in ADC channels) for the bending plane (top) and non bending plane (bottom). . . . .	187
8.12	Sigma of the pedestal (in 10 bit ADC channels) for the bending (top) and non bending plane (bottom). 1 channel corresponds to 625 electrons. . . . .	188
8.13	Sigma of the pedestal as a function of strip area for bending (top) and non bending plane (bottom). 1 ADC channel corresponds to 625 electrons. . . . .	189
8.14	$^{90}\text{Sr}$ source position in the bending plane large strip region. . . . .	190
8.15	Source position (in ADC channel) in bending and non bending plane, from online display. . . . .	191
8.16	Total charge distribution fitted by a Landau function for different HV values (left: bending plane, right: non bending plane). . . . .	192
8.17	Total charge distribution fitted by a Landau function for different HV values (left: bending plane, right: non bending plane). . . . .	193
8.18	Most probable value of total charge (ADC channels) as a function of High Voltage for bending (circle symbol) and non bending (star symbol) plane. On top: small strips, on bottom: large strips. . . . .	195
8.19	Number of hits in the bending (left) and in the non bending plane (right), for small strips. . . . .	196
8.20	Number of hits in the bending (left) and in the non bending plane (right), for large strips. . . . .	197
8.21	Mean hit value as a function of High Voltage for bending (square) and non bending (star) plane. On top: small strips, on bottom: large strips. . . . .	198
8.22	Strips fired outside the source region in different HV runs for bend- ing (square) and non bending (star) plane. On top: small strips, on bottom: large strips. . . . .	199
8.23	Detector efficiency as a function of HV (no check on outside strips). On top: small strips, on bottom: large strips. . . . .	200
8.24	Reconstruction efficiency as a function of HV for small (top) and large (bottom) strips, by requiring 2 hits outside the source region at maximum. . . . .	202
8.25	Most probable value of total charge on small strips for different HV values and quencher percentage. . . . .	203

8.26	Mean number of hit strips for small strips for different HV values and quencher percentage (top: bending plane, bottom: non bending plane). . . . .	204
8.27	Efficiency as a function of HV and quencher percentage without (top) and with (bottom) check on source region. . . . .	205
8.28	Schematic view of the experimental set-up at CERN PS. . . . .	206
8.29	Pedestal sigma for Saclay (left) and Cagliari (right) prototypes. In this test we used a 12 bits CRAMS with 1.5 V range. . . . .	207
8.30	Resolution in the bending plane as a function of High Voltage (small strip region). . . . .	207
8.31	Non bending plane resolution as a function of High Voltage (small strips). . . . .	208
9.1	Test of the prototype at CERN PS. . . . .	211
9.2	Sigma pedestal for a MANU of bending (left) and non bending (right) planes. . . . .	212
9.3	Resolution in the bending plane as a function of High Voltage. . .	213
9.4	Beam position on the chamber for 4 runs. . . . .	214
9.5	Gain as a function of the 4 positions in the PCB for bending plane.	215
9.6	Bending plane resolution as a function of the four positions on the PCB. . . . .	216
9.7	Bending plane resolution as a function of chamber slope. . . . .	216



# List of Tables

3.1	<i>Number of hits and maximum density per unitary area for each Station, obtained by GEANT and FLUKA simulations. A safety factor of 2 is included [MUOAD]. . . . .</i>	51
3.2	<i>Trigger rates as a function of different beam types (minimum bias), at maximal luminosities. . . . .</i>	51
3.3	<i>Main tracking chambers features [Tou01]. . . . .</i>	55
4.1	<i>Strip segmentation and number of channels in the bending plane (y direction). . . . .</i>	81
4.2	<i>Strip segmentation and number of channels in the non bending plane (x direction). . . . .</i>	81
4.3	<i>MANAS-16 and GASSIPLEX 0.7 <math>\mu\text{m}</math> main features. . . . .</i>	92
4.4	<i>Comparison of GASSIPLEX 0.7 <math>\mu\text{m}</math> and 1.5 <math>\mu\text{m}</math> characteristics. . . . .</i>	94
5.1	<i>Luma quotation for gold plated and cleaned and straightened wires (May 2001). For all quotations VAT is included. . . . .</i>	104
6.1	<i>Thickness, and corresponding radiation length, of each material used in each chamber plane. The contribution from electronics has not been taken into account. . . . .</i>	133



# Acknowledgements

Innanzitutto vorrei ringraziare il Prof. Sergio Serçi, per avermi permesso di proseguire e ampliare l'attività scientifica intrapresa durante il lavoro di tesi di laurea nell'ambito delle attività sperimentali del Gruppo 3 della Sezione INFN di Cagliari e per aver reso possibile questo lavoro di tesi, che mi ha portato ad effettuare esperienze utili ed interessanti e a collaborare con persone di alto livello professionale.

Un GRAZIE di cuore al mio relatore, nonché caro Amico, Corrado Cicalò, con cui ho avuto il piacere e la fortuna di lavorare a stretto contatto durante questi anni.

Grazie per avermi resa sempre partecipe delle tue innumerevoli conoscenze e competenze, per avermi seguita con attenzione costante e aver sopportato con tanta, tantissima pazienza, il mio caratteraccio, per avermi trasmesso il tuo entusiasmo per questo lavoro, per avermi aiutata a crescere e maturare professionalmente, per avermi consigliata sempre per il meglio e per averlo fatto in modo assolutamente disinteressato, per i nostri incontri/scontri, talvolta duri, ma sempre costruttivi...

Grazie per essere stato, in alcuni momenti, soprattutto in quelli di sconforto, l'unica persona su cui ho sentito di poter veramente contare e perchè senza di te questo lavoro (e non solo questo...) non sarebbe mai stato possibile.

Un sentito grazie alla prof.ssa Giovanna Puddu per l'aiuto scientifico e il supporto morale che mi ha fornito in continuazione, per le belle esperienze professionali condivise assieme, per l'attenzione costante, scientifica e umana, con cui ha continuato a seguirmi e per la sua professionalità.

Ad Alessandro va un grande ringraziamento per i suoi innumerevoli insegnamenti e consigli, per la pazienza, la disponibilità, la stima (spesso immeritate) e l'amicizia che ha continuato a dimostrare nei miei confronti.

Un ringraziamento particolare va alla Prof.ssa Maria Paola Macciotta, non solo per i tanti suggerimenti professionali che mi ha fornito e per la sua esperienza che ha messo a mia disposizione e di cui ho cercato di far tesoro, ma anche per la pazienza che ha dimostrato nel cercare di insegnarmi a svolgere con il giusto equilibrio (e una buona dose di distacco e diplomazia) un lavoro bello, speciale e impegnativo come questo...

A Davide, Marcellino e Mauro un grazie enorme per avermi trasmesso le loro tante conoscenze in modo chiaro e piacevole, per la loro competenza e l'aiuto che mi hanno dato in numerose occasioni, per il loro buonumore e per la loro capacità di saper rendere i momenti più duri e faticosi in allegri e divertenti e riuscire a creare in questo modo un ambiente di lavoro estremamente piacevole.

Grazie, ancora una volta, a tutto il gruppo PINOT di Torino e in particolare ad Alessandro, Alfredo, Beppe, Chiara, Enrico, Mauro, Paolo, Pietro e Roberta, per i momenti piacevoli trascorsi durante i run ZDC e per la stima e l'affetto che mi hanno dimostrato in più di un'occasione.

Merci beaucoup Alberto, Didier, Fabienne, Jean-Claude, Herve, Pierre, Sophie, Lionel et Manoel pour votre sympathie et votre disponibilité et pour les moments très intéressants et stimulants partagés au CERN.

Je voudrais remercier vivement Yves Le Bornec pour avoir accepté d'être mon rapporteur de thèse, pour ses observations, les remarques et les précieux conseils.

I would like to express my gratitude to Rob Veenhof for his great patience and help while trying to teach me something about simulation programs and tracking chamber physics and for his great availability.

Ai neo-laureati, Stefano e Stefania, un ringraziamento per i momenti, belli e faticosi, ma anche divertenti e sempre stimolanti, trascorsi al CERN e a Cagliari. Ad entrambi un augurio sincero affinché conservino ancora a lungo almeno un pizzico del loro entusiasmo.

Sia il periodo della laurea che quella del dottorato mi hanno permesso di stringere o rafforzare amicizie con persone speciali, che in questi anni sono state sempre presenti e non hanno mai mancato di dimostrarmi il loro affetto. A Cristiana, Fabrizio, Giampaolo, Lara, Luca, Luisa e Silvia va un affettuoso e sincero grazie!!

Fra questi vorrei ringraziare in modo particolare Carlo Nicola, mio compagno di ufficio prima e carissimo amico poi, per le belle chiacchierate e gli ottimi consigli

ricevuti, per essere stato una figura di riferimento importante e sempre presente, per i momenti che abbiamo condiviso durante il nostro percorso da dottorandi, per la sua amicizia che la forzata lontananza non è finora riuscita a scalfire.

Grazie anche a Daniele, Davide P., Gianluca, Luisanna, M. Assunta, Rachele e Walter, per aver contribuito, ciascuno in modo diverso, a rendere piacevoli questi anni di lavoro.

Grazie a Stefania per essere, ormai da quasi 29 anni, la migliore amica che si possa desiderare, sempre vicina, nei momenti belli e brutti, sempre disponibile e paziente ad ascoltarmi, sostenermi e aiutarmi...

Grazie a tutti coloro che, a diverso titolo, mi sono stati vicini in questi anni, in particolare Mamma, Papà, Enrico e Francesco per aver sempre rispettato le mie scelte, sostenendomi e incoraggiandomi in qualunque momento.

Infine un grazie speciale a due persone speciali...grazie ai miei studenti Stefano e Maurizio per aver ridimensionato l'importanza del mio lavoro di ricerca facendomi capire, in questi pochi mesi di insegnamento, che trasmettere le proprie conoscenze in maniera semplice ma non banale e comprensibile da tutti è talvolta più difficile, e anche più gratificante e appagante dal punto di vista umano, che cercare l'evidenza sperimentale del QGP....

Cagliari, 1998-2001



# Introduction

According to QuantoCromo Dynamics a phase transition from a state in which quarks and gluons are confined within hadrons to a deconfined one should occur at high temperature and energy density conditions.

Lattice QCD calculations give values between 140 and 180 MeV, corresponding to an energy density of nearly 1 GeV/fm<sup>3</sup>, or seven times that of nuclear matter for the transition temperature to this state, called Quark Gluon Plasma (QGP). Temperatures and energy densities above these values existed in the early Universe during the first few microseconds after the Big Bang. The study of this state evolution involves particle and nuclear physics and also astrophysics, since the cores of some dense neutron stars might be in a deconfined phase.

Experimentally it is possible to achieve high temperatures and energy densities by means of heavy ion collisions at ultrarelativistic energies. To see if the deconfinement occurred the behaviour of some physical variables, sensitive to the presence of a deconfined phase, must be studied. The physics programme started at CERN in 1986 with the acceleration of light ions (<sup>16</sup>O and <sup>32</sup>S) achieving a center of mass energy up to 200 GeV/nucleon. A 158 GeV per nucleon Lead ion beam has been produced in 1994. Seven complementing experiments participate to the Lead beam program, measuring different aspects of lead-lead and lead-gold collision events: NA44, NA45/CERES, NA49, NA50, NA52/NEWMASS, WA97/NA57, and WA98. The large amounts of collected data led CERN to announce that the formation of “*a new state of matter where quarks and gluons are not confined*” is evident. One of the most important QGP signature is the suppression of charmonia production. In fact, it is foreseen that in a deconfined medium the colour binding potential between  $c$ - $\bar{c}$  quarks would be screened, avoiding the formation of charmonia states. Such signature has been extensively studied by NA38 and NA50 collaborations.

At LHC accelerator one of the four foreseen experiments, ALICE (A Large Ion Collider Experiment), will be entirely dedicated to the study of QGP detection in heavy ion collisions. This experiment is mainly devoted to the study of a large number of QGP signatures. It will be possible, by accelerating Lead ions, to achieve better conditions for what concerns energy density, spatial dimensions

and mean lifetime of the produced system and to study the suppression not only of  $c\bar{c}$  but also of  $b\bar{b}$  states. The heavy vector mesons will be identified through their muonic pair decay in a forward muon spectrometer (Muon Arm). Muon trajectories and momenta will be reconstructed by means of 10 tracking planes organized into five stations. These detectors are cathode strip chambers for which a high spatial resolution and efficiency are required. Beside this, the last three stations involve mechanical and technical problems for which a modular approach has been chosen. Their construction is in charge to CEA Saclay, INFN Cagliari, PNPI Gatchina and SUBATECH Nantes.

In this thesis the study of the last three stations performances is presented. Simulations have been done to help the design of final tracking detectors. They led to the construction of some prototypes which have been also tested at CERN PS.

In the first chapter an overview of heavy ions physics will be given. The most important results obtained at CERN SPS will be presented.

The ALICE experiment will be described in the second chapter, where a detailed description of Muon Arm system will be also made.

In the third chapter the required performances, which lead to the final detector choice, will be outlined. Its operation mode will be described and validated by means of simulation studies.

The tracking system will be discussed in more details in the fourth chapter, where the electronics readout will be also presented.

The fifth will be entirely dedicated to simulation studies while in the sixth the assembly of a large size prototype will be described. Such prototype has been in-beam tested at CERN PS and the results obtained from the analysis of the data will be shown in chapter 7. A small prototype has been later built to better understand some detector performances and to test a new electronics version. A preliminary detector study, with a  $^{90}\text{Sr}$  source, has been made in Cagliari laboratories before the test at PS. The most significative results of these two tests will be described in chapter 8. In the last chapter the main results of a test made on a prototype equipped with the almost final electronics will be presented and the conclusions will be drawn.



# Chapter 1

## Quark Gluon Plasma

The Quantum ChromoDynamics (QCD) describes the interaction of the colour charges of quarks and gluons. Two of the most important predictions of this theory are the confinement of quarks inside the hadronic matter and the existence of a phase transition from a system made by colourless hadrons to a deconfined phase in which hadronic matter is dissolved in its constituents. Such inverse transition should have been happened at about  $10^{12}$  kelvin and  $\simeq 10^{-5}$  seconds after the Big Bang and it is called Quark Gluon Plasma (QGP).

In the last ten years such predictions have been tested by means of heavy ion collisions at ultrarelativistic energies. In such collisions a large amount of energy is deposited during a short time and in a small spatial region. This should allow to create a medium with density from 10 to 100 times higher than the ordinary nuclear matter.

An ultrarelativistic heavy ions physics programme first started at BNL AGS accelerator, achieving a 5 GeV center of mass energy, and then at CERN SPS, where a 20 GeV value has been reached.

Since 1986 light ions were accelerated ( $^{16}\text{O}$  at 60 GeV/nucleon and  $^{32}\text{S}$  at 200 GeV/nucleon, at CERN) and in the nineties heavy ions were used in experiments at AGS and at SPS.

At CERN SPS, since 1994, more favourable conditions have been in fact met by accelerating Lead ions, at 158 GeV per nucleon. It is estimated that in these collisions an energy density of about  $3 \text{ GeV/fm}^3$  has been obtained, 20 times higher than the nuclear density. This corresponds to a temperature of  $\sim 200 \text{ MeV}$  ( $\sim 2.3 \cdot 10^{12}$  kelvin) which is about 5 order of magnitude larger than the temperature in the center of the Sun. The results obtained at SPS experiments led Professor Luciano Maiani, CERN Director General, to announce, in February 2000, that “*We now have evidence of a new state of matter where quarks and gluons are not confined*” [CERN].

For what concerns the present, RHIC collider at BNL started its heavy ion

programme in summer 2000, reaching a  $\sqrt{s_{NN}}$  of 200 GeV per nucleon in Au-Au collisions.

In the future (2007) CERN LHC will achieve even better conditions for what concerns energy density, spatial dimensions and lifetime of the produced system.

The study of a phase transition is performed by non perturbative QCD, using analytical and numerical solutions which are difficult to be solved. In the following a phenomenological model, useful to explain in a qualitative way some aspects of strong interactions, will be presented. A more rigorous approach, based on lattice theory, will be later discussed.

## 1.1 MIT Bag Model

Theoretical results show that when the separation between a quark and an antiquark becomes large, it is more favourable, from an energetic point of view, to create another quark and antiquark pair. It would be impossible to separate a quark from its antiquark partner, resulting in their confinement inside the hadrons. Experimentally no single quark has been detected: quarks seem to be permanently confined within hadrons [Won94].

An useful phenomenological description of quark confinement inside hadrons is provided by MIT Bag Model [Cho74]. It is an intuitive description which helps to understand why a stable system can undergo over a phase transition.

This model describes massless quarks when they are inside a finite dimension bag and with an infinite mass when they are outside. Moreover, also gluons are confined inside the bag and therefore the total colour charge inside the bag must be zero.

In this model confinement is the result of the equilibrium between a bag pressure  $B$ , directed inward, and the stress originated by quark kinetic energy, leading to a stable system. Pressure is a phenomenological quantity useful to take into account non perturbative effects of QCD.

To estimate the pressure we can suppose to have  $N$  massless fermions in a spherical volume with radius  $R$  and in thermal equilibrium at temperature  $T$ . The pressure (with  $\hbar = c = 1$ ) is [Has81]:

$$B^{1/4} = \left( \frac{2.04N}{4\pi} \right)^{1/4} \frac{1}{R} \quad (1.1)$$

If, for example, we take into account a confinement radius of 0.8 fm for three quarks in a baryon, we obtain an estimation of  $B^{1/4} = 206$  MeV.

If the pressure inside the bag grows up there will be a value for which the pressure directed outward will be greater than the inward one. When this happens

the bag can no longer confine particles inside it. A new phase of matter, with quarks and gluons in a deconfined state, is therefore possible.

This pressure can be originated either by a high matter temperature or by a high density in the baryonic number. Both conditions could be simultaneously verified.

Figure 1.1: *Phase transition originated by a high temperature and/or a high baryonic number density.*

### 1.1.1 QGP at high temperatures

Let's take into account a gas made by a quark-gluon system in thermal equilibrium at high temperature  $T$  and inside a volume  $V$ . We suppose that such particles do not interact, that they are massless and the net baryon density (given by baryon density minus antibaryon density) is zero. The total pressure of this system, at temperature  $T$ , is [Won94]:

$$P = 37 \frac{\pi^2}{90} T^4 \quad (1.2)$$

and energy density is [Won94]:

$$\varepsilon = 37 \frac{\pi^2}{30} T^4 \quad (1.3)$$

If  $T$  is 200 MeV the energy density is 2.54 GeV/fm<sup>3</sup>. By combining eq. 1.1 and 1.2 the critical temperature at which the pressure of the quark-gluon system is equal to the bag pressure is:

$$T_c = \left( \frac{90}{37\pi^2} \right)^{1/4} B^{1/4} = \left( \frac{90}{37\pi^2} \right)^{1/4} \left( \frac{2.04N}{4\pi} \right)^{1/4} \frac{1}{R}; \quad (1.4)$$

If  $B^{1/4} = 206$  MeV, as shown before,  $T_c \sim 144$  MeV.

If the matter inside the bag achieves a temperature higher than  $T_c$ , the gas pressure will be greater than the bag pressure  $B$ . The bag will be no longer able to contain the matter and the deconfinement will occur. Such deconfined phase is called *Quark Gluon Plasma*.

### 1.1.2 QGP at high baryonic density

It is possible to obtain a deconfined system also when the temperature is close to zero. We suppose that the matter inside the bag is made by only quarks. The baryonic density is therefore very high. According to Pauli exclusion principle no more than one fermion can be in a state characterized by definite quantum numbers. When the density increases quarks must complete higher and higher momentum states. The quark gas pressure grows up owing to the gas degeneracy (which increases with density), until it will be higher than the bag pressure. The bag will be broken and a new state, in which quarks are deconfined, will be formed. Since the baryonic number of each quark is  $1/3$  a high quark density implies a high baryonic density. The baryonic density at which such transition occurs is given by [Won94]:

$$n_B(QGP) = \frac{4}{3} \left( \frac{g_q}{24\pi^2} \right)^{1/4} B^{3/4}, \quad (1.5)$$

where  $g_q$  is the degeneracy number of matter made by quarks.

If we take into account a plasma originated by the compression of ordinary nuclear matter, which contains only valence quarks  $u$  and  $d$ , the degeneracy number is:

$$g_q = (3 \text{ colours}) \times (2 \text{ spins}) \times (2 \text{ flavors}) \quad (1.6)$$

For a bag pressure of  $B = 206 \text{ MeV}$ , the critical baryon number density at which ordinary hadronic matter undergoes a phase transition at  $T = 0$  is  $n_B(QGP) \sim 0.72 \text{ nucleons/fm}^3$ . This value is about 5 times larger than the baryonic density ( $n_B \sim 0.14 \text{ nucleons/fm}^3$ ) for normal matter at equilibrium.

Between these two cases it is possible to have an intermediate situation. The total pressure can be in fact originated both by the kinetic energy of particles and by the degeneracy of fermion gas. If neither the temperature or the baryonic density is zero, the critical temperature at which the deconfined phase appears is between  $T = 0$  (for a degenerate quark gas) and  $T_c$  (for a pure plasma with baryonic density zero). This leads to the phase diagram illustrated in fig. 1.2. Along the x axis the baryonic chemical potential (a measure of the nucleon density) and the baryonic density, relative to the ordinary one, are represented, while in y the temperature is plotted.

The shadowed line, which defines the boundaries between confined and deconfined phases, is less important at low baryonic potential where lattice QCD is more reliable and it gets more important at high baryonic densities where it is more difficult to perform non perturbative calculations.

In this figure it is also displayed the trajectory we think the Early Universe went through at the time of the Big Bang. It is very close to the y axis because

Figure 1.2: *Phase diagram of nuclear matter.*

the baryon density was very low. In fact at the Big Bang time the excess of baryons over antibaryons, of matter over antimatter, was very low.

It has been supposed that the Universe went through this phase transition at about  $10 \mu\text{s}$  after the Big Bang. In this region the critical temperature should be of the order of 170 MeV.

Here are also plotted some ideal trajectories that matter could go in heavy ion collisions at SPS, AGS, RHIC and LHC accelerator. There is another interesting region at low temperature and high baryonic potential regarding neutron stars. In fact the cores of some dense neutron stars might be in a deconfined phase [Web01].

## 1.2 Lattice QCD

The bag model provides only a qualitative estimation on the possible formation of Quark Gluon Plasma. It is better to treat such argument from a more rigorous point of view, by using more advanced theoretical models.

The equilibrium and transition phases involve quarks and gluons interacting at large distances. A non perturbative study is therefore required, since a perturbative treatment, based on expansion in powers of the coupling constant, is no longer applicable.

Numerical studies [Kac99] demonstrated that non perturbative phenomena prevail up to temperatures few times greater than the critical value  $T_c$ .

Lattice QCD is a non perturbative treatment of Quantum ChromoDynamics, in which the Lagrangian is discretized on a lattice of space-time coordinates. The distance between nearest lattice points defines the maximum momentum scale cut-off for the calculation. By taking the limit to zero of the lattice size, the terms which diverge for very large momenta will become finite, eliminating in a natural way the ultraviolet divergencies( [Cel84], [Eng90]).

Since lattice calculations are limited by computer memory and speed, the number of lattice points and their spacing cannot be too small.

A phase transition is of order  $n^{th}$  if the  $n^{th}$  derivative of the free energy  $\partial^n F / \partial T^n$  is discontinuous with respect to the temperature  $T$  while the lower order derivatives are continuous. A first order phase transition will be therefore characterized by a  $\partial F / \partial T$  discontinuous derivative and a continuous free energy. The energy density, defined as the ratio of the total system energy to the volume  $V$  of the system itself, is correlated to  $\partial F / \partial T$  through the following relation:

$$\varepsilon = \frac{E}{V} = \frac{F + T \frac{\partial F}{\partial T}}{V} \quad (1.7)$$

In a first order phase transition also the density energy will be discontinuous. The energy density difference at the discontinuity gives us the latent heat.

In a second order phase transition the free energy  $F$  and  $\partial F/\partial T$  are continuous while  $\partial^2 F/\partial T^2$  is discontinuous with respect to  $T$ . Since the specific heat at constant volume is correlated to  $\partial E/\partial T$  or  $\partial^2 F/\partial T^2$ , a second phase transition will be characterized by a continuous free energy and energy density and by a discontinuous specific heat, at constant volume. Lattice QCD calculations help to determine the order transition of a phase.

Since the beginning of the eighties many Monte Carlo calculations have been made for a system at finite temperature and in the limit of infinite mass quark. In particular it is interesting to evaluate the phase order transition (if it exists) and the critical temperature at which such transition occurs. In Monte Carlo calculations, a first order transition should show itself as a flip between the “ordered” and the “disordered” phase. These metastable states are not easy to recognize, in particular if the lattice size is small. In this case flips between different thermodynamical states cannot be distinguished from statistical fluctuations.

In fig. 1.3 the energy density of a strongly interacting system versus the temperature of the system itself in terms of deconfinement temperature is shown.

Figure 1.3: *Energy density in units of  $T^4$  for QCD with 3 dynamical light quark flavors, extrapolated to zero quark mass and to the continuum.*

These calculations are performed with 3 flavors (up, down and strange) neglecting the effect of their masses. The system starts out with rather low  $\epsilon$  values and at a certain point ( $T = T_c$ ) the energy density increases very rapidly. This

is due to the larger number of degrees of freedom in the deconfined phase with respect to the confined one. If we take for the critical temperature a 170 MeV value the required energy density is about 1 GeV/fm<sup>3</sup> [Kar]. This behaviour seems to indicate a first order phase transition, characterized by a discontinuity in the energy first derivative. The transition occurs from a hadronic gas to a plasma of quarks and gluons, with the density system approaching the plasma value in an asymptotic way.

A more realistic calculation, which includes quark masses, is required [Lee95]. In fig. 1.4 results, obtained by Columbia Group [Bro90] using a lattice  $16^3 \times 4$ <sup>1</sup>, show that the order transition appears to depend on quark masses. The x axis indicates the masses of up and down quarks multiplied by the lattice size  $l$ , while the y axis represents the strange quark mass in the same units.

Figure 1.4: *Phase transition for a  $16^3 \times 4$  lattice.*

The E point refers to the case  $m_{u,d} = m_s = \infty$  and shows a first order transition. The extrapolation to  $m_{u,d} \simeq 0$  should lead to a second order phase transition. On the other side when  $m_{u,d} = m_s = 0.025/l$  (point A) the transition seems to be of the first order, while when  $m_s$  increases up to  $0.1/l$  (point B) the transition is again of the second order. The empty circle, which represents the point of physical interest, lies in the second order region but the number of lattice sites in the imaginary time direction  $\tau$  is too low.

Doubling  $N_\tau$  intervals (from 4 up to 8) new results, which suggested a second

---

<sup>1</sup>The lattice volume is given by the product of lattice points along the three spatial axis and the number of lattice sites in the imaginary time direction  $\tau$ .



order transition phase, were found [Maw93].

Later, by considering  $N_\tau = 8$  and increasing the spatial dimension to  $32^3$ , taking into account only up and down quarks ( $m_s \rightarrow \infty$ ), it was established that a second order phase transition is correct for the two flavor quarks [Zhu94]. Some recent studies [Kac99] are instead consistent with a first order transition.

## 1.3 How to study QGP

In order to study QGP formation it is necessary to reproduce the following conditions ([Kar], [Hei]):

- The system dimensions must be bigger than the typical strong interaction range ( $\sim 1$  fm). It should also be made by a great number of interacting particles to allow the use of macroscopic variables like temperature, density, etc.
- The system must reach the equilibrium, and so the thermalization, phase to be described with thermodynamical variables. This can be achieved and kept during the expansion only if the system is characterized by a sufficient number of interactions. The number of collisions per particle has therefore to be higher than one.
- The energy density and the temperature must reach the values foreseen by lattice QCD calculations.

Such conditions can be experimentally reached with heavy ion collisions at ultrarelativistic energies. The obtained energy is in fact nearly proportional to the number of interacting particles. Due to the Lorentz contraction two colliding nuclei appear as thin disks (fig. 1.5). The collisions between nucleons, in a nucleus-nucleus interaction, occur therefore nearly at the same time and in the same spatial position. In such collisions nucleons lose most of their energy and a high energy density region is created ([Won94]).

With heavy ions it should therefore be possible to create the appropriate conditions for new forms of matter under extreme conditions of energy densities and high temperatures. A high energy deposition is foreseen to give rise to a fireball of quarks and gluons in a deconfined state.

After its creation the system goes through a mixed phase, in which a gas of quarks, gluons and hadrons can exist. It then expands and cools down until all partons recombine into hadrons and the fireball freezes out.

It is not possible to observe directly the phase transition products. In fact, the plasma state is characterized both by a preceding pre-equilibrium partonic phase and by a subsequent hadronic rescattering phase.

Figure 1.5: *Simplified picture of Pb-Pb collisions.*

Figure 1.6: *Time evolution of fireball.*

Its formation should be put in evidence by some signatures, i.e. physical effects which are consequences of the phase transition and cannot be explained otherwise [Ant01].

Seven large experiments participate to the Lead beam programme at CERN, measuring many different aspects of Lead-Lead and Lead-Gold collision events: NA44, NA45/CERES, NA49, NA50, NA52/NEWMASS, NA97/WA57 and WA98. Some of these experiments use multipurpose detectors to measure simultaneously and correlate several of the most abundant observables. Others are dedicated to study rare signatures with high statistics. This coordinated effort, using several complementing experiments, has proven to be very successful. In the following some of the most important results within this program will be summarized [Hei00].

### 1.3.1 Collision centrality

In a nucleus-nucleus collision the center of each nucleus passes the other at a distance  $b$ , the so called impact parameter. The nucleons which are outside the overlapping region continue essentially unaffected and are called *spectators*. The nucleons which are in the overlapping region interact and give rise to the fireball we want to study and are called *participants*. With centrality essentially we mean how far the centers of the two colliding nuclei passed each other.

Figure 1.7: *Schematic view of a central (left) and peripheral (right) nucleus-nucleus collision.*

Experimentally the centrality can be estimated by measuring one of these variables:

- $N_{ch}$ , the number of charged particles produced in a given rapidity<sup>2</sup> interval. This quantity nearly increases in a linear way with the number of participants.
- $E_T$ , the transverse energy<sup>3</sup> which also increases with the number of participants.
- The energy released by spectators. This “forward” energy can be measured by a Zero Degree Calorimeter ( $E_{ZDC}$ ).

Assuming that  $N_{ch}$  and  $E_T$  are directly proportional to the number of participant nucleons, i.e. that  $E_{ZDC}$  varies as a function of the number of spectator nucleons, it is possible to describe the measured distributions in the framework of the Glauber model of nucleus-nucleus collision. It is therefore possible to calculate the relationship between the measured quantities and  $N_{part}$ , and thus to compare the results from several experiments as a function of a common centrality variable [Chia01].

At SPS energies, in central Pb-Pb collisions, about 2500 particles are produced (NA49). More than 99.9 % of them are hadrons [Hein].

### 1.3.2 Initial energy density

The energy density reached in the collisions can be estimated by means of Bjorken's formula [Bjo83]:

$$\varepsilon_{BJ}(\tau_o) = \frac{1}{Ac\tau_o} \frac{dE_T}{dy} \Big|_{y=0}, \quad (1.9)$$

where  $A$  represents the transverse overlapping area while  $\tau_o \simeq 1 \text{ fm}/c$  (also known as proper time) is the time it takes to the energy initially stored in the field to materialize into hadrons [Ant01].  $dE_T/dy$  is the transverse energy per unit rapidity around  $y_{cm}$ .

For Lead-Lead central collisions at 158 AGeV ( $A \simeq 160 \text{ fm}^2$  and  $dE_T/dy=400$

---

<sup>2</sup>The rapidity  $y$  is defined as:

$$y = \frac{1}{2} \ln \frac{E + p_z}{E - p_z} \quad (1.8)$$

where  $p_z$  is the longitudinal component of the momentum along the beam direction ( $z$  axis) and  $E$  is the beam energy.

<sup>3</sup>The transverse energy is defined as  $E_T = \sum_{i=1}^n E_i \sin \theta_i$ , where  $E_i$  and  $\theta_i$  are, respectively, the energy and the angle formed by the particle direction with respect to the  $z$  axis. In a fixed target experiment such axis corresponds to the beam direction. The sum includes all particles produced during the interaction.

GeV) Bjorken estimate provides an energy density value enough for deconfinement,  $\varepsilon \sim 2.5 \text{ GeV/fm}^3$ . This value is larger than the one foreseen for the occurrence of the phase transition. NA49 at CERN obtained a similar experimental result,  $\varepsilon \sim (3.2 \pm 0.3) \text{ GeV/fm}^3$  [Alb95].

### 1.3.3 System temperature

The most important parameters, which characterize the evolution towards the final state, have been verified with great accuracy. The chemical freeze-out and baryon chemical potential have been estimated by NA49 experiment, using statistical models of the hadronization processes. Though several versions of these models exist the values of the two parameters are always the same:  $T \sim 170 \text{ MeV}$  and  $\mu_B \sim 270 \text{ MeV}$  ([Alb95], [Bra99]). Such a temperature is very similar to the one foreseen for the phase transition. It is therefore probable that the system undergoes the phase boundary shortly before the chemical freeze-out point.

It is possible to have informations about the expansion of the hadronic system by studying the transverse mass distributions of particles produced during the collisions and using the results from HBT analysis. Usually the transverse mass spectra of identified particles are fitted to thermal distributions:

$$\frac{dN}{dm_T} \propto m_T \cdot \exp\left(-\frac{m_T}{T}\right) \quad (1.10)$$

This study has been performed by NA49, NA44 and WA97 experiments. In fig. 1.8 the particle mass is plotted along the x axis, while in y the temperature is drawn, showing a strong dependence of the temperature from the particle mass. The heavier is the particle, the higher is the temperature [Ant00].

The temperature  $T$  is also called “inverse slope”, or “apparent temperature” or “ $m_T$  slope” [Ant01]. This is due to the fact that the temperature of the  $m_T$  spectra is modified by the presence of a collective transverse flow, caused by the explosion of the fireball ([App98], [Bea98]).

The temperature  $T$  is approximately given by the sum of two terms: the freeze-out temperature  $T_F$  (i.e. the temperature the particles have when they stop to interact) and a term proportional to the square of the transverse flow velocity,  $\frac{1}{2}m < v_T >^2$ .

The anomalous behaviour shown by the  $\Omega$  in fig. 1.8 has been explained as an earlier kinetic freeze-out, due to the absence of strong rescattering with pions. This indicates that the enhancement of the  $\Omega$  is due to the pre-hadronic phase.

It is difficult to separate the thermal and flow contributions since the errors are too large to do it. Such information can be provided by Bose-Einstein pion correlations. The method has been at first developed by Hambury-Brown and Twiss to measure the size of a star using the Bose-Einstein correlation between

Figure 1.8: *Correlation between particle mass and  $m_T$  spectra inverse slope  $T$  for Pb-Pb collisions.*

pairs of photons emitted from a star and detected at the same time on Earth [Ham56]. It has been later applied to particle physics to study the correlations of pairs in proton-antiproton collisions [Gol60].

The correlation function  $C(q)$  is defined as the ratio of the probability for the coincidence of two bosons with four-momenta  $k_1$  and  $k_2$  relative to the probability to observe separately the two particles [Won94]:

$$C(q) = \frac{p(k_1, k_2)}{p(k_1) \cdot p(k_2)} = 1 + \lambda e^{-(qR)^2} \quad (1.11)$$

This correlation function depends only on the four momenta difference  $q$ .  $\lambda$  is called chaoticity parameter and can assume any value ranging from zero (when the system is completely correlated) up to 1 (maximum non correlation effect).  $R$  is a 4-vector and gives informations on the dimensions of the source emitting the particles.

The information from the HBT radii provides a relation between the transverse flow velocity  $\beta_T$  and freeze-out temperature  $T_F$ . The two informations can be combined with that coming from the particle spectra to get an estimate of the freeze-out parameters ( [Hei99], [Tom]).

A  $T=(120 \pm 12)$  MeV freeze-out temperature is obtained which corresponds to an average density of  $\varepsilon \sim 0.05$  GeV/fm<sup>3</sup> [App98]. WA98 experiment has obtained slightly lower temperature values with a similar analysis [Pei99].

The average radial flow velocity  $\langle v_T \rangle$  is  $\sim 0.5$  c and the volume of the fireball at the freeze-out moment is nearly 2000 fm<sup>3</sup> ( [Sta99], [App98], [Tom]).

This indicates that the fireball is clearly expanding at about a half the speed of light, as a consequence of a large pressure generated inside the fireball.

To study what happens between the fireball creation and the freeze-out moment it is necessary to observe the signatures of the phase transition.

## 1.4 Thermal dileptons

The study of vector mesons through their decay into electron-positron pairs (dileptons), could give informations about the occurrence of a phase transition. The  $\rho$  meson behaviour is particularly interesting. In fact, due to their short lifetime (1.3 fm/c) compared to the typical fireball lifetime (10-20 fm/c at SPS energies), most of  $\rho$  mesons decay within the interaction region. The dileptons, due to their electromagnetic character and having a large mean free path, can escape from this region without further strong interactions in the final state. The dielectron spectrum measured by the experiment gives informations about the early stages of the collision. A careful analysis of the resulting dielectron invariant mass spectrum should, in principle, allow to unfold the whole spacetime history of the nuclear collision. The experiment NA45/CERES showed that in S-Au and Pb-Au collisions the expected  $\rho$  peak is completely smeared out. An excess of dileptons, 3 times larger than in proton-nucleus collisions, in the mass range between 250 and 700 MeV, shown in fig. 1.9, has also been found [Len99].

A large fraction of the observed enhancement could be explained by annihilation processes, predominantly  $\pi^+\pi^- \rightarrow \rho \rightarrow e^+e^-$ , due to the thermal radiation from the interaction phase of the fireball. The spectral shape in the excess region cannot in any case be explained without introducing modifications of the vector mesons properties in the medium [App01]. Two different theoretical models both well reproduce CERES results. The first explains the  $\rho$  mesons mass in the hot medium as a precursor of chiral symmetry<sup>4</sup> restoration [Li95], the other takes into account modifications of mesons properties due to their interactions with the surrounding hadrons [Rap97].

The limited mass resolution of CERES spectrometer did not allow for a systematic investigation of possible modification in the narrower mass region of  $\omega$  and  $\phi$ . A magnet system and a Time Projection Chamber have been added during 1999.

Some tests at 40 AGeV have been done to study the effect of varying the baryon density and to provide additional constraints for the model calculations [Fil01]. The measured  $e^+e^-$  yield shows an enhancement by a factor of  $5.0 \pm$

---

<sup>4</sup>QGP shows the so called *chiral symmetry* (which is spontaneously broken in normal matter), resulting in effective quark masses which are much larger than the current quark masses [Hei].

Figure 1.9: *Inclusive  $e^+e^-$  mass spectra obtained from the '95 and '96 analysis. The data are compared to the sum of the expected contributions from hadron decays [Len99].*

1.5, in the mass range  $m_{ee} > 200 \text{ MeV}/c^2$ , with respect to the expectations from known hadronic sources in heavy ion collisions (fig. 1.10).

The analysis of the 2000 data will provide a dilepton mass spectrum with a mass resolution  $\Delta m/m < 2\%$  in the region of  $\omega$  and  $\phi$  resonances.

## 1.5 Strangeness enhancement

Strangeness enhancement as a QGP signature has been proposed in 1982 by J. Rafelski and B. Muller [Raf82].

The masses of deconfined quarks are expected to be about 350 MeV lower than those of quarks confined within hadrons, due to the partial restoration of chiral symmetry. The strange quark should be very sensitive to such process. Its constituent mass is about 500 MeV so its bare mass should be about 150 MeV. While in hadronic matter the production probability for strange quarks is low due to its high mass, strangeness production should be enhanced if the system is deconfined since the mass goes down to a value comparable with the critical temperature (100-200 MeV). Strangeness production is also favoured by Pauli blocking of u and d states.



Figure 1.10: *Inclusive  $e^+e^-$  invariant mass spectrum at 40 AGeV compared to the expectations from known hadronic sources in heavy ion collisions (left) and to several model calculations (right) [App01].*

When the plasma cools down it eventually hadronizes, leading therefore to an increase of strange hadrons. Such enhancement should be larger for particles of higher strangeness content. In a deconfinement scenario we expect that hadrons containing  $N$  strange quarks will be produced with a rate  $E_s^N$  times higher than in an environment with no strangeness enhancement, like p-A interactions [Hei99]. This thus requires that  $E_\Omega > E_\Xi > E_\Lambda$ , where  $E_i$  is the enhancement of the particle  $i$  with respect to p-A collisions [Chia01].

A certain amount of enhancement in the abundance of strange particles can be expected even in the absence of QGP, through reactions like:

$$\pi + \pi \rightarrow K + \bar{K} \quad (1.12)$$

$$\pi + N \rightarrow \Lambda + K \quad (1.13)$$

Such processes are relatively “easy”, which means that they are fast on the timescale of the collision, for kaons and  $\Lambda$ , but things become harder and harder, i.e. slow on the collision timescale, for particles of larger strangeness content. Models based on hadron rescattering give therefore an opposite pattern, with respect to QGP scenario, due to high production thresholds ( $\sim 3$  GeV for the process  $\pi\pi \rightarrow \Omega\Omega$ ) and low cross sections [Chia01].

Such different behaviours, in confined and deconfined medium, should allow to understand if a transition phase between the two states occurred.

Experimentally the study of the production of multi-strange particles in Pb-Pb collisions has been performed at CERN by the experiment WA97 which mea-

sured an enhanced abundance of strange particles in Pb-Pb collisions with respect to p-A reactions at 160 AGeV. NA57 extended the WA97 measurements to study the evolution of strangeness enhancement as a function of the beam energy and over a wider centrality range [Eli01].

This experiment uses an extremely granular detector made by 13 pixel detector planes to track the particles from strange and multi-strange hyperon decays. In fact they will be reconstructed thanks to their weak long lifetime decays into final states with charged particle only (e.g.  $\Xi^- \rightarrow \Lambda \pi^-$ , with  $\Lambda \rightarrow \pi^- p$ ) [Eli01]. The secondary decay product can be therefore separated from the much more numerous primary collision products, drastically reducing the combinatorial background. NA57 collected data on Pb-Pb collisions at both 160 and 40 AGeV/c beam momentum and on p-Be at 40 GeV/c. The measurements of WA97 for p-Be and p-Pb at 160 GeV/c are used as reference data. In fig. 1.11 results from WA97 and NA57 experiment are shown.

Figure 1.11: *Hadrons and hyperon yields relative to p-Be collisions as a function of participant nucleons from WA97 for all measured particle (closed symbols) and from NA57 for  $\Xi^-$  and  $\Xi^+$  (open symbols) [Eli01].*

The hadron and hyperon yields in Pb-Pb collisions, relative to p-Be interactions, are displayed. As predicted in case of QGP formation, the enhancement is larger for particles of higher strangeness content, up to a factor of about 15 for the  $\Omega$ , which contains the highest number of strange quarks [And99]. So far no microscopic hadron collision model has reproduced these observations. In the common centrality region the NA57 yields are about 20% larger than the WA97 ones: this difference is under investigation. The sudden drop for  $\Xi^+$ , which

could indicate the point of QGP phase transition, is currently under study. An investigation on  $\Lambda$  and  $\bar{\Lambda}$  on the same sample is under way. The doubled statistics of year 2000 will allow later to perform the analysis of  $\Omega$  hyperons and to reduce the error bars on the  $\Xi$  yields.

## 1.6 Charmonia suppression

The suppression of charmonia (bound states of  $c$  and  $\bar{c}$  quarks) as a signal of deconfinement has been proposed by Matsui and Satz in 1986 [Mat86]. Such states in fact, since they are produced in the early stages of the collisions before the existence of any medium, allow to test the initial conditions of the colliding matter. Moreover they make possible to disentangle between confined and deconfined medium since in the latter their production rate is lower, as we will see later. Their study appears relatively easy through their leptonic decays. In the future RHIC and LHC will produce collisions at energies high enough to make possible an investigation of bottomonia ( $b\bar{b}$  states).

The idea is that if QGP is formed, the interaction potential is screened beyond a certain distance  $\lambda_D$ , due to the presence of quarks, antiquarks and gluons in the plasma. This behaviour is similar to the Debye screening of an electric charge in QED where the potential of a charge is screened by the field of the electrons which surround it. Moreover in the QGP the string tension vanishes and the confinement effect disappears.

If we consider a  $J/\Psi$  as a two-body system made by a charm quark interacting with an antiquark, in absence of QGP, the resulting potential will be [Won94]:

$$V(r) = \frac{q}{4\pi r} + \sigma r \quad (1.14)$$

This is the sum of a Coulomb potential and of a confining potential between  $c$  and  $\bar{c}$ , which increases with the distance.  $\sigma$  represents the string tension coefficient.

Considering the  $J/\Psi$  in a QGP state the potential will be modified from the long-range potential to a short Yukawa potential:

$$V(r)_{QGP} = \frac{q}{4\pi} \frac{e^{-r/\lambda_D}}{r} \quad (1.15)$$

The Debye screening length  $\lambda_D$  represents the range up to which the interaction between  $c$  and  $\bar{c}$  is effective. Above this value the interaction diminishes exponentially with distance. When the resonance dimensions are bigger than  $\lambda_D$  the dissociation of quark and antiquark pairs is possible.

$\lambda_D$  is inversely proportional to the temperature and in fig. 1.12 this behaviour is shown. The straight lines, which intersect the  $\lambda_D$  curve, represent the dimensions of some charmonium states. When the critical temperature is exceeded,  $c$  and  $\bar{c}$  binding is broken, starting from the most weakly bound state.

Figure 1.12: Debye radius as a function of  $T/T_c$ . The lines correspond to the critical Debye radius for different charmonium states.

Such quarks then combine with light quarks or antiquarks and hadronize as open charm mesons like  $D$  ( $c\bar{u}$  and  $c\bar{d}$ ),  $\bar{D}$  ( $\bar{c}u$  and  $\bar{c}d$ ),  $D_s$  ( $c\bar{s}$ ) and  $\bar{D}_s$  ( $\bar{c}s$ ). The different binding energies of the  $c\bar{c}$  involve a hierarchy of suppression. In fact  $\Psi'$  and  $\chi$  start to be suppressed at lower temperatures, with respect to  $J/\Psi$ , since they are more loosely bound.  $J/\Psi$ , since is smaller and more tightly bound, starts its dissociation process at about  $1.2 T_c$ . As the temperature increases more bound states will melt and such trend can be also used to estimate the temperature system.

The  $J/\Psi$  suppression is characterized by a threshold effect and so a sharp onset in its suppression pattern will be shown. Moreover  $J/\Psi$  can be directly produced or can come from the decays of other excited states ( $\sim 32\%$  from  $\chi_c$  and  $\sim 8\%$  from  $\Psi'$ , in nucleus-nucleus collisions). A multi-step suppression pattern is therefore expected.

The most important results concerning the study of charmonia suppression as a signature of QGP formation have been probably obtained by NA50 experiment at CERN, with Pb-Pb collisions at 158 GeV per nucleon, about a 32 TeV total energy.

The experimental set-up is mainly made by a dimuon spectrometer complemented by several centrality detectors. The most of charged particles produced in

the collisions are absorbed by an iron wall, except muons. In fact  $J/\Psi$  is detected through its decay in two muons, with a Branching Ratio ( $\simeq 5.88 \pm 0.10$ )%.

A "normal" suppression of the production of  $J/\Psi$  has been already observed in experiments which used lighter ion beams and in p-A collisions. This is attributed to nuclear absorption. In fact, the produced resonances can suffer several collisions with the target nucleons and be absorbed [Khar96].

In fig. 1.13 the Branching Ratio for  $J/\Psi$  production divided by the product of projectile and target number of mass is shown as a function of such product. The data well reproduce the theoretical behaviour foreseen for the "normal" absorption in different collisions, from p-p to S-U, except for Pb-Pb. The point corresponding to Pb-Pb collisions seems in fact to indicate a departure from the nuclear absorption curve and so an anomalous suppression.

Figure 1.13:  $J/\Psi$  cross section per nucleon-nucleon collisions as a function of the  $AB$  product of the projectile and target atomic mass numbers.

Let's now take into account all the data concerning Lead-Lead collisions as a function of the event centrality. In NA50 this can be evaluated by measuring the energy released in the Zero Degree Calorimeter ( $E_{ZDC}$ ) by the non participating nucleons and is directly proportional to the number of spectator nucleons.

The Branching Ratio for  $J/\Psi$  production normalised to Drell-Yan<sup>5</sup> as a function of the  $E_{ZDC}$  is plotted in fig. 1.14 ( [Arn00], [Abr01]). The solid line rep-

---

<sup>5</sup>It consists of an electromagnetic annihilation of a valence quark and a sea antiquark sharing

resents the prediction for nuclear absorption. A first departure from it, followed by a second decrease, is clearly visible. This deviation becomes more and more important as the centrality increases (low  $E_{ZDC}$  values).

Figure 1.14: *The ratio  $J\Psi/DY$  as a function of the energy released in the Zero Degree Calorimeter is shown. A two step-pattern, foreseen for a deconfinement scenario, is visible ( [Arn00], [Abr01]).*

These results have been also obtained by an independent analysis where the centrality of the collision has been estimated by means of the transverse energy released in the electromagnetic calorimeter (fig. 1.15).

It has been tried to explain such behaviour with many purely hadronic models without deconfinement [Abr00]. The idea is to add a contribution given by dissociation of  $J/\Psi$  in final state hadronic interactions with comovers via the inelastic reaction:

$$J/\Psi + h \rightarrow D\bar{D} + X \quad (1.16)$$

---

the same flavour, which results in a lepton pair. Such process is often used as reference to study the  $J/\Psi$  production behaviour since its insensitivity to the final state interactions in pA and AB collisions.

Figure 1.15:  $J/\Psi/DY$  ratio as a function of  $E_T$ . The Pb-Pb data are compared to several theoretical calculations.

Several models have been developed, essentially based on different estimation of the comovers density. All such calculations reproduce in a good way the  $J/\Psi$  suppression from pA to central S-U collisions, but not the data coming from Pb-Pb collisions at large centrality values (fig. 1.15).

## 1.7 Have we found the QGP?

As shown up to now at  $\tau_0$  ( $\sim 1$  fm/c) we have an estimated initial energy density of about  $3 \text{ GeV/fm}^3$ , for a system created in a central Pb-Pb collision at the SPS. Theoretically such state should be QGP.

At chemical freeze-out the temperature is about 170 MeV and inelastic interactions stop. The chemical composition of the system in terms of produced particles is frozen. It is still possible to have elastic interactions so the momenta can be redistributed between particles but the composition cannot be changed. This happens at energy density of about  $1 \text{ GeV/fm}^3$ . At this point strangeness production has been enhanced and  $J/\Psi$  production has been suppressed.

At freeze out, when elastic interactions stop, the system is expanding at more than  $1/2$  the speed of the light, showing a large pressure buildup.

Between  $\tau_0$  and the chemical freeze-out the system is in a state of very large energy density and the individual hadrons can penetrate each other. The concept of individual, separated, hadrons is therefore not more meaningful.

The properties of the formed state are not explained in terms of those of a conventional system of strongly interacting hadrons. This state shows many features of the QGP, in particular the expected effect of deconfinement ( $J/\Psi$  suppression and strangeness enhancement).

Many of the predicted features of QGP are showed by the system formed in Pb-Pb collisions at the SPS but...the evidence is indirect and we have no clear evidence yet of thermal QGP radiation. To better understand the properties of this state we need to go at higher energies, deeper into the deconfinement regime, where comparison with theory and interpretation of data are expected to be much more clear. Probably an ideal QGP itself is a too crude description of the data and in this field more has to be investigated.

We certainly cannot rule out that other explanations may be found which describe the observed phenomenology and in any case our picture of hadronic interactions is going to change [Ant01].

At SPS it should be further investigated the onset of effects already observed as a function of  $N_{part}$  energy and measurements with intermediate mass ion beams and at different beam energies should be done.

The NA50 experiment will be upgraded with a pixel vertex detector to measure dimuon production and in particular open charm [NA60].



## 1.8 The present (RHIC) and the future (LHC)

The Relativistic Heavy Ion Collider (RHIC) at Brookhaven National Laboratory switched on on June 2000. Au ions travel in opposite directions around RHIC's 2.4 miles. The nucleon-nucleon center of mass energy is 200 GeV, a factor 10 larger than what it is achieved at SPS. Higher energy densities and temperatures, larger expected deconfined phase lifetimes and volumes will be obtained.

QCD calculations become more reliable and our understanding and interpretation of data should improve. Unlike SPS and LHC accelerators, where heavy ion beams are typically available for 1 month per year, RHIC is a facility all year-round dedicated. It will be also possible to have energy scans and p-A and A-B collisions.

STAR is one of the two-large scale experiments at RHIC. It searches for signatures of Quark Gluon Plasma formation and investigates the behaviour of strongly interacting matter at high energy density by focusing on measurements of hadron production over a large solid angle. PHENIX is designed to detect, identify, and measure the momentum of each of the many different kinds of particles produced at RHIC and in particular it looks for leptonic and electromagnetic signals. There are also 2 smaller experiments, PHOBOS and BRAHMS. The PHOBOS detector will be able to measure quantities such as the temperature, size, and density of the fireball produced in the collision. It will also study the ratios of the various particles produced. The BRAHMS experiment is designed to measure charged hadrons over a wide range of rapidity and transverse momentum to study the reaction mechanisms of the relativistic heavy ion reactions.

The most interesting research areas will concern strange and multistrange field (the number of strange quarks at central rapidity could be equal to up and down quarks). For what concerns the electromagnetic area it could be possible to see the radiation of QGP.

LHC accelerator, at CERN, is expected to turn on in 2006 and to accelerate heavy ion beams in 2007. There will be a multi-purpose experiment entirely dedicated to QGP study: ALICE. Their detailed description will be given in the next chapter.



## Chapter 2

# The ALICE experiment

Physicists are already searching for signs of the Higgs boson or supersymmetric particles in existing colliders. However, to investigate properly these and other new phenomena it is required a collider that will achieve much higher energies - 70 times that of LEP - replicating the conditions in the Universe about 10  $\mu$ s after its birth. This accelerator, the Large Hadron Collider (LHC), is now being built by international teams of all over the world. Constructed in the same underground 27 km long LEP, it will be ready by 2006.

Protons will be delivered by SPS and its pre-accelerators at 0.45 TeV. They will be later accelerated up to 7 TeV by 5000 superconducting magnets and will rotate for several hours, colliding at each experiment. Heavy ions, like Lead, will be also accelerated, achieving a 5.5 TeV center of mass energy per pair of nucleons, a value about 30 times higher than at RHIC and 300 times higher than at SPS.

The foreseen luminosity will be  $10^{34}\text{cm}^{-2}\text{s}^{-1}$ , two orders of magnitude greater than the maximum value presently achievable in a p-p collider. The LHC ring will be filled with 2835 bunches of  $10^{11}$  particles each, resulting in a large beam current ( $I_b = 0.53$  A). At the intersection of colliding beams four experiments will detect the incoming particles: ALICE, ATLAS, CMS and LHCb. In fig. 2.1 a layout of LHC structure is represented.

ATLAS and the Compact Muon Solenoid (CMS) will aim to observe the Higgs and supersymmetric particles, while LHCb will search for B-mesons to explain the asymmetry in particle behaviour that explains the missing antimatter in the Universe. ALICE experiment will study the extreme state of matter known as Quark Gluon Plasma.

Thanks to a highly sophisticated superconducting technology LHC combines, for the first time, a large beam current at very high energy. In these conditions many “beam troubles” could arise, like the beam-beam effect and a loss of beam particles due to the effect of strong electromagnetic field of the opposite bunch.




Figure 2.1: View of LHC accelerator.

Any initial disturbance in the position and energy of a bunch, caused by the electromagnetic *wake-field* left behind by the previous bunch, can be amplified, leading to beam loss. These *collective instabilities* can be severe in LHC since the high luminosity needs a large beam current. Such effects can be minimized checking the electromagnetic properties of the elements which surround the beam.

In addition to collective instabilities spurious non linear components of the guiding and focusing magnetic field can result in a chaotic beam motion. An efficient collimation system must be used to avoid particle diffusion into the beam pipe wall. Moreover, this would lead to a conversion of particle energy into heat and to a quench of superconducting magnets.

The power emitted by synchrotron radiation will be not negligible and will be absorbed by the beam pipe at cryogenic temperature, affecting the refrigeration system.

## 2.1 The ALICE detector

ALICE (A Large Ion Collider Experiment) is the experiment of LHC dedicated to the study of heavy ion collisions [ALITP]. Its main goal is to investigate the behaviour of nuclear matter at high densities and temperatures. In particular it should allow to study QGP formation and its dynamical evolution, phenomena associated with the phase transition of rehadronization and the evolution of the hadronic final state until freeze-out. It will measure a large set of observables, connected to hadrons and leptons as well as photons.

With respect to RHIC it will be possible to study gluon distribution functions at much lower values of  $x_t$  ( $x_t=2p_t/\sqrt{s}=10^{-4}$ - $10^{-3}$ ). A very high initial gluon density has been estimated and up to 4000 gluons per unit rapidity near mid-rapidity are expected [Esk94]. This should lead to a fast equilibration on a time scale of 0.1 fm/c, an initial energy density of the order of 1000 GeV/fm<sup>3</sup> and a temperature of 1 GeV [Shu92].

As a consequence of the high gluon densities at small  $x_t$  at LHC the cross sections for charm, beauty and semi-hard jet production are more than one order of magnitude greater with respect to RHIC [TRD].

From a theoretical point of view it is very difficult to estimate the number of charged particles produced during the collisions. In fact, such beam energies have not yet achieved before, even for proton-proton collisions, and the gluon distribution functions have not been yet measured in nuclei for such  $x_t$  values.

Moreover first results from RHIC as a function of centrality indicate a dependence on the number of participating nucleons in a complicated way, containing a linear and a quadratic term ([Adc01], [Bac01]). It is therefore necessary to estimate the overall centrality dependence in an accurate manner in this range of energy. Estimates based on Glauber models gave values up to  $dN_{ch}/dy=8000$  for Pb-Pb collisions while more recent calculations (based on Gribov-Regge theory) give a value three times lower [TRD].

A multiplicity function, scaling with beam energy, has been derived from 130 GeV data and has been successfully verified at the full RHIC energy (200 GeV). If an extrapolation to LHC energies is made a multiplicity of about 2000 particles for Pb-Pb collisions is expected.

ALICE experiment has been designed to be able, in any case, to cope with the maximum estimated rapidity density of primary charged particles averaged over two units of rapidity ( $-1 \leq y \leq 1$ ), which is equal to 8400 [TRD].

The detector mainly consists of three parts (fig. 2.2):

- The central region, housed in the L3 magnet, which covers the pseudorapidity<sup>1</sup> range  $-0.9 < \eta < 0.9$ . It is dedicated to the study of hadronic signals, dielectrons and photons.
- The forward muon spectrometer, to identify the muon pairs coming from heavy resonance decays, in the range  $2.5 < \eta < 4.0$ .

---

<sup>1</sup>In the ultrarelativistic limit, where the particle momentum is larger than the mass, the rapidity  $y$  is well approximated by the pseudorapidity  $\eta$ :

$$\eta = -\ln\left(\tan\frac{\theta}{2}\right), \quad (2.1)$$

where  $\theta$  is the angle between the particle momentum and the beam axis.

- The forward detectors ( $\eta > 4.0$ ), to evaluate the photon and charged particle multiplicity and the collision centrality.

## 2.2 The central barrel

The central region is inside a magnet, the same used for L3 experiment. It is a large size solenoid (inner radius  $\sim 5$  m) with a weak field. The field strength, 0.2 T, is a compromise between good momentum resolution, low momentum acceptance and tracking efficiency. It would be possible to identify and track particles down to a transverse momentum  $\sim 100$  MeV [ALITP].

This central region is made by an Inner Tracking System of Silicon detectors (ITS), a large Time Projection Chamber (TPC), a Transition Radiation Detector (TRD) and a Time Of Flight array (TOF). Close to mid-rapidity there will be also two single arm detectors: a RICH counter (Radiation Imaging CHerenkov) for the High Momentum Particle IDentification (HMPID) and an array of crystals for Photon detection (PHOS).

We give in the following a description of the capabilities of each subdetector.

### 2.2.1 Inner Tracking System (ITS)

The Inner Tracking System will allow to [ITS]:

- determine the primary vertex and the secondary ones to reconstruct charm and hyperon decays;
- identify and track the low-momentum particles which do not reach the TPC;
- improve the momentum and angle measurements of the TPC for the HBT analysis.

To achieve an efficient track finding and impact parameter resolution the detector will be made by six cylindrical layers of silicon detectors covering the central rapidity region ( $|\eta| \leq 0.9$ ). In the innermost region the required granularity due to the high particle density (up to 90 particles per  $\text{cm}^2$ ) is achieved with silicon micro-pattern detectors: Silicon Pixel Detectors (SPD) and Silicon Drift Detectors (SDD). Since at larger radii the track densities are below 1 per  $\text{cm}^2$  double-sided Silicon Strip Detectors are used. These detectors must be as thin as possible (0.4 %  $X_0$ ) to avoid multiple scattering effects and to achieve the required signal to noise ratio. The area of the whole detector is  $\simeq 6.74 \text{ m}^2$ , for a total channel number of around  $18 \cdot 10^6$ .

Figure 2.2: *General layout of ALICE experiment.*

The inner radius must be compatible with beam pipe dimensions, while the outer is determined by the track matching with the TPC.

### 2.2.2 Time Projection Chamber (TPC)

The TPC is the main tracking detector of the ALICE central region. It has to satisfy many requirements in order to allow both the hadronic and leptonic observable investigations.

In the first case it should provide informations on the flavour composition of the fireball through the spectroscopy of strange and multi-strange hadrons, on its space-time extent at freeze-out by means of the single-particle and two-particle spectra and correlation studies, and on event-by-event fluctuations of the fireball [TPC].

Together with TRD and ITS it should measure, in the dielectron channel, the production of light and heavy vector meson resonances for Pb-Pb collisions, the overall amount of open charm and open beauty produced in the collision and separate the directly produced  $J/\Psi$  from those coming from B-decay.

This detector has also to cope with a maximum multiplicity of  $dN_{ch}/dy=8000$  charged particles per unit rapidity at midrapidity which should result in 20000 charged primary and secondary tracks in the TPC.

The detector has to cover an overall acceptance of  $|\eta| < 0.9$ . This acceptance value is important for hadronic variable studies like the  $K/\pi$  ratio, from which it could be possible to determine the strangeness content of the fireball. For the dielectron channel it should allow to collect a significative statistics for high mass and high  $p_t$  electron pairs.

The multiwire proportional chambers are the detectors which better satisfy ALICE TPC physics requirements. To fulfill the acceptance constraint the TPC design is cylindrical with an inner radius of  $\sim 80$  cm, an outer radius of  $\sim 250$  cm and a length, along the beam direction, of  $\sim 500$  cm.

The inner radius has been chosen to have a particle density, on the cylinder surface, equal to  $\simeq 0.1$  particles per  $\text{cm}^2$ . The outer one is due to the length required to have a  $dE/dx$  resolution better than 7%, needed to study hadronic and leptonic signals in the region  $p_t < 10$  GeV/c.

It is filled with a gas mixture made by 90 % Ne and 10 %  $\text{CO}_2$  and the High Voltage electrode (up to 100 kV) is located at the axial center of the cylinder. The cathode planes are segmented into small pads. Since the particle track density decreases as the radius increases two different readout chambers, called *inner* and *outer*, will be used. The total channel number will be nearly equal to 570000.



### 2.2.3 Transition Radiation Detector (TRD)

The main aim of the Transition Radiation Detector is the identification of electrons with momentum higher than 1 GeV/c with high efficiency. It will provide, together with ITS and TPC, the following measurements [TRD]:

- the production of light and heavy vector-meson resonances and the di-lepton continuum;
- the semi-leptonic decays of hadrons with open charm and open beauty;
- charm and beauty production over the rapidity range  $y = 0 - 4$  in conjunction with the Forward Muon Arm.

The detector thickness has to be chosen as a compromise between efficient electron detection, minimization of small angle scattering, reduced Bremsstrahlung, showering and mechanical stiffness.

The detector will be made by 540 modules arranged in 18 supermodules. Each of them will contain six layers of detectors subdivided into 5 sections in  $z$  direction. Each module is made by a radiator 4.8 cm thick, a multiwire proportional chamber, and by its readout electronics. The cathode planes are segmented into pads with a  $\sim 6\text{-}7\text{ cm}^2$  area to achieve 80 % tracking efficiency (single track). The total number of readout channels is  $\sim 10^6$ . The TRD will provide a momentum resolution of 5 % at 5 GeV.

### 2.2.4 Time Of Flight (TOF)

The TOF detector will identify hadrons with momentum ranging from 0.5 GeV/c to 2.5 GeV/c through a time of flight measurement. The first value is the upper limit for  $dE/dx$  measurement in ITS and TPC for  $K/\pi$  separation, the second has been chosen to allow an event by event reconstruction.

The chosen detector for TOF is a Multigap Resistive Plate Chamber. A Resistive Plate Chamber is a gas detector with parallel plate chamber with resistive electrodes which quench the streamers. This allows to work at higher gains in avalanche mode [TOF].

In a multigap RPC the total gas gap is split into sub-gaps. It offers the advantage of a large total gas gap (looser mechanical tolerances and improved rate capability) and smaller gaps (time resolution improving).

The ALICE TOF detector will achieve a final time resolution of 150 ps, including all sources of timing errors [TOF].

### 2.2.5 High Momentum Particle Identification Detector (HMPID)

The HMPID will detect pions, kaons and protons in the momentum range 1-5 GeV/c. The HMPID is a single-arm detector, since above  $p_t \sim 1$  GeV/c the expected particle production yield is low. The particle spectra will be studied in an inclusive way since the cross section for high momentum particles is too small to allow an event-by-event analysis [HMPID].

To provide the required momentum range for particle identification a detector based on ring-imaging technique using Cherenkov light will be used.

The detector will be located close to the inner radius of L3 magnet, far from the interaction point, for particle density reasons.

The radiator and the detector geometry are chosen in order to allow particle identification in the required momentum range (from 1 to 5 GeV/c). The  $C_6F_{14}$  has an adequate refractive index and is transparent to Cherenkov photons in this range. The detection of photons will be made by means of a solid CsI photocathode together with a MWPC.

The analog signal will be read out through GASSIPLEX chips (section 4.4.1).

### 2.2.6 Photon Spectrometer (PHOS)

The Photon Spectrometer will be mainly dedicated to the study of photon signals. It will make possible to obtain informations on the initial phase of the collision, in particular about the temperature, via single photons and di-photons. It will also be possible to investigate signals of chiral-symmetry restoration and jet quenching via high  $p_t$   $\pi^0$  and  $\eta$  spectra study. It will measure photons of 0.5-10 GeV/c,  $\pi^0$  of 1-10 GeV/c and  $\eta$  mesons of 2-10 GeV/c.

The detector is a high granularity electromagnetic calorimeter made by 17280 channels of lead-tungstate crystals (PWO), a fast scintillating crystal coupled to Si PIN photodiodes.

It will be located at the bottom of ALICE central barrel and will cover the pseudorapidity region  $|\eta| \leq 0.12$ . Its total area will be  $\sim 8$  m<sup>2</sup> and the total crystal volume  $\sim 1.5$  m<sup>3</sup> [PHOS].

## 2.3 The forward detectors

Many QGP signatures show different features as a function of the energy density (e.g. charmonia and bottonia production, strangeness), estimated through the measurement of the collision centrality. A good resolution on the centrality

measurement is therefore required.

A Photon Multiplicity Detector (PMD) and Zero Degree Calorimeters (ZDC) will complement the central detectors to study the critical phenomena associated with phase transition.

### 2.3.1 Photon Multiplicity Detector (PMD)

The Photon Multiplicity Detector has the following features [PMD] :

- determine the reaction plane and the probes of the thermalization through the study of azimuthal anisotropy and flow;
- study the signals of chiral-symmetry restoration through the measurement of the charged particle multiplicity;
- investigate about some global observable fluctuations near the phase transition, like multiplicity, mean transverse momentum and pseudorapidity distributions;
- estimate the transverse electromagnetic energy  $E_T = \sum_i \Delta E_i \sin \theta_i$ , where  $\Delta E_i$  is the energy deposited by the  $i^{th}$  photon in the sensitive volume of the detector and  $\theta_i$  is the emission angle of the photon in polar coordinates.

This high granularity preshower detector will be located at 5.8 m from the vertex, covering the region  $1.8 \leq \eta \leq 2.6$  at the opposite side of the dimuon spectrometer.

It is subdivided into three parts: a converter, a veto and a preshower. Photons crossing the lead converter start an electromagnetic shower, producing a large signal in some cells of the sensitive detector volume. Hadrons hit only one cell and produce a typical minimum ionizing particle signal. The thickness of the converter has been chosen in order to have a high conversion probability of photons and a small shower transverse size to avoid overlapping in high multiplicity events. In front of the detector a veto is used to reject charged particles.

The preshower and the veto are based on honeycomb proportional chambers. The honeycomb wall forms a common cathode which operates at high negative voltage. The signal is read out from the anode wires (at ground potential) connected to the readout electronics. The gas mixture is made by Argon and Carbon dioxide since it is not sensitive to neutrons and it is not flammable.

A module is made by  $24 \times 24$  hexagonal cells arranged in a rhombus array to provide minimum dead spaces at the boundaries.  $3 \times 3$  unit modules make a supermodule of side 80 cm. The total active area is  $\sim 10 \text{ m}^2$ .

### 2.3.2 Zero Degree Calorimeters (ZDC)

To estimate the collision centrality two set of calorimeters will be used. They are located at opposite sides with respect to the beam interaction point, at nearly 115 m from this. The zero degree calorimeters will measure the energy of nucleons not involved in the collision (spectators). This value decreases as the collision become more central. It is possible to estimate the number of interacting (participants) nucleons by using this simple relation:

$$N_p = A - E_S/E_A \quad (2.2)$$

where  $A$  is the mass number of the ion,  $E_S$  is the energy carried away by the non interacting nucleons (spectators) and  $E_A$  is the beam energy per nucleon.

Each set of calorimeters is composed by a detector for protons and one for neutrons. Due to their different charge to mass ratio it will be in fact possible to separate spectator protons and neutrons from the beam particles with the use of the D1 LHC dipole. Further informations on the centrality of the collision can be provided by an electromagnetic calorimeter which detects the energy carried by photons in the forward direction.

Each detector is made by quartz fibers embedded in a dense material and oriented to  $0^\circ$  with respect to the beam axis. The Cherenkov light produced in the fibers is driven to photomultipliers.

The neutron detectors, due to the constraints imposed by their location in the reduced space between the beam pipes, have dimensions  $7 \times 7 \times 100 \text{ cm}^3$  and use Densimet Tungsten alloy as a passive material.

The proton devices, not subject to stringent geometrical constraints, have larger dimensions ( $20.8 \times 12 \times 150 \text{ cm}^3$ ) and are made by brass.

## 2.4 The forward dimuon spectrometer

In 1995 it has been proposed to upgrade ALICE central detectors with a forward Muon Arm in order to study the complete spectrum of heavy quark vector resonances ( $J/\psi$ ,  $\psi'$ ,  $\Upsilon$ ,  $\Upsilon'$  and  $\Upsilon''$ ) in p-p and heavy ion collisions via their decay into muon pairs [ALIAD].

In fact, as shown in the previous chapter, one of the most important signature of the QGP formation is the anomalous suppression of the  $J/\psi$  resonance. At LHC energies it will be possible to study such phenomena not only for  $c\bar{c}$  but also for  $b\bar{b}$  bound states.

The Muon arm is made by:

- a front absorber;

- 10 tracking planes;
- a large area dipole;
- a muon filter;
- four trigger planes;
- a V0 detector;
- a beam shield.

A schematic view of the Muon Arm is reported in fig. 2.3. A tracking and trigger system view is also shown. The smallest acceptance angle is  $2^\circ$ , due to the beam pipe presence, the biggest is  $9^\circ$ , a good compromise between the acceptance and the cost of the detector [MUOAD].

In the following each element will be described.

### 2.4.1 The absorbers

Three absorber sections are foreseen in the Muon Arm to shield the detectors from the large particle flux: a front absorber in the acceptance region  $2^\circ < \eta < 9^\circ$ , a beam shield which surrounds the beam pipe and a muon filter, just before the trigger chambers.

#### Front absorber

It is located between the first tracking Station and the interaction point. It has to attenuate the hadronic flux by at least two orders of magnitude and the background coming from  $\pi$  and K decays into muons by limiting their free path [ALIAD]. The central part, near the interaction vertex, is made by carbon, to absorb pions and kaons before their decay into muons. A low Z material has been chosen to reduce muon multiple scattering effects, which lead to a worse mass resolution of the spectrometer. The rear region is made by concrete, lead, tungsten and boronated polyethylene to absorb the secondaries produced in the absorber, low energy neutrons and photons.

The outer part is made by lead and tungsten to shield the central ALICE detectors from the particle flux. A part of the shower originated by the particles crossing the absorber could in fact exit from the outer surfaces. It will also absorb muon with momentum lower than 4 GeV/c making impossible their detection.

Figure 2.3: *Forward dimuon spectrometer lateral view.*

### Muon filter

It is made by an iron layer 1.2 m thick and it is put between the last tracking Station and the first trigger planes. Together with the front absorber it will stop muons with momentum lower than 4 GeV/c, to reduce the background due to pions and kaons decay. It will also enhance the trigger chamber performances by stopping the hadrons not absorbed by the front absorber or produced in the beam pipe.

### Beam shield

It has to shield the muon spectrometer detectors from high rapidity particles and secondaries along the beam pipe. It is made by tungsten but, above all, by lead which allows a low cost absorber without increasing the background. It is covered by a stainless steel layer.

## 2.4.2 Dipole magnet

It will deflect muons according to their charge and allow their momentum measurement, which is inversely proportional to their deflection angle. It is 5 m long, 6.6 m wide and 8.6 m high. The central field will be 0.7 T and the integral one  $\geq 3 \text{ T}\cdot\text{m}$ . Such magnet has been preferred to a toroid which would not satisfy the ALICE acceptance requirements. The dipole structure can be used as support for the muon absorber and beam shielding.

## 2.4.3 Trigger chambers

The trigger has to select, amongst the background sources, the events of interest, i.e. the muon pairs coming from a  $J/\psi$  or  $\Upsilon$  decay. The major background source is due to low  $p_t$  muons coming from pions and kaons decay. To reduce it a selection on the  $p_t$  value is applied ( $p_t \geq 1 \text{ GeV}/c$  for muons coming from  $J/\psi$  decay and  $p_t \geq 4 \text{ GeV}/c$  for those coming from  $\Upsilon$  decay).

A *dimuon trigger* is generated when at least two tracks, from opposite sign particles, satisfy the predefined  $p_t$  cuts. The trigger signal must be very fast ( $\leq 1\mu\text{s}$ ) since it is used as strobe signal of the tracking chambers. The trigger information is also used to identify the tracks in the offline analysis.

Amongst different detectors a trigger system based on Resistive Plate Chambers has been chosen<sup>2</sup>. With this device the required granularity of  $\sim 1 \text{ cm}$ , needed to select high  $p_t$  muons from  $J/\psi$  or  $\Upsilon$  and to reject the background, can be obtained.

---

<sup>2</sup>A detector based on scintillator arrays would be more expensive and fragile.

Moreover the RPC sensitivity to gamma and neutrons, produced by showers inside the absorbers and the beam shield, is low (of the order of  $10^{-2}$  and  $10^{-3}$  respectively).

It also shows good timing properties and, thanks to a strong and constant electric field inside the detector, a 20 ns gate can be used, allowing to reject many background hits. In fact the 10% of photons and 1% of neutrons reach the trigger detector 20 ns after the fastest muons.

Simulations showed that the interaction rates will be 3 Hz/cm<sup>2</sup>, 40 Hz/cm<sup>2</sup> and 10 Hz/cm<sup>2</sup> for, respectively, Pb-Pb, Ca-Ca and p-p collisions. Considering also a safety factor, a rate capability of 100 Hz/cm<sup>2</sup> is needed.

The number of adjacent fired channels must be as close as possible to 1 to minimize the occupancy factor and to allow a more selective trigger.

The ALICE trigger system is based on two RPC Stations (MT1 and MT2), 1 m far one from each other, located at  $\sim 16$  m from the interaction point and at 1.2 m from the muon filter. Each Station is made by two 36 m<sup>2</sup> planes of single-gap RPCs working in streamer mode. Two resistive bakelite planes enclose a 2 mm gas layer.

Each plane, segmented into strips, provides the x and y coordinates. The y measures the bending deviation due to the dipole magnetic field, the x the coordinate in the non bending direction [MUO]. The signals are discriminated and sent to the readout electronics to be processed. The trigger decision is taken in  $\sim 600$  ns ( $1.2 \mu\text{s}$  including the processing time of the central trigger processor).

#### 2.4.4 V0 detector

To achieve a better vertex determination and to recognize and reject the background events during p-p run (either online or offline) a V0 detector will be added( [MUOAD], [Che00]).

It will be made by an array of scintillators read out by wavelength shifting fibers and will cover the carbon section of the absorber from  $R_{min}=40$  mm to  $R_{max}=160$  mm.

#### 2.4.5 Tracking chambers

The tracking system is made by ten circular chambers grouped into five Stations. The first two Stations are located after the front absorber, the third is inside the dipole magnet and the last two are between the magnet and the muon filter. Each chamber has two cathode planes which are both read to have a bidimensional hit information.

The INFN Cagliari Group III in collaboration with Nantes (SUBATECH) and Saclay (CEA) French teams and the Russian team of St. Petersburg (PNPI) is



involved in the study, design and realization of the last three Stations.

The best suited detectors for the tracking system have been chosen in order to satisfy many physics, geometrical and technical requirements and they will be illustrated in more details in the following chapters.

Simulations studies and prototype tests, made to achieve the best possible final configuration, are the subject of this thesis.



# Chapter 3

## ALICE tracking chambers

LHC luminosity, for heavy ion collisions, will give rise to low interaction rates but the multiplicity per event will be high. Despite the shielding in Pb-Pb collisions several hundred particles could hit each tracking chamber. They have to detect a small number of muon pairs, coming from heavy resonance decays, with a high spatial resolution and efficiency, in a forward geometry.

A description of the main features of the tracking system for ALICE experiment will be given in the following.

### 3.0.6 Number of hits and trigger rates

Some simulations, using different transport codes, have been performed [MUOAD] to evaluate the number of hits and the maximum hit densities for each Station. For the event generator a particle density, in the central region, of  $dN_{ch}/dy = 8000$ <sup>1</sup> in Pb - Pb collisions has been taken into account. The results from GEANT<sup>2</sup> and FLUKA simulations are presented in table 3.1. A safety factor of 2 has been included to take into account different particle production levels from various codes and the uncertainty in background evaluation. FLUKA results lie at the lower and GEANT at the higher bound [MUOAD]. In these studies a gas mixture of 80% Ar and 20% CO<sub>2</sub> has been used and the heating jacket insulation and the protection of the beam pipe have been included. A more realistic position layout has been also considered for the tracking and trigger Stations with respect to those described in the Technical Proposal [ALITP]. The replacement of the original inner tungsten shield by lead makes the background level decrease in the last two Stations.

In fig. 3.1 the number of particles per unitary area, for the five tracking Stations and the first trigger Station, as a function of Station radius, is plotted.

---

<sup>1</sup>The particles flux has been simulated with HIJING code.

<sup>2</sup>It simulates the detector response [Brun94].

Figure 3.1: *Number of hits per unitary area, for the five tracking Stations and the first trigger Station, versus Station radius [MUOAD].*

Station	Total hits	Max density ( $10^{-2}$ part/cm $^2$ )
1	$400 \pm 40$	5.0
2	$505 \pm 55$	$2.1 \pm 0.1$
3	$250 \pm 20$	0.7
4	$225 \pm 45$	$0.5 \pm 0.05$
5	$265 \pm 35$	$0.6 \pm 0.05$

Table 3.1: *Number of hits and maximum density per unitary area for each Station, obtained by GEANT and FLUKA simulations. A safety factor of 2 is included [MUOAD].*

The radial distribution is not constant and the highest density values are achieved near the beam pipe. The worst case is represented by the first Station which has to work at particle densities up to  $5 \cdot 10^{-2}$  cm $^{-2}$ .

The interaction rates depend on the beam type. In table 3.2 the trigger rates at minimum bias have been reported, for different beam types and at maximal luminosities.

	Pb-Pb	Ca-Ca	p-p
$L$ (cm $^{-2}$ s $^{-1}$ )	$10^{27}$	$10^{29}$	$10^{31}$
Trigger rates (Hz)	8000	$3 \cdot 10^5$	$10^6$

Table 3.2: *Trigger rates as a function of different beam types (minimum bias), at maximal luminosities.*

### 3.0.7 Mass resolution

As explained, one of the possible signature of QGP formation is the suppression of heavy quark vector mesons like  $J/\Psi$ ,  $\Psi'$ ,  $\Upsilon$ ,  $\Upsilon'$  and  $\Upsilon''$ . They could be measured in the spectrometer through their muonic decay.

To separate the  $\Upsilon'$  (10.023 GeV) and  $\Upsilon''$  (10.355 GeV) states a mass resolution better than 100 MeV is required (fig. 3.2).

All the detector features must be chosen in order to mainly satisfy this requirement, as we will show in the following.

Figure 3.2: *Mass spectrum for the  $\Upsilon$ -family. The lower curve represents the muons coming from open beauty decays [ALIAD].*

### 3.0.8 Required detector performances

The mass resolution is mainly determined by the precision achieved in measuring the angle between the two muons and their momenta.

The momentum resolution depends on the precision of the track spatial reconstruction, on the multiple scattering suffered inside the detectors and on the energy-loss fluctuations in the absorber. To achieve the required mass resolution the error on momentum evaluation must be  $\Delta p/p < 1\%$  in the whole momentum range [ALIAD].

The influence of several parameters on the mass resolution has been studied.

#### Spatial resolution

Simulations [MUO] show that in the magnet bending plane (fig. 3.3), i.e. in the  $y$  direction, a spatial resolution better than  $100\ \mu\text{m}$  for each tracking plane, is needed to achieve the required mass resolution (fig. 3.4).

This value must include also misalignments, mechanical deformations, vibrations and so on. If the detector performances improve by a factor two the mass resolution improves only by less than 10 MeV.

In the non bending plane ( $x$  direction) a  $\sim 2\ \text{mm}$  spatial resolution is sufficient

Figure 3.3: Muon Arm schematic view in the  $yz$  plane. The tracking Stations 1 and 2 are placed before the magnet, the Station 3 is inside the dipole and the last two are located before the filter. The muon deflection is visible.

Figure 3.4: Mass resolution, in the  $\Upsilon$  region, as a function of tracking chamber spatial resolution [MUO].

to reconstruct the angle between the two muons and their trajectories in an efficient way.

### Thickness

The mean detector thickness must be below 2 - 3 %  $X_0$ <sup>3</sup> to limit multiple scattering effects and therefore to avoid spatial resolution degradation which leads to a mass resolution worsening.

In fig. 3.5 the correlation between chamber thickness and mass resolution is plotted.

Figure 3.5: *Mass resolution, in the  $\Upsilon$  mass region, as a function of each tracking chamber thickness [MUO].*

If the detector thickness is doubled the worsening at  $\Upsilon$  mass is only  $\sim 10$  MeV but thicker chambers could be more sensitive to  $\gamma$ 's.

### Efficiency

Simulations show that, to reconstruct single tracks with a  $\sim 97\%$  efficiency, chambers must have an intrinsic efficiency of  $\sim 95\%$  [MUO]. For a chamber efficiency of  $\sim 82\%$  the reconstruction efficiency drops to  $\sim 50\%$ .

---

<sup>3</sup>The radiation length  $X_0$  is defined as the distance over which a high-energy ( $> 1$  GeV) electron loses on average 63.2% of its energy to Bremsstrahlung [Wig].



## Chamber sizes

Muons will be detected in the angular acceptance  $2^\circ$ - $9^\circ$ . The active area of the first two Stations is simply the geometrical projection of this cone. The third Station dimensions are limited by the internal dipole clearance and the last two Stations are bigger since they have to detect muons after their deflection in the magnet. The active surface for each tracking Station is reported in table 3.3.

Station	Position along z direction (mm)	Inner diameter (mm)	Outer diameter (mm)	Number of channels
1	5400	364	1766	119.368
2	6860	464	2290	104.084
3	9750	630	3088	165.376
4	12871	790	4182	217.856
5	14270	790	5220	257.024

Table 3.3: *Main tracking chambers features [Tou01].*

These detectors have also to provide a low sensitivity to photons and neutrons background to keep the number of hits to a reasonable level, to reduce the dead time and enhance the detection efficiency.

### 3.0.9 Detector choice

Different detectors have been considered and their feasibility investigated ([Cus97], [Cus98]). The device which better satisfies the above mentioned requirements is a multiwire proportional chamber with segmented cathodes (**Cathode Strip Chamber**). The particle coordinates are determined by calculating a weighted mean of the charge induced on cathode strips. The major advantage of this detector is the possibility to segment the cathode planes as a function of local hit density, which varies as a function of chamber radius. It can also be equipped with a high granularity readout and achieves the required spatial resolution ([Bal99], [Ger99]). Moreover this detector reduces the problem of ghost hits, mainly present in large surface detectors (section 4.3).

Since the study of the last three tracking chamber Stations is the subject of this thesis a detailed description of this kind of detector will be given in the remaining part of this chapter.

Some chamber features will be illustrated with simulation results obtained by using Garfield program [Gar], which provides a simple description of the detector

by means of planes and wires. It can be interfaced to other programs, like Magboltz [Mag] and Imonte to study the drift velocity and the diffusion of electrons and Heed [Hee] to simulate ionisation processes in gas when a particle crosses the chamber.

## 3.1 Gaseous ionization detectors

Until the 70's particle trajectories were reconstructed by means of optical detectors like photographic emulsions or bubble chambers. The events were recorded on films and then examined one by one. This procedure was time consuming and allowed to analyse only a limited number of events.

In 1968 Charpak and his collaborators [Cha68] showed that each of many anode wires in the same detector, closely spaced, can act as an independent proportional counter, called *multiwire proportional chamber*.

The detector properties, mainly the excellent time and spatial resolution, were immediately recognized and it was quickly adopted in high energy physics experiments.

The microelectronics development later helped in getting through one of the detector limit, the great number of electronics channels with which it has to be equipped.

### 3.1.1 Energy loss in thin detectors

When a fast heavy charged particle crosses a gaseous or condensed medium many processes can occur, the electromagnetic ones being the most probable.

It can suffer a deflection from its original direction due to the interaction with nuclei but the energy transfer in this collisions is very small, owing to the large nuclei masses.

The particle mainly loses energy through inelastic collisions. The energy transfer from the particle to the atom can cause its ionization or excitation. These events can be classified as *soft* collisions, in which only an atom excitation occurs and *hard* collisions in which there is a release of electronic charges (ionization). In some of these last reactions the electron itself can have sufficient energy to produce secondary ionization. These high energy electrons, with an energy above a few keV, are called  $\delta$  electrons.

The average energy loss per unit path length has been calculated by Bethe, Block and other authors [Rit61] by using a quantum mechanical approach:

$$\frac{dE}{dx} = -K \frac{Z}{A} \frac{\rho}{\beta} \left\{ \ln \frac{2mc^2 \beta^2 E_M}{I^2 (1 - \beta^2)} - 2\beta^2 \right\} \quad (3.1)$$

where

$$K = \frac{2\pi N z^2 e^4}{mc^2}. \quad (3.2)$$

$I$  represents the mean excitation potential and varies with  $Z$  in a complicated way. It has been evaluated for many gases and tabulated.

$E_M$  is the maximum energy transfer in a head-on collision and depends on the incident particle mass and on its velocity (through  $\beta = v/c$ ):

$$E_M = \frac{2mc^2\beta^2}{1 - \beta^2} \quad (3.3)$$

This kinematical expression cannot always be used, especially in case of thin detectors where  $\delta$  electrons can escape and the maximum energy transfer is not therefore dissipated inside the detector.

The theoretical calculation in this case has been done by Landau [Lan44] and the analytical expression for the energy-loss distribution is the following:

$$f(\lambda) = \frac{1}{\sqrt{2\pi}} e^{-\frac{1}{2}(\lambda + e^{-\lambda})} \quad (3.4)$$

The variable  $\lambda$  represents the deviation from the most probable energy loss  $(\Delta E)_{mp}$  and equals:

$$\lambda = \frac{\Delta E - \Delta E_{mp}}{\xi} \quad (3.5)$$

where  $\xi = K \frac{Z}{A} \frac{\rho}{\beta^2} X$  is the mean energy loss given by the first term in Bethe-Block formula and  $\Delta E$  is the actual loss.

A large amount of energy can be transferred in a single collision as there is also the possibility, for electrons, of a large *one-shot* energy loss for Bremsstrahlung [Leo87]. These events, though rare, determine an asymmetric shape of the distribution, with a long high energy tail (fig. 3.6).

Due to this long tail the mean energy does not correspond to the peak position (which defines the most probable energy).

The long tail, corresponding to the production of  $\delta$  electrons, requires the use of a readout electronics with a large dynamic range, as will we see later.

### 3.1.2 Primary and total ionization

When a particle crosses a medium it can ionize the molecules and create electrons and ion pairs. This is called *primary* ionization. Such electrons can have sufficient energy to further ionize the medium and to produce *secondary* electron-ion pairs. The sum of this two contributions is called *total* ionization.

Figure 3.6: *Energy loss distribution for a thin absorber.*

Since some energy is spent in excitation processes, the number of total produced ion pairs  $n_T$  is not simple the ratio of energy loss ( $\Delta E$ ) to the ionization potential, but an average value ( $W_i$ ) for this last term has to be taken into account:

$$n_T = \frac{\Delta E}{W_i} \quad (3.6)$$

For gases this average value does not depend in a strong way on the particle type and only weakly on the gas type. It is of the order of 1 ion-electron pair per 30 eV energy lost in the gas.

If we now consider a gas mixture made, for example, by 80 % Ar and 20 % CO<sub>2</sub>, the number of primary ion pairs produced in 1 cm by a minimum ionizing particle, will be given, with a simple composition law, by the ratio of  $dE/dx$  to  $W_i$  [Sau77]:

$$n_p = 29.4 \times 0.8 + 34 \times 0.2 \simeq 30 \text{ pairs/cm} \quad (3.7)$$

The number of total ion pairs is obtained by eq. 3.6:

$$n_T = \frac{2440}{26} \times 0.8 + \frac{3010}{33} \times 0.2 \simeq 93 \text{ pairs/cm} \quad (3.8)$$

This implies that the mean distance between two primary interaction is  $\simeq 330 \mu\text{m}$  and that each primary pair produces nearly 2 secondaries.

### 3.1.3 Drift of charges in gas

In absence of electric field, electrons and ions produced by a crossing particle diffuse uniformly, lose their energy in multiple collisions with gas molecules and come into thermal equilibrium with them. The average thermal energy is  $\varepsilon_T = 3/2 kT \simeq 0.04$  eV and the Maxwell distribution leads to a mean velocity  $v = \sqrt{\frac{8kT}{\pi m}}$ . The electron velocity is thus nearly equal to  $10^7$  cm/sec at room temperature while ions, due to their mass, move much slower.

For the detector efficiency it is very important that ion-electron pairs stay in a *free* state a time sufficient to be collected. In fact, without electric field, positive ions will recombine either with negative charges of the gas volume, or with electrons extracted from the gas container walls.

Electrons can recombine with positive ions, can be absorbed in the walls or be captured by electronegative atoms to form negative ions. The probability of attachment is nearly zero for all noble gases and hydrogen. Its value for the other gases has been evaluated and tabulated [Tow47]. Attachment takes place in a time  $t = (hN)^{-1}$ , where  $N$  is the number of collisions per unit time and  $h$  the attachment coefficient. This is a function of the electric field, as shown in fig. 3.10 (dark grey curve).

When an electric field is applied electrons and ions are accelerated and move along the field lines. During this motion their increasing velocity is limited by the collisions with gas molecules. Therefore they reach an average velocity, also known as *drift velocity* ( $w$ ). It is useful to introduce a quantity called *mobility* ( $\mu$ ), defined as the ratio of the drift velocity ( $w$ ) to the electric field strength ( $E$ ). For positive ions  $w$  linearly depends on the reduced electric field  $E/P$ , where  $P$  is the pressure, up to high fields. At a constant pressure the mobility is constant and up to very high fields it does not depend on  $E$  since the ions average energy does not substantially changes. In fig. 3.7 the ion mobility, as a function of  $E$ , is plotted for a gas mixture made by Ar 80 % and CO<sub>2</sub> 20 %.

Electrons instead can increase their energy when they collide with gas molecules under the action of the electric field, due to their low mass. Their mobility is therefore a function of  $E$ .

At high fields a typical electron mobility equal to 5 cm/ $\mu$ s is attained while ions are around 1000 times slower. The behaviour of drift electron velocity as a function of the electric field is shown in fig. 3.8.

During the drift process electrons diffuse following a Gaussian distribution. A change in the energy distribution due to the electric field gives rise to a diffusion coefficient depending on  $E$ . A small value allows to localize the drifting swarm with a best accuracy. The limiting accuracy is not given by  $\sigma_x$  (the standard deviation of space diffusion) but by its variance  $\sigma_x/\sqrt{n}$ . In fig. 3.9 the longitudinal and transverse diffusion coefficient as a function of the electric field are plotted.

Figure 3.7: *Ion mobility vs  $E$ , for a gas mixture made by Ar 80 % and CO<sub>2</sub> 20 %, at normal conditions.*

Figure 3.8: *Drift electron velocity vs  $E$ , for a gas mixture made by Ar 80 % and  $\text{CO}_2$  20 %, at normal conditions.*

Figure 3.9: *Diffusion coefficients (transverse, in dark grey; longitudinal, in light grey) vs  $E$ , for a gas mixture made by Ar 80 % and  $\text{CO}_2$  20 %, at normal conditions.*



### 3.1.4 Avalanche formation

For electric fields above a few kV per cm the electrons coming from primary ionization can produce inelastic phenomena, excitation and secondary ionization. This secondary electrons can have sufficient energy to further ionize gas molecules producing tertiary ionization and so on, starting an avalanche process.

Before starting a secondary ionization an electron has to travel a mean free path. The inverse of this value,  $\alpha$ , represents the number of produced pairs per unit path length and it is known as *first Townsend coefficient*.

After a mean free path  $\alpha^{-1}$  one electron-ion pair is produced and two electrons will drift and again, after a distance  $\alpha^{-1}$ , each of them will produce another electron-ion pair and so on. If  $n$  is the number of electrons at a certain position after a path  $dx$ , there will be an increase in the number of electrons equal to:

$$dn = n\alpha dx \quad (3.9)$$

By integrating this expression the total number of electrons created in a path  $x$  will be:

$$n = n_o e^{\alpha x} \quad (3.10)$$

where  $n_o$  is the original number of electrons. The *multiplication factor*  $M$  (or gas gain) is defined as:

$$M = \frac{n}{n_o} = e^{\alpha x} \quad (3.11)$$

In case of a non uniform electric field a more general expression can be used:

$$M = \exp\left[\int_{x_1}^{x_2} \alpha(x) dx\right] \quad (3.12)$$

This value cannot increase indefinitely, since secondary processes like photon emission (which could generate an avalanche spread) and electric field deformation could occur and generate a spark breakdown. Generally it happens for  $M \sim 10^8$  which corresponds to  $\alpha x \sim 20$ . This is also known as Raether condition.

Various theoretical models have been developed to calculate  $\alpha$  for different gases [Kow85] but there are no simple rules to calculate this coefficient for gas mixtures.

In fig. 3.10 the Townsend coefficient (in light grey), for a gas mixture made by Ar 80 % and CO<sub>2</sub> 20 %, at normal conditions, is plotted as a function of the electric field.

A threshold effect in this plot is evident. The Townsend coefficient is in fact, different from zero only for  $E \geq 2 \cdot 10^4$  V/cm.

Figure 3.10: *Townsend coefficient (in light grey) and attachment coefficient (in dark grey) as a function of the electric field, for a gas mixture made by Ar 80 % and CO<sub>2</sub> 20 %, at normal conditions.*

## 3.2 Multiwire proportional chambers

If a particle crosses a layer of gas 1 cm thick nearly 100 ion pairs are produced. If this charge is collected the signal will be too low to be detected. Applying an electric field between two electrodes an avalanche formation will occur and the signal will be increased by several orders of magnitude.

A cylinder filled with gas, with a central anode wire positive with respect to the outer electrode, is usually called a proportional counter. In this detector the spatial particle localization is however limited. It would be possible to use many counters placed side by side to increase it but, from the mechanical point of view, this structure is not practical and easy to handle. Charpak and his collaborators showed that a detector made by many wires, closely spaced, works properly. In fact the positive charge induced at the electrodes surrounding the wire where the avalanche takes place greatly exceeds the signals coming from capacitive coupling in the neighbouring wires.

### 3.2.1 Operating principles

A chamber is made by a central anode plane, made by wires equally spaced, sandwiched between two outer cathode planes made by wires or by metallic surfaces. Generally the cathode planes are equally spaced from the anode plane. When, for example, a positive potential is applied to the wires and the cathode planes are grounded an electric field is settled in. In fig. 3.11 the electric field lines for a multiwire chamber are shown. In this detector the wire pitch is 2.5 mm, the distance between the anode and each cathode plane is again 2.5 mm ( $y = \pm 0.25$  cm), the wire diameter  $20\ \mu\text{m}$  and the  $\text{HV} = 1650$  Volt.

The electric field maximum value is reached at the wire surface and decreases as  $r^{-1}$  (fig. 3.13).

When a particle crosses the detector a primary ionization starts. The electrons and ions follow the field lines towards, respectively, the anode wires and the cathode planes. Near the wires the field becomes stronger and stronger and the multiplication process can occur: electrons are quickly collected (within  $\sim 1$  ns) and positive ions (half of them produced in the last mean free path) slowly drift towards the cathodes.

In fig. 3.12 a particle crossing a chamber is plotted. The electron drift lines, as reconstructed by Garfield, are also illustrated.

As already shown the Townsend coefficient is different from zero only for  $E \geq 2 \cdot 10^4$  V/cm (fig. 3.10). This value in the chamber is reached at  $\sim 120\ \mu\text{m}$  from the wire center (fig. 3.13).

This means that the avalanche formation starts only at a few wire radii. The avalanche extension along the wire is between 0.1 and 0.5 mm. The ions

Figure 3.11: *Electric field lines in a multiwire proportional chamber. The numbers in the field lines refer to the potential value.*

Figure 3.12: *Electron drift lines from a particle crossing the chamber.*

Figure 3.13: *Electric field shape near a wire: the field is radial.*

surrounding the wire will modify the field in this region and it will be completely restored only after ion neutralization at cathodes (after several hundred  $\mu\text{s}$ ).

The chamber multiplication factor (eq. 3.12) is now:

$$M = e^{\int_a^{r_c} \alpha(r) dr} \quad (3.13)$$

where  $a$  represents the anode wire radius and  $r_c$  the starting point of the avalanche.

It is important to underline that the pulse signal in the detector (negative at the anode and positive at the cathodes) is the consequence of a change in the energy system due to the movement of ions and electrons as they migrate to the electrodes, rather than to the charge collection itself.

The induced charge will be amplified and then digitized by the readout electronics.

### 3.2.2 Choice of the filling gas

In principle any gas can be used in a multiwire proportional chamber but experimental requirements (low working voltage, high gain, long lifetime, etc.) restrict the choice to only a few of them.

In noble gases avalanche formation begins at lower field values with respect to polyatomic molecules. This is a consequence of non-ionizing modes through which complex molecules can dissipate energy.

The most frequent choice is Argon, due to its high specific ionization and low cost (with respect, for example, to Xenon and Krypton). For gains higher than  $10^3 - 10^4$  this gas shows permanent discharges. In fact during the avalanche formation the Ar excited molecules return to the ground state only through a radiative process. The energy of the emitted photon (11.6 eV for Argon) is sufficient to ionize the cathode material (the ionization potential is, for example, 7.7 eV for copper) and to produce a spurious avalanche, subsequent to the first one. This probability is so high, even for low gains, to induce a permanent discharge process.

This problem can be solved by adding a small amount ( $\sim 10\text{-}20\%$ ) of polyatomic molecules like Methane, Alcohol or even inorganic compounds ( $\text{CO}_2$  or  $\text{BF}_3$ , for example). These, acting as a *quencher*, absorb the radiated photons and dissipate this energy through elastic collisions or by dissociation into simpler radicals. By also suppressing the spurious avalanches they allow to attain gains up to  $10^6$  before discharge effects take place.

It is also possible to increase the detector gain by adding small quantities of electronegative gases (freon, for instance). They absorb the radiated photons and also trap the electrons extracted from cathodes, before they reach the anode plane to induce an avalanche.

Organic quenchers can give many problems after high radiation fluxes have been absorbed. In fact their recombination after dissociation can have, as a result, the formation of liquid or solid polymers, accumulating at anode and cathodes. This formation can result in a continuous discharge and a detector damage. This can be restored only after complete cleaning.

Inorganic quenchers, like carbon dioxide, avoid ageing effects but they are less efficient.

Multiwire proportional chambers usually work in open flow of gas, since it is difficult to seal large surface detectors in an efficient way. The large amount of quencher consumed in each detected event is not therefore a problem.

### 3.2.3 Readout methods

The information from a MWPC can be processed in different ways. It is possible to consider each wire as a single separated detector with its own electronics. In this case only one coordinate can be reconstructed. The second one can be obtained by using another chamber with wires perpendicular to those of the first one.

It is also possible to segment one or both cathode planes in pads (square shaped) or strips (rectangular shaped). This kind of MWPCs are called CSC/CPC (Cathode Strip/Pad Chambers). In one plane strips are parallel to wires, in the other they are perpendicular .

The avalanche, highly localized along the wire, induces a signal on the cathode planes, due to the ion motion. The wire is used to start the multiplication process.

The induced signals are large in the strip close to the avalanche point and decrease with distance. This point can be estimated by calculating the *center of gravity* of the charge induced in the sample of hit strips (this method will be described later in section 7.3).

In the next chapter technical and geometrical parameters chosen for the ALICE tracking chambers will be discussed. In particular Station 3, 4 and 5 features will be illustrated in details since their study is the subject of this thesis. The readout electronics will also be presented.



# Chapter 4

## The Muon Arm Tracking System

Multiwire proportional chambers with segmented cathode planes are well suited as tracking devices for the ALICE Muon Arm. These detectors in fact well satisfy all the requirements, particularly spatial resolution and efficiency over a large surface area at a reasonable cost.

As we have already seen in chapter 3 the tracking system is made by 10 chamber planes, grouped into 5 Stations.

Each Station has to cope with different constraints which lead to a different detector structure.

Chambers belonging to Station 1 and 2 have a small radius since they are close to the interaction point. But owing to the higher particle flux a high granularity is required.

Station 3 is located inside the magnet. It is necessary to reduce multiple scattering to avoid a deterioration of the mass resolution.

Stations 4 and 5 are located between the dipole magnet and the muon absorber. The particle density is here relatively small but their large size is technically demanding (for example wire length, cathode planes planarity and rigidity).

In this chapter we describe the tracking system paying more attention to its functional aspects and leaving a discussion of the technical features and assembly technique to chapter 6.

### 4.1 CSC's geometrical parameter

The CSCs are made by a central anode wire plane and by two cathode planes segmented into strips to have a bidimensional information on track position. In the bending plane strips are perpendicular to wires, while in the non bending they are parallel.

A schematic view of CSC's geometrical parameters (anode-cathode distance, wire

pitch, strip lengths and widths) is shown in fig. 4.1. These parameters have been chosen, for each Station, in order to satisfy specific technical and physical requirements, as already shown.

Figure 4.1: *Schematic view of the Cathode Strip Chamber geometrical parameters.*

The distance between the wire plane and the cathode plane is  $d = 2.5$  mm. Any effect coming from mechanical defects, like a non perfect planarity of cathode planes, would be amplified for lower gap values. On the other hand, once the strip dimensions have been fixed, the charge spread in the cathode planes would become smaller, leading to a decrease in the occupancy<sup>1</sup> rate. This would allow to disentangle two hits, in case of overlapping events but it would increase the number of readout channels.

A larger gap would require fewer strips but the occupancy rate would increase.

According to some authors ([Cha73], [Gat79], [Fen95]) the best resolution in the bending plane is achieved for a ratio of the strip width  $W$  to the gap  $d$  equal to  $\sim 1$ . Others find a higher ratio (1.4-1.6 [Kho94]) or even 1.5-2.0 [Chi83]. It has been demonstrated [Wur97] that a ratio  $W/d=2$  leads to only a 4 % resolution worsening with a consistent reduction in the number of readout channels. In our case a width  $W$  of 5 mm has been chosen.

To achieve a spatial resolution, in the non bending plane, close to  $700\text{-}800\text{ }\mu\text{m}$  the anode pitch  $s$  must be 2.5 mm. In fact, by taking into account an uniform particle distribution the resolution, in this plane, is  $\sigma = s/\sqrt{12}$ . A pitch value less than 2 mm would introduce critical requests on the assembly.

The strip size, in each Station, has been chosen in order to minimize the occupancy factor. A 5% value is considered an acceptable compromise between the number of readout channels and the estimated reconstruction efficiency for

---

<sup>1</sup>It is defined as the ratio between the number of fired strips and the total number of strips in a given area.

close hits [MUO].

Since the hit density decreases as a function of radius (fig. 3.1) the cathode planes have been divided into three regions, with different strip lengths (while the width stays constant) to keep the occupancy level constant along the chamber radius.

The chosen gas mixture has to satisfy the following requirements:

- low working voltage;
- good ionization efficiency;
- high gain;
- low detection efficiency for neutral particles (in particular neutrons and  $\gamma$ );
- minimization of ageing effects.

Some tests with a CSC prototype have been made [Kha99], by using different gas mixtures and quencher percentages. The mixture Argon-Isobutane shows a good ionization efficiency but it is sensitive to neutrons and is flammable. The Ar-CO<sub>2</sub> mixture shows a good ionization efficiency and it does not contain hydrogen atoms which could induce n-p reactions. By showing a reduced sensibility to neutrons, it contributes to the background reduction. As a consequence of the results obtained in these tests it has been decided to use a gas mixture made by Ar and CO<sub>2</sub>.

## 4.2 Station 1 and 2

Stations 1 and 2 have similar technical and geometrical characteristics. Since they are close to the beam interaction point the number of particles per unitary area will be high ( $\sim 5 \cdot 10^{-2}$  part/cm<sup>2</sup>). This requires the use of a high granularity readout.

Since the total surface is relatively small these chambers will be made by four quarters (fig. 4.2).

Each detector is built with a sandwich composite technology. It is made by a central anode wire plane and by two outer segmented cathode planes. The strips are arranged in groups of 64 and are connected to the readout electronics through Kapton foils.

The cathode planes are glued on a Rohacell foam to provide rigidity to the structure. This panel is milled to allow strip connections to readout electronics. In fig. 4.3 the design of a chamber quarter, for the Station 1, is shown.

The strip size and the corresponding occupancy as a function of the radius are shown in fig. 4.4 for Station 1 and in fig. 4.5 for Station 2.

Figure 4.2: *Station 1 and 2 layout.*

The original strip size, in the innermost region, for Station 1 was  $5 \times 7.5 \text{ mm}^2$  and the gap between anode plane and cathode plane 2.5 mm. These dimensions have been recently decreased to  $4 \times 6 \text{ mm}^2$  and to 2 mm respectively. Also the wire pitch has been reduced to 2 mm. These modifications allow to reduce the occupancy factor by 36% with respect to the previous size for the same particle flux and chamber gain [MUOAD].

### 4.3 Station 3, 4 and 5

To cover the geometrical acceptance of the tracking system ( $2^\circ$ - $9^\circ$ ) the last three Stations must have a circular active area with a maximum outer radius ranging from  $r = 1.544 \text{ m}$  (Station 3) up to  $r = 2.610 \text{ m}$  (Station 5).

The large size of such Stations suggested a different approach in the design of the detector structure. In fact, it would be quite demanding to have quarters, like in Stations 1 and 2, owing to the wires length and the cathode planarity over a large area.

To cope with these problems a more segmented approach has been chosen. The active area is thus covered by independent rectangular detectors (Slat) 40 cm height, as sketched in fig. 4.10. The total sensitive area is around  $20 \text{ m}^2$  per chamber.

Though the dimensions of Stations 4 and 5 are very similar, their design will not be identical. The slat number and length will be different for geometrical

Figure 4.3: *General design of a Station 1 quarter. The milled Rohacell layer and some connectors are visible.*

acceptance and cost reasons. Nevertheless the mechanical and technical approach is the same for all the last three Stations.

For what concerns Station 3 a direct extrapolation from the last two Stations project is not possible, owing to its position inside the magnet, which makes also more difficult its integration (cabling and cooling).

Such chamber will work in a magnetic field of about 0.7 T, with the field vector horizontal and perpendicular to the anode wires. This is thus perpendicular to the electric field between the anode and cathode planes. The magnetic field modifies the mean trajectory of the primary electrons in the vertical plane, by a Lorentz angle  $\alpha$ . This angle is approximately given by  $\tan\alpha = |\vec{v}_D \times \vec{B}| / \vec{E}$  and mainly depends on High Voltage and gas mixture [MUO] .

The charges are spread over a wire segment which leads to a spatial resolution degradation. In fact, due to the statistic fluctuation of primary clusters along the track, the avalanches are distributed in a random way along the wire. Thus an additional error in the center of gravity measurement should thus occur. This spreading effect is similar to that provided by a track inclined at  $\phi_y + \alpha$  with respect to the detection plane.

Figure 4.4: *Strip sizes (top) and occupancy level as a function of the radius (bottom) for both chambers 1 (full line) and 2 (dashed line) of Station 1.*

Figure 4.5: *Strip sizes (top) and occupancy level as a function of the radius (bottom) for both chambers 1 (full line) and 2 (dashed line) of Station 2.*

Figure 4.6: Definition of  $\alpha$  (a) and  $\theta$  (b) angles.

The dependence of resolution on the Lorentz angle  $\alpha$  can be expressed as [MUO]:

$$\sigma = \sqrt{\sigma_o^2 + (\sigma_\alpha \tan \alpha)^2} \quad (4.1)$$

where  $\sigma_o$  is the resolution for  $\alpha=0$  and  $\sigma_\alpha$  is the contribution due to the track projection, different from zero, on the anode.

The behaviour of spatial resolution as a function of the incident angle has been studied on a chamber prototype (chapter 9).

### 4.3.1 Slat structure

Each slat has a constant height (along the wires) and length which is function of the distance from the beam axis. Cathode planes are made by double-sided Printed Circuit Boards (PCB). One side of these circuits hosts the active strips, while the other contains the connecting lines between strips and readout electronics.

Each PCB has an overall surface of  $580 \times 400 \text{ mm}^2$  with an active area of  $400 \times 400 \text{ mm}^2$  and two regions dedicated to the electronics.

This size is a good compromise between the request to have elements as long as possible and the capability by industries to produce PCBs with stringent mechanical tolerances at an affordable price.

Because of these constraints each cathode plane will be made by a number of PCBs between 2 and 6, mounted one next to the other. In fig. 4.7 a standard slat, made by 3 PCBs is shown. The upper and lower bands, dedicated to the electronics, are visible. The hatched squares represent the active region.

The CSC modules will be mounted horizontally, with vertical wires. Each slat will work as an independent detector for what concerns gas and High Voltage supplies, mechanics and electronics. To reduce dead areas the modules will be overlapped (fig. 4.8).



Figure 4.7: *Standard slat design. The upper and lower PCB regions host the electronics, the squared ones represent the active area. On the right, a slat cross section is displayed [Ors01].*

The described structure, with limited height slats and short wires, allows to reduce the loading on the mechanical structure (fig. 4.10). The use of lightweight materials, which reduces multiple scattering effects, is therefore possible.

For what concerns slat support there are two options. The first foresees a frame, made of carbon/epoxy fibers to reduce their dimension variation due to temperature, for each half-chamber. The frames have to support the slats, the high and low voltage cables and the gas supplies. To minimize the hit losses due to the vertical part of frames the two half chambers must overlap in the middle, by a distance corresponding to the width of the vertical frame. Owing to the large size of the last two Stations the width of the vertical frame cannot be less than 38 mm and also cables will run along the central vertical direction, making this region a dead zone [MUOAD].

A new approach for the supports, based on sandwich panels, has been studied. They are made by 2 skins of 0.3 mm of carbon fiber ( $\simeq 0.3\% X_o$ ) core made with Nomex honeycomb of 15 mm. Sandwich panels are less heavy than frames (panel = 18 kg, frame = 173 kg) and very small mechanical deformations are observed whatever the composite type is. For Station 3 the lack of place in the dipole with frames is avoided using panels. The disadvantage is shown by the difficulties with tooling, due to very large dimensions (5.5 m  $\times$  2.6 m for Station 5). Investigations on frames and panels are in progress [Orsi01].

Figure 4.8: *Slat overlapping in Station 3 [Ors01].*

### 4.3.2 Strip sizes

As we have already seen there will be three strip sizes as a function of hit density. These dimensions have been chosen mainly to keep constant the occupancy level along the radius (see chapter 3). The occupancy factor as a function of the radius, for the last three Stations, is illustrated in fig. 4.9.

To simplify the design and the construction each PCB will contain a matrix of strips of only one size. This leads to six different PCB types (three for the bending plane and three for the non bending).

For the bending plane a 5 mm strip height has been chosen. This solution has been tested [Kha99] and showed the possibility to achieve the required resolution ( $< 100 \mu\text{m}$ ). The strip width is 25 mm, 50 mm and 100 mm for the three regions. For the non bending plane the strip width will be 7.143 mm. This corresponds to nearly 3 wires per strip, a value which makes easier the hit wire identification. With this size exactly 56 strips are present in each row of the non bending plane.

In table 4.1 and 4.2 the strip segmentation for, respectively, bending and non bending plane, is given.

PCB type	$\Delta x \text{ (mm)} \times \Delta y \text{ (mm)}$	Number of channels
1 (High density)	$25 \times 5$	1280
2 (Medium density)	$50 \times 5$	640
3 (Low density)	$100 \times 5$	320

Table 4.1: *Strip segmentation and number of channels in the bending plane (y direction).*

PCB type	$\Delta x \text{ (mm)} \times \Delta y \text{ (mm)}$	Number of channels
1 (High density)	$7.143 \times 25$	896
2 (Medium density)	$7.143 \times 50$	448
3 (Low density)	$7.143 \times 100$	224

Table 4.2: *Strip segmentation and number of channels in the non bending plane (x direction).*

The different PCB types in each cathode plane have been located by taking into account the maximum tolerated occupancy factor. Each PCB type in the bending plane is in front of the same PCB type in the non bending plane. In fig. 4.10 the different geometry distribution for Station 3, 4 and 5 are shown.

Figure 4.9: Occupancy level as a function of the radius for both chambers 1 (full line) and 2 (dashed line) of the last three Stations.

Figure 4.10: *Schematic view of a chamber of Station 3, 4, and 5 respectively with the different strip densities.*

### 4.3.3 Special slats

Based on AliRoot simulations the shape of the slats has been optimized. Dimuons coming from  $\Upsilon$  decay have been generated and a sample of “golden tracks” which survive to the coincidence of Station 1, 2 and trigger chambers has been selected. The impact points of these tracks on Station 3, 4 and 5 have been reconstructed [Bal01].

It comes out that, to reduce hit losses in the central part of the chambers, round shaped slats, as shown in fig. 4.12 and 4.13, are needed around the beam pipe. Besides this, in Station 3, a central “half moon” slat (fig. 4.11) will avoid a 1.9% event loss [Bal01]. Due to its position inside the magnet the length of this slat for chamber 6 will be greater than the same slat of chamber 5.

A central half moon slat is not needed for Stations 4 and 5. In fact this would reduce the losses of only 0.15%. Circular PCBs need a dedicated study, since the design is much more complicated.

Figure 4.11: *Half moon slat needed for the Station 3 (chamber 5) [Ors01].*

A first round shaped prototype, 1.6 m long, is now being assembled at SU-BATECH Nantes and it will be tested at CERN during summer 2002.

### 4.3.4 Ghost hits

Ghost hits are generated when more tracks hit the same rectangular area  $L_x \times L_y$ , where  $L$  is the strip length. For example, as shown in fig. 4.14, if we have two tracks four coordinate combinations are possible and we have to disentangle the right from the fake ones.

Figure 4.12: *Round shaped slat for Station 3 (chamber 5) [Ors01].*

Figure 4.13: *Round shaped slats for Stations 4 and 5 [Ors01].*

Figure 4.14: *Ghost hits originated by two true hits.*

The correlation between the charge in the bending and non bending plane (fig. 4.15) will be used to reject these hits. If the avalanche was symmetric around the wire the charge induced by ions drifting towards the cathode planes should be the same. Due to fluctuations in the primary ionization there can be an asymmetry which is amplified when the ion clouds approach the cathode planes.

Since the integration time of the preamplifier is large ( $\sim 500$  ns) this effect is noticeable and the ratio  $Q_x/Q_y$  shows a non negligible dispersion (fig. 4.16).

To reject ghost hits all the reconstructed charges  $\{Q_x\}$  and  $\{Q_y\}$  will be sorted in ascending order and the pairs will be chosen from this ordering [MUO].

With a typical value of the dispersion around 11% a misidentification probability of 5% has been obtained, for the most probable case of two hits in the same area. The ghost hits problem is mainly shown in the large strip regions.

If we consider that in the  $10 \times 10$  cm<sup>2</sup> strip region the probability to have a muon hit coming from a  $\Upsilon$  together with a background hit is around 20%, we obtain a 1% of misidentified good events [MUOAD].

Slat module characteristics will be described in more details in the following chapters.

## 4.4 Readout electronics

The high number of electronic channels, around one million, associated to the large chamber dimensions, requires a modular design for the readout electronics. The charge produced by a particle crossing the detector is small ( $\sim 10$ -100 fC) and must be amplified. The transmission of low level analog signals is therefore



Figure 4.15: *Correlation between charges induced in bending and non bending plane.*

Figure 4.16: *Ratio of the charges induced in bending and non bending plane.*

forbidden and the use of amplifiers is required.

Besides this the length of the connecting lines, which drive the signal from the strips to the readout electronics, must be as short as possible to reduce electromagnetic pick-up on the lines. The spatial resolution in fact mainly depends on the signal to electronic noise ratio. The signal will be therefore preamplified close to the strips. The readout electronics will be located as close as possible to the strips to avoid a large number of lines on the PCBs and the coding, the pedestal subtraction and the zero suppression will be made on board.

The readout card must be as thin as possible to limit multiple scattering effects. Moreover, electronics power consumption must be low due to the great channel number. Last but not least the readout system has to show a low noise level, a high reliability, a limited unitary cost and an easy production, plug in and repair.

#### 4.4.1 GASSIPLEX

The C-Mos VLSI 16 channel GASSIPLEX chip, developed at CERN( [Bek97], [San99]) is well suited to gaseous detectors. A new version of GASSIPLEX chip, called MANAS-16, is currently being designed for the ALICE tracking chambers by the Calcutta Saha Institute of Nuclear Physics.

GASSIPLEX shows a low level noise, a good sensitivity and long integration times. It is made by a charge preamplifier (CP), a switchable filter (FLT), a shaping amplifier (SP), a Track/Hold stage to store the charge in a capacitor by opening a switch and an analog multiplexer to multiplex the stored charges on a single output line (see fig. 4.17).

GASSIPLEX is an ungated, and then asynchronous, device. This means that each output, or baseline, has to be kept at a constant level when there is no physical signal in the input line. This level is called *pedestal* and can be measured in mV or ADC channels. Its mean value can be set close to zero by means of a potentiometer in order to take advantage of the largest chip dynamic range.

The low noise amplifier is characterized by a long integrating time ( $\sim 600 - 800 \text{ ns}^2$ ). This feature, together with a high input sensitivity, allows to detect very low signals.

The slow drift of ions towards the cathode planes gives rise to a hyperbolic long tailed current which lasts a few microseconds and disturbs the baseline when the shaping is done in the next step. The filter has been designed to provide a stable baseline level restauration at  $\pm 1 \%$  of the peak amplitude, after less than  $3 \mu\text{s}$ . It extracts the biggest part of the output signal, from the amplifier, and transforms it in a quasi-step function as input to the shaper. When the rate is high this reduces the signal duration and avoids event overlapping.

---

<sup>2</sup>These values and the followings refer to GASSIPLEX  $1.5 \mu\text{m}$ .

Figure 4.17: *GASSIPLEX functional blocks.*

The shaper amplifier is made by a low-pass filter and a band-pass filter. This combination transforms the quasi-step function into a semi-Gaussian shape. The peaking time is adjusted at  $(600 \pm 100)$  ns by means of an external bias resistor. This shaping improves the signal to noise ratio and allows an easier peak voltage measurement since the semi-Gaussian shape has a flat top [MUO].

When a particle hits the chamber a charge is induced in the cathode planes. This signal is driven by connecting lines in the PCB backplane towards the read-out electronics. The capacitors, associated to the hit channels, are charged up and the total charge corresponds to the current induced in the detector. An external trigger signal, synchronous with the physical event, generates a HOLD signal. This is sent to the system to open all switches at a time corresponding to the shaping amplifier peaking time (fig. 4.18).

Figure 4.18: *Timing of the GASSIPLEX signals.*

The maximum signal is stored for hit strips and the pedestal values are stored for those being no hit.

When the HOLD signal is ON the switches are opened and the charge signals

are frozen in the capacitors. When the HOLD signal is released the switches are closed and the charges are lost. The event read out is independent from the T/H signal.

#### 4.4.2 MANAS-16

GASSIPLEX chips will be substituted by a different chip, MANAS-16 (16 channel Multiplexed ANalog Signal-Processor). Its gain and dynamical range have been designed in order to satisfy the dimuon spectrometer requirements.

It is composed by a charge sensitive amplifier (CSA), a deconvolution filter (DF), a semi-Gaussian shaper (SGS), a Track&Hold stage and an analog multiplexer [MUO]. In fig. 4.19 a schematic representation of a MANAS-16 channel is shown.

Figure 4.19: *Representation of a single MANAS-16 channel.*

The architecture of the chip is identical to GASSIPLEX, so its working mode will not be described again, but the dynamic range and the peaking time have been increased. The first indian MANAS version showed performances similar to those of GASSIPLEX. A second iteration should correct some problems in the T/H stage and reduce the chip size [MUOAD].

A comparison between MANAS and GASSIPLEX 0.7  $\mu\text{m}$  features is presented in table 4.3.

#### 4.4.3 The test electronics

During the in-beam tests performed on slat chamber prototypes a provisional readout electronics has been used. In this case a START/READ signal, generated by the event trigger logic with a desired delay, starts a train of multiplexed clock pulses, provided by an external device, allowing the read out process to begin. With this module (CAEN Sequencer V551B [V551B]) it is possible to decide the frequency and the number of the clock pulses, i.e. the number of channels to be read out. Once these values are known the duration of the HOLD signal must be set larger than the CLOCK signal duration.

	MANAS	GASSIPLEX 0.7 $\mu\text{m}$
Technology	SCL 1.2 $\mu\text{m}$	Alcatel-Mietec 0.7 $\mu\text{m}$
Peaking time	1.2 $\mu\text{s}$	1.2 $\mu\text{s}$
Dynamic range (+)	500 fC	560 fC (0 to 2 V)
Dynamic range (-)	275 fC	500 fC (0 to -1.1 V)
Conversion gain (+)	3.5 mV/fC	3.6 mV/fC
Noise at 0 pF	640 $\text{e}^-$ rms	530 $\text{e}^-$ rms
Noise slope	11.58 $\text{e}^-$ rms/pF	11.2 $\text{e}^-$ rms/pF
Analog readout speed	10 MHz (max)	10 MHz (50 pF load)
Power consumption	7 mW/ch	8 mW/ch at 10 MHz
Output temp. coefficient	0.03 mV/ $^{\circ}\text{C}$	0.05 mV/ $^{\circ}\text{C}$

Table 4.3: MANAS-16 and GASSIPLEX 0.7  $\mu\text{m}$  main features.

The output signal, made by multiplexed sequential charges, is sent to another device, a 12 bit V550 C-RAMS (CAEN Readout Analog Multiplexed System [V550A]) which performs the analog to digital conversion. Each ADC channel will give as output a logic signal corresponding to the charge induced in each detector strip.

After the digitization process and after the HOLD signal has been released, a RESET signal is sent to the GASSIPLEX and the switches are in the initial position (switches driven by the T/H stage are closed and those driven by the MPX stage open). A BUSY signal avoids the overlapping of events during the whole process, by vetoing the trigger logic. This signal is then released when all the operations are completed [Bek97].

It is possible to connect several 16 channel chips in a daisy chained way, up to a maximum channel number of 2048. A long multiplexed preamplifier chain is not desirable since the sequential read out time increases. Moreover the read out process occurs through a single line and the breakdown of a single channel could cause the loss of the whole information transiting over the chain.

Four GASSIPLEX chained in a single board allow to read out 64 channels. This configuration, called GAS64, has been extensively tested and used for ALICE tracking chambers prototypes [Cou99]. In fig. 4.20 a GAS64 card is shown with its scheme.

ALICE tracking chamber prototypes have been equipped, until year 2000, with GASSIPLEX chips built in 1.5  $\mu\text{m}$  technology. During the June 2001 test the new 0.7  $\mu\text{m}$  version [San99] has been used. Their features are compared in table 4.4.

The main difference between them concerns the insufficient dynamic range

Figure 4.20: *Top side view of GAS64. The four GASSIPLEX chips are shown.*

	GASSIPLEX 1.5 $\mu\text{m}$	GASSIPLEX 0.7 $\mu\text{m}$
Technology	Alcatel-Mietec 1.5 $\mu\text{m}$	Alcatel-Mietec 0.7 $\mu\text{m}$
Peaking time	from 450 to 650 ns	1.2 $\mu\text{s}$
Dynamic range (+)	150 fC	560 fC (0 to 2 V)
Dynamic range (-)	-75 fC	500 fC (0 to -1.1 V)
Conversion gain	12.5 mV/fC	3.6 mV/fC
Noise at 0 pF	650 e <sup>-</sup> rms	530 e <sup>-</sup> rms
Noise slope	15 e <sup>-</sup> rms/pF	11.2 e <sup>-</sup> rms/pF
Analog readout speed	10 MHz	10 MHz (50 pF load)
Power consumption	8 mW/ch	8 mW/ch at 10 MHz
Output temp. coefficient	0.1 mV/°C	0.05 mV/°C

Table 4.4: Comparison of GASSIPLEX 0.7  $\mu\text{m}$  and 1.5  $\mu\text{m}$  characteristics.

showed by the first chip version. In fact it has been built and optimized for ALICE RICH detector (Ring Imaging Cherenkov), which shows different constraints.

#### 4.4.4 The final readout system: MANU

GASSIPLEX+Sequencer+C-RAMS readout system has been used up to now for prototype test. In the final detectors it will be substituted by a single readout card called MANU (MANas NUmerical). It will process the analog signal, convert this in a digital one, subtract the pedestals and transmit the zero-suppressed data. It is made by:

- four GASSIPLEX (or MANAS-16) preamplifier/shaper/multiplexer;
- two 12 bit ADCs, with a conversion range of 0 to +3 V, to optimize the power consumption for the same coding time (500 ns conversion time);
- a digital processor called MARC (Muon Arm Readout Chip).

The four MANAS-16 chips are not controlled through daisy chaining. This allows to disable, via software, a single unit in case of bad working.

The MARC processor sequences the GASSIPLEX read-out, the coding, it performs the pedestal subtractions, the zero suppression and transmits the data on the numerical buses towards the front-end DSPs (Digital Signal Processor).

The MANU cards, also called *slave stations*, performs the following operations [MUOAD]:

- amplification and filtering of 64 channel analog signals;



- 12 bit coding;
- selection of the hit channels after zero suppression (this is obtained by a comparison with a threshold value);
- buffering of the data and interface with the readout bus.

In fig. 4.21 the architecture of the card is shown.

Since the Stations have different requirements two MANU versions have been developed. MANU12 (for Stations 1 and 2) must have a small size owing to the strip dimensions in the first two Stations and has to be connected with them through Kapton foils. Its dimension are  $23 \times 63 \text{ mm}^2$  and has four connectors: for low voltages, for command signal distribution, for the digitized data and for the Kapton foil. MANU345 (for Stations 3, 4 and 5) has less constraints for what concerns dimensions ( $32 \times 50 \text{ mm}^2$ ) and it is directly plugged in the cathode planes, requiring only one 100 pins connector.

The MANUs will be connected to DSP clusters, located on a board called CROCUS (Cluster Read Out Concentrator Unit System), through PATCH (Protocol for Alice Tracking Chambers) data buses. Each of them is made by two parts. A bus in LVTTTL (Low-Voltage TTL) technology is located on the chamber PCBs. A maximum number of 24 MANUs can be connected, to limit the signal attenuation due to parasitic capacitance of each slave. This bus is only one meter long and is connected to CROCUS boards via a LVDS (Low Voltage Differential Signaling) bus, which can be several metres long (fig. 4.22).

These buses drive N slave Stations to one link port of the DSP, which is the master station bus controller. In one direction they download parameters towards MANU (thresholds and trigger signals) and in the other they allow the readout of the data.

Each CROCUS is made by 8 DSPs associated with a concentrator. This at first will collect the data from DSPs and later will send them to the DDLs (Detector Data Link). The read out time needed for an average size event is:

- $t=0$ , the particle crosses the chamber, L0 trigger signal;
- $t=38 \mu\text{s}$ , coding and zero suppression are performed in the MANU boards;
- $t=68 \mu\text{s}$ , the data are stored in the DSPs;
- $t=88 \mu\text{s}$ , the data are transferred to the concentrator DSPs;
- $t=240 \mu\text{s}$ , the data transfer to the DDLs is completed if one DDL/CROCUS board is used. If two DDLs are associated to each CROCUS this time is reduced to  $164 \mu\text{s}$ .

Figure 4.21: *Schematical view of MANU architecture (top) and top side view of MANU345 (bottom).*

Figure 4.22: *Bus LVTTTL and LVDS connection between PCBs.*



## Chapter 5

# Slat chamber optimization

A slat chamber is made by a sandwich structure. In the middle plane wires are soldered or glued in a frame which has to ensure a constant distance between anode plane and each cathode plane. The two outer cathode planes are glued on panels to achieve the required rigidity and planarity. A high permittivity insulating foil will be inserted between the panel and the cathode plane, to reduce capacitive noise. The various elements (fig. 5.1) will be assembled at different times and later coupled and sealed together to form the whole detector.

Figure 5.1: *Exploded view of a CSC: from center to top (or bottom) the anode wire frame, the PCB planes and the carbon fiber panels are shown.*

Most of the geometrical parameters have already been fixed, as explained in the previous chapter. Some other characteristics have to be optimized through simulations and prototype tests.

In this chapter we present a study, based on simulations, to estimate the variation on some detector performances with geometrical parameters and the electric field behaviour at the chamber edges. This study can be very useful to establish the allowed geometrical tolerances for different chamber elements and put in evidence the high mechanical precision and technical level to be adopted during the slat chamber assembly to achieve a spatial resolution better than 100  $\mu\text{m}$ .

## 5.1 Gain dependence on mechanical tolerances

It is well known that gain, in multiwire proportional chambers, depends in a critical way on geometrical parameters (see ref. [Sau77] for a detailed discussion). It could therefore change from point to point as a function of mechanical variations.

The analytical expression for electric field near wires is [Dia91]:

$$E = \frac{s}{\pi r_o} \times \frac{V_o}{g - \frac{s}{\pi} \ln\left(\frac{2\pi r_o}{s}\right)} \quad (5.1)$$

where:

$r_o$  = wire radius

$g$  = gap

$s$  = wire pitch

$V_o$  = High Voltage.

This means that even a small variation of one of the geometrical parameters results in a large gain variation, through a change in the first Townsend coefficient. This, in fact, depends in a strong way on the electric field (see section 3.1.4). Thus it is very important to keep these parameters as constant as possible to avoid large gain variations which would influence the spatial resolution and reconstruction efficiency. Experimentally it has been demonstrated that a relative gain variation  $\Delta G/G$  of 15% is an acceptable value.

As a first step we calculated, using Garfield [Gar] program, the gain<sup>1</sup> for a CSC in a *standard* working configuration, i.e. a gas mixture of 80% Ar and 20% CO<sub>2</sub>, 2  $r_o$  = 20  $\mu\text{m}$ ,  $g$  = 5 mm,  $s$  = 2.5 mm and  $V_o$  = 1650 V. The value we found has been used as a reference to compare gain variations.

---

<sup>1</sup>With gain we mean the number of electrons produced by a primary electron during the multiplication process. See section 5.2 for the gain evaluation procedure.

To have an idea we plot, in fig. 5.2, the gain behaviour between 1000 and 2000 Volt.

Figure 5.2: *Gain variation as a function of High Voltage.*

### 5.1.1 Anode wires

As shown by eq. 5.1 the gain increases as the wire diameter decreases. On the other side, to compensate the electrostatic force to which they are subjected, a mechanical tension has to be applied. It has to be as high as possible to avoid gap variations due to vibrations.

Tungsten wires are widely used in wire chambers since they show a good resistance to mechanical stretching, even at small diameters.

In our tracking chambers a diameter of 20  $\mu\text{m}$  has been chosen<sup>2</sup>, as a compro-

---

<sup>2</sup>For all the prototypes assembled up to now wires have been supplied by LUMA METALL [Luma].

mise between gain and mechanical stretch. For these wires the maximum value of the mechanical tension to avoid elasticity loss is 70 g. Thus a tension between 50 g and 60 g is suitable for our use.

An important aspect is how to fix anode wires to the spacers. To this aim two techniques have been explored.

- **Soldering on a PCB frame.** This method guarantees a good electrical conductivity between wires but increases the amount of matter and requires a lot of time. Moreover wires could be damaged by  $\text{ZnCl}_2$  acid dropping during the heating process. Since the tungsten melting point is  $3410^\circ \text{C}$  wires need to be plated with gold. The gold coating prevents wire corruption but, to avoid gain variations, the material deposition must be as uniform as possible. The gold plated surface could also induce current micro-leakages. An enlarged view of a  $20 \mu\text{m}$  gold plated wire is shown in fig. 5.3.
- **Gluing.** Wires could be glued to spacers with a conductive resin adding later a conductive ink. This assembly procedure is faster and allows to use uncoated wires. With this technique spacers must be grooved to allow wire positioning.

It is important to check what is the diameter tolerance for the two different kind of wires.

In May 2001 we made an enquiry to Luma about *gold plated* and *cleaned and straightened* wires, with or without the addition of Rhenium<sup>3</sup>. At the same time a simulation of the gain behaviour as a function of wire diameter variation has been performed.

Both kind of wires can achieve a required 2 % maximum ovality (out of roundness) and straightness grade 1 (these features are not standard but they are available on request with a price addition). The results of our investigation are reported in table 5.1.

From simulations (fig. 5.4) we can see that the standard diameter tolerance for gold plated wires leads to a  $\pm 6 \%$  maximum gain variation. It is possible to reduce the gain variation to  $\pm 5 \%$  and  $\pm 3 \%$  with a, respectively,  $\pm 1.5 \%$  and  $\pm 1 \%$  diameter tolerance, available on request. This improvement involves however a 10 % and a 30 % price addition.

For cleaned and straightened wires the situation is different. The standard diameter tolerance is  $\pm 1 \%$ . This value can give rise to a  $\pm 3 \%$  gain variation (see fig. 5.4).

On request, the diameter tolerance can be  $\pm 0.75 \%$ , which leads to a  $\simeq \pm 2 \%$  gain variation and a 5 % price addition. The best achievable value is  $\pm 0.5 \%$  to

---

<sup>3</sup>With a percentage of Rhenium the wire shows superior hot and vibration strength.



Figure 5.3: *Enlarged view of a 20  $\mu\text{m}$  gold plated wire. The pictures (4500 enlargments on top, 1500 on bottom) show a good uniformity in gold coating.*

Kind of wire	Quality (Luma code)	Price (Euro/km)	Standard Diameter Tolerance
Gold plated W	821/60	155	$\pm 2\%$
Gold plated W + 3% Re	861/60	310	$\pm 2\%$
Cleaned and Straightened W	821/42	35	$\pm 1\%$
Cleaned and Straightened W + 3% Re	861/42	105	$\pm 1\%$

Table 5.1: *Luma quotation for gold plated and cleaned and straightened wires (May 2001). For all quotations VAT is included.*

Figure 5.4: *Gain variation as a function of wire diameter variation.*

obtain a  $\simeq \pm 1$  % gain variation but with a 10 % price addition. Tungsten + 3 % Re no gold plated wires ensure therefore a better diameter tolerance, at a lower price. This kind of wires can be only glued; for this reason this assembly procedure is preferable to soldering.

### 5.1.2 Cathode planes planarity

It is very important to ensure cathode planes planarity to reduce, as much as possible, any gain variation.

We can see from simulations (fig. 5.5) that an overall gap variation equal to 2% (i.e. an absolute variation of gap of 100  $\mu\text{m}$ ) leads to a  $\simeq 12\%$  gain variation.

Figure 5.5: *Gain variation as a function of gap variation.*

To increase the cathode planes rigidity the PCBs have to be glued on panels made by 0.2 mm thick skins of high modulus carbon fiber and a 6 mm thick

Nomex honeycomb core. Assuming a 0.5 mbar differential pressure the deflection is  $4\text{ }\mu\text{m}$ , which leads to a negligible gain variation.

### 5.1.3 HV system

Another source of gain variation lies in the anode voltage stability. Up to now the HV system to be finally used in the Muon Tracking has not been chosen. A possible device is based on the CAEN SY1527 system [SY1527], which could ensure an accuracy of 0.3 % on the HV value  $\pm 0.4\text{ V}$ . This value leads to a  $\pm 4\text{ }\%$  gain variation as shown by the simulations in fig. 5.6.

Figure 5.6: *Gain variation as a function of HV variation.*

## 5.2 Edge wires

The electric field, near the border region, is higher than in the middle of the chamber because the last few anode wires are less surrounded by neighbouring ones. A gain increase is therefore foreseen in this region. In order to avoid sparks near the border, due to the high gain, we have to decrease it by replacing the last few anode wires with thicker wires (edge wires in the following).

We studied how many edge wires need to be placed in the border region and which is their optimum diameter to lower the gain. To choose the best configuration we must take into account the following requirements:

- We cannot increase edge wire diameter as we want since we would have to apply a higher mechanical tension and this would lead to a larger loading on spacers.
- To ensure a better electric isolation of the border we would have also to increase the number of edge wires.
- At the same time we want the smallest possible dead zone, to reduce the losses of good events in this region.
- A constant gain in the active region close to the border is also desired.
- Besides, to simplify the chamber assembly, it could be better to handle edge wires with the same diameter.

We simulated the gain behaviour at the border, for different edge wires configurations, with Garfield program.

We represented the chamber in a simplified model as made by two conductive grounded planes, placed at  $y = \pm 2.5$  mm. The anode plane is made by 20  $\mu\text{m}$  W wires, at a mechanical tension of 50 g and High Voltage of 1650 V. The gas mixture used is Ar(80 %) - CO<sub>2</sub>(20 %).

We took 20 points equally distributed around each wire, at 300  $\mu\text{m}$  from wire's centre, a distance where the multiplication process begins. From these points electrons start drifting and are accelerated towards the wire. The gas molecules are ionized by electrons and the avalanche process starts. We calculated the mean gain near each wire and we repeated these calculations for several diameters and number of edge wires.

We considered at first the configuration with only 20  $\mu\text{m}$  wires, namely without edge wires. In fig. 5.7 results are shown. For simplicity in the x axis only the first 7 wires are shown. In the y axis the corresponding gain value is reported. The situation previously described (high gain near the border) is reproduced.

Figure 5.7: *Gain value near the border (only the first seven  $20\ \mu\text{m}$  wires are shown). In the x axis the wire number is displayed. Wire zero is the closest to the end of the chamber.*

We tried to decrease this value by using one edge wire only, with different diameters. In fig. 5.8 results obtained with a  $50\text{ }\mu\text{m}$  diameter wire are displayed, showing a gain decrease near the border.

Figure 5.8: *Gain value near the border (one  $50\text{ }\mu\text{m}$  edge wire).*

To improve this isolation we studied the configuration with two edge wires, for different diameter values. With two  $70\text{ }\mu\text{m}$  edge wires, the behaviour shown in fig. 5.9 is obtained. In this situation the gain near the border is lower so this region is now better isolated. At the same time we can see that thicker wires influence the gain near the first  $20\text{ }\mu\text{m}$  wires, causing its decrease in the detector active region.

To find a good compromise between a low gain value at the border and a constant gain near the field wires we calculated the gain near the first five  $20\text{ }\mu\text{m}$  field wires as a function of edge wire diameter, for different configurations. Edge wire diameter goes from a minimum value of  $20\text{ }\mu\text{m}$  to a maximum of  $100\text{ }\mu\text{m}$ .

If the edge wire diameter is  $20\text{ }\mu\text{m}$  (i.e. we have only field wires) we can see

Figure 5.9: *Gain value near the border (two 70  $\mu\text{m}$  edge wires).*



(fig. 5.10) that the gain in the region near the border is very high (as already shown).

Figure 5.10: *Gain behaviour as a function of edge wire diameter, using only one edge wire.*

If we increase edge wire diameter the gain in this region decreases. For a diameter value of  $\sim 43 \mu\text{m}$  the gain near the field wires is approximately the same. As the edge wire diameter increases the gain near the border and also close to the first field wires decreases.

If we now take into account 2 edge wires we can see (fig. 5.11) that the gain is lower than in the previous situation, so the border is better isolated. The isolation is better and better with the increase of edge wire diameter.

With 3 edge wires the isolation increases, but the dead region is now larger (7.5 mm). This could be an acceptable choice for the outer slat chamber, but not for those surrounding the beam pipe.

These simulations seem to suggest a configuration with two edge wires between

Figure 5.11: *Gain behaviour as a function of 2 edge wires diameter.*

50 and 70  $\mu\text{m}$ , as a good compromise between good electric isolation, small dead region and a not too high mechanical tension.

Figure 5.12: *Gain behaviour as a function of 3 edge wires diameter.*

### 5.3 Electric field near the spacer

As already explained CSCs are characterized by a sandwich structure. The constant gap (2.5 mm) between anode and cathode is kept by two spacers running around the outside border of the cathode planes. They will be made of Noryl [GEP] in the final detector version.

A cross section of a slat chamber is shown in fig. 5.13, with each layer in evidence.

As we can see in fig. 5.13 (at left) a step is foreseen to avoid discharge between strip planes and wires. This shape could however introduce an electric field deformation. We simulated the electric field behaviour near CSC border to check

Figure 5.13: *Slat chamber cross section (near the border).*

this situation and to evaluate the extension of the deformed region. This study gives important information useful to choice the overlap between adjacent slats.

For comparison we investigated the configurations with and without this step (*step* and *no step* model in the following). For these simulations we evaluated the electric field with Maxwell program [Max], based on finite element analysis.

Electric field computation is a difficult task. To simplify this procedure we divided our chamber in simplified elementary cells. To each element of this object the proper material attributes and relative dielectric constant are assigned. We then calculated the field in this restricted region. The cell is then repeated and mirrored through x, y and z axis to represent the whole chamber structure.

In fig. 5.14 and 5.15 this simple structure, for the two models, is shown (the two spacer shapes are better shown in fig. 5.18 and 5.19).

After the calculation of the electric field the field maps (generated by Maxwell) can be read as input by Garfield.

The spacer cross section, together with the field wire and the potential lines, are shown in fig. 5.16 as reproduced by Garfield. As we can see there is a small deformation in the potential shape (*step model*). This deformation does not extend more than few mm. To be safe an overlap of 15 mm between slats is foreseen. In the *no step model* (fig. 5.17) the potential shape seems to be more regular.

With Garfield we can also track a particle and follow its path. Taking, for

Figure 5.14: *Step model cell.*

Figure 5.15: *No step model cell. The spacer is, in this model, a simple parallelepiped.*

Figure 5.16: *Potential profile (step model), as obtained with Garfield. The numbers in the field lines refer to the potential value.*

Figure 5.17: *Potential profile (no step model). The numbers in the field lines refer to the potential value.*



example, positive ions in the *step model* (fig. 5.18) we can see that they go towards the edge of the spacer. An accumulation of charge in this region is possible and it could cause a discharge. It could be better to round the corner to avoid this possibility. This effect is not seen in the *no step model* (fig. 5.19).

Figure 5.18: *Ion path from a particle crossing the chamber (step model).*

## 5.4 Conclusions

In this chapter results from slat chamber simulations have been presented. Such study made possible to investigate about detector performances near the edges (lateral and upper) and on some mechanical tolerances we have to respect to avoid gain variations. Hereafter we summarize the main results:

- The study on gain variations as a function of several geometrical parameters gave us useful indications about mechanical tolerances of each detector

Figure 5.19: *Ion path from a particle crossing the chamber (no step model).*

element.

- Two or three edge wires, with a diameter  $\geq 50 \mu\text{m}$ , should be used to lower the gain near the border.
- The spacer on which wires are set should be rounded to avoid a charge accumulation which could cause a discharge.

Several prototypes have been assembled by different groups to check if the geometrical and technical choices make possible to satisfy the physics requirements.

In each laboratory (Cagliari, Saclay, Nantes) many tests have been made to validate some mechanical aspects, like the structure and sealing of the chamber, the machining and gluing of the PCBs and the assembly of the whole detector parts.

Some of these detectors, showing different configurations, have been in-beam tested at CERN PS to study the main characteristics of the detector (noise, gain, resolution, efficiency).

In the following chapters the mechanical and technical aspects and the assembly procedure of three CSC prototypes will be discussed. Each of them has been equipped with a different version of the readout electronics. The first, equipped with GASSIPLEX  $1.5 \mu\text{m}$  and separated 10 bits ADC CRAMS, has been in-beam tested in May 2000. The second, with GASSIPLEX  $0.7 \mu\text{m}$  and separated 12 bits ADC CRAMS, has been studied during July 2001. The third, in-beam tested in October 2001, has been equipped with an electronic similar to the final one, with GASSIPLEX  $0.7 \mu\text{m}^4$  with on board 12 bits ADC.

Particular attention will be paid in the analysis of the data acquired during the tests and in the discussion of the achieved results, both for what concerns technical aspects and from the physics point of view.

In the next chapter the building of the first prototype completely assembled in Cagliari laboratories during year 2000 will be presented.

---

<sup>4</sup>In the final version of electronic MANAS will be used instead of GASSIPLEX  $0.7 \mu\text{m}$ .



# Chapter 6

## Study of a large CSC prototype

During year 2000 a slat chamber prototype has been built to check the capability of respecting the required mechanical tolerances during its assembly and to tune the assembly procedure for CSCs made by more than 2 PCBs per plane.

From the physics point of view the main aim was the study of the spatial resolution behaviour for  $5 \times 25 \text{ mm}^2$  strip size and the correlation between the charge induced on the two cathode planes. Other important detector features to be investigated were the noise, the gain and the efficiency.

This detector, made by 3 PCBs in each plane, for a total  $1200 \times 400 \text{ mm}^2$  active area, was the first, for the ALICE experiment, made by more than two PCBs per plane.

It has been assembled in Cagliari in collaboration between CEA Saclay and INFN Cagliari and it has been in-beam tested, in May 2000, at CERN PS.

### 6.1 Prototype characteristics

The typical slat module structure has been described in the previous chapters. In the following the main features of each detector element, adopted for this prototype, will be described in details. A particular attention will be given to the geometrical and technical features needed to achieve the required performances.

#### 6.1.1 Cathode planes

Each cathode plane is made by 3 double sided PCBs. As already explained in section 4.3.1, the total area of each Printed Circuit is  $400 \times 600 \text{ mm}^2$ .

The frontplane can be ideally divided into three regions. The central part, namely the active area, segmented into strips, is  $400 \times 400 \text{ mm}^2$ . The surface of

each upper and lower zone is  $10 \times 40 \text{ cm}^2$ . They are both dedicated to host the read-out electronics.

In the backplane connecting lines drive the signal from each strip to the corresponding pin of the connectors soldered on the PCBs on which GAS64 will be mounted. The lines ( $180 \text{ }\mu\text{m}$  wide) are connected to strips by means of metallized holes, named vias (see fig. 6.1).

The thickness of the PCB dielectric (FR4) is  $200 \text{ }\mu\text{m}$ . The metal layer has been chosen as thin as possible, compatibly with production capabilities, to reduce multiple scattering effects. The base layer is  $5 \text{ }\mu\text{m}$  thick with a final value, after recharge, of around  $20 \text{ }\mu\text{m}$ .

In the two cathode planes the strips are oriented in a different way with respect to the wires. In the bending plane the long strip side is perpendicular to the wires (Y plane), in the non bending it is parallel (X plane).

The bending plane strip dimension ( $5 \times 25 \text{ mm}^2$ ) is the same for the 3 PCB planes. This value corresponds to the highest particle hit density region in the slat tracking chambers (Station 3, 4 and 5). It was particularly interesting, in this prototype, to show the capability to execute the design, especially for what concerns the routing corresponding to the highest strip density.

One of the most important aims of the test was to evaluate the spatial resolution for  $5 \times 25 \text{ mm}^2$  strips and therefore to validate the choice of the strip segmentation.

In the non bending plane two PCBs have strips with the the same area, i.e.  $7.143 \times 25 \text{ mm}^2$ . The third PCB is subdivided in two regions with different strip dimension:  $5 \times 25 \text{ mm}^2$  and  $10 \times 25 \text{ mm}^2$ .

In fig. 6.2 the non bending plane design is shown. The strips with different dimensions and the connecting lines between strips and readout electronics are shown. A bending plane detail has already been shown in fig. 6.1.

Between strips there is a dead region. In the y direction this space is, both for bending and non bending plane,  $250 \text{ }\mu\text{m}$  to allow manufacturing in a low PCB class.

In the x direction the situation is different. To achieve the required spatial resolution the position of each strip has to be exactly known. This implies a great accuracy in the positioning of each PCB. We have to take into account a minimum clearance of  $100 \text{ }\mu\text{m}$  between adjacent PCBs for gluing and a tolerance in PCB etching of  $100 \text{ }\mu\text{m}$  over  $400 \text{ mm}$ . The calculation leads to a value of  $500 \text{ }\mu\text{m}$  between strips to have a periodic structure within the slat [Dia01].

A particular attention must be also paid to the dimensional stability in X direction. By means of a measuring machine (which guarantees a measuring accuracy better than  $7 \text{ }\mu\text{m}$  over  $1 \text{ m}$ ), equipped with a CCD camera, the distance between PCB borders has been measured. The difference between this value and the nominal one ( $399.5 \text{ mm}$ ) did not exceed  $200 \text{ }\mu\text{m}$ .

Figure 6.1: *Enlarged view of a PCB quarter. The connecting lines are clearly shown. The upper region is dedicated to the readout electronics.*

Figure 6.2: *PCB non bending plane design. The two strip sizes are displayed, together with the corresponding connecting lines.*



To reduce the electronics noise the signal translation logic has been directly implemented on the PCBs. This circuit is essentially a level shifter and an amplifier of the multiplexed signal.

The technical designs of the PCBs have been carried out at INFN Cagliari, by using the software ALLEGRO from CADENCE package [Cad]. They have been produced by CERN laboratories.

### 6.1.2 Carbon fiber planes

To increase the cathode plane rigidity PCBs have been glued on sandwich panels ( $1280 \times 430 \text{ mm}^2$  area)<sup>1</sup>. The two outer parts,  $200 \mu\text{m}$  thick, are made by carbon fiber. The central part,  $5 \text{ mm}$  thick, is made by Nomex honeycomb. This replaced an uniform Rohacell layer, used in previous prototypes. The honeycomb should reduce multiple scattering effects.

The whole structure guarantees the required dimensional stability, a planarity better than  $100 \mu\text{m}$  over  $1 \text{ m}$ , the needed resistance to bending and mechanical stresses (originating, for instance, from wires mechanical tension) and the gas tightness.

In the non bending carbon fiber plane two holes are made for the gas way in and way out. In the bending plane a hole for the HV input cable has been drilled.

### 6.1.3 Insulating foils

Though the carbon fiber skins are impregnated with epoxy resin the panels showed a non negligible electrical conducibility on the surface. To isolate PCBs from them and to reduce capacitive noise a Nomex insulating layer [Dup],  $250 \mu\text{m}$  thick, is glued between cathode planes and carbon skins. Nomex relative dielectric constant is 4.

### 6.1.4 Anode wires

The  $20 \mu\text{m}$  W+Re gold plated wires have been put under tension on an aluminium frame by a winding machine, at CEA Saclay. A mechanical tension of  $0.5 \text{ N}$ , corresponding to the 75 % maximum allowable, has been used. They have been soldered on the spacer.

---

<sup>1</sup>They are produced by AEROFORME, Nantes [AER].

### 6.1.5 Spacers

To keep a gap of 2.5 mm between each cathode plane and anode wires, one frame (spacer) is glued on each half of the chamber. In this prototype spacers are made of standard FR4, 2.5 mm thick. Their shape is rectangular: they are 15 mm wide along the larger sides of the detector and 30 mm large along the smaller.

The spacer glued on the bending plane has a printed circuit on one surface. This circuit, comb-like shaped, allows wires soldering (fig. 6.3).

The teeth pitch is 2.5 mm. In each tooth a centering mark, 100  $\mu\text{m}$  wide, allows the wire positioning with an accuracy better than 50  $\mu\text{m}$ . The circuit guarantees also the electrical continuity between wires.

As in the carbon panel, a hole is drilled on the bending side to connect the HV cable and two on the non bending to allow, through steel tubes, the gas way in and out.

Other small holes, made on the frames, make possible the right coupling of the two half the detector, by means of pins.

## 6.2 Assembly procedure

The assembling procedure can be divided into three phases:

- gluing
- wire soldering
- detector sealing

### 6.2.1 Gluing

The gluing procedure has been performed in three steps: Nomex gluing on to the carbon fiber panels, PCBs gluing on this panel and then spacers gluing on PCBs. This procedure has been repeated for both bending and non bending planes.

A two-component epoxy resin, Araldite 2011 from Ciba-Geigy [Ciba], has been used for the whole gluing process. It shows good stress resistance and insulation features.

During the gluing phase caution must be paid to the following requirements:

- keep cathode planes flatness;
- guarantee the right alignment between PCBs, in order to respect the regularity in strip positioning;

Figure 6.3: *Mechanical design of spacers. An enlarged view of the printed circuit on which wires are soldered is displayed. It has been glued on the bending plane.*

- obtain a good mechanical coupling between the different detector elements.

To satisfy the last two points, reference pins have been inserted on precision holes drilled in the PCBs, the sandwich panels and the spacers. These pins, with a diameter of 3 mm, have a tolerance in their position less than  $20\text{ }\mu\text{m}$  and are left inserted during the gluing procedure.

To glue NOMEX and PCBs on the sandwich panel we followed the same method. A  $40\text{ }\mu\text{m}$  glue layer has been distributed on a as uniform as possible way in each plane. This value guarantees a good gluing without a relevant increase in the detector thickness.

The panel has been placed on a flat surface (optical table) and envelopped with a nylon foil. The vacuum ( $\sim 800\text{ mbar}$ ) has been made inside the foil to keep an uniform load during the glue drying phase (24 hours).

This procedure has been adopted to guarantee an uniform glue distribution and to avoid air bubble formation, which could generate variations in the detector gap and then in the gain.

The frames have been glued onto the PCBs by means of a little bristle brush, soaked in Araldite. Some lead bricks have been put over the frames as a load during the drying process.

In fig. 6.4 the non bending plane, after the overall gluing procedure, is shown. A detailed view of each bending plane element, after the gluing procedure, is shown in fig. 6.5. From bottom to top we can see the Nomex foil (white) glued on to the carbon fiber panel, the PCB region segmented into strips and the PCB zone dedicated to the electronics lodging. In this region the copper lines, going to the electronics connectors (soldered in the backplane) and the electronics circuit, soldered on the PCB, are clearly visible. The last element is the spacer, with the printed circuit for wires soldering.

### 6.2.2 Wires soldering

The wires have been soldered on the frame glued on the bending plane. This plane has been put on a mechanical support which allowed a fine movement in the vertical direction.

During the soldering procedure it is very important to keep the right wire positioning and mechanical tension. Each wire has been put within the centering mark by using a magnifying lens and a microscope.

In fig. 6.6 the wire plane, during the soldering procedure, is shown.

Figure 6.4: *X plane after gluing procedure.*

Figure 6.5: *Bending plane view. Cathode plane, spacer, sandwich panel and translator logic are visible.*

Figure 6.6:  $20\ \mu\text{m}$  W+Re gold plated wires put under tension. Under the wires the printed circuit (comb-shaped) for wires soldering is visible.

### 6.2.3 Detector cleaning

After gluing and soldering, the two detector halves have been cleaned with great accuracy. Any impurity could in fact cause discharges. For this operation a sable bristle brush soaked in Methylal has been used. This organic compound is very suitable for this purpose since it is degreasing but, at the same time, volatile. This means that a deep cleaning do not originate a residual humidity which could give rise to a circulating current between anode and cathode planes.

By increasing step by step the HV value before the detector closure it is also possible to check if the mechanical tension of some wire is too low.

### 6.2.4 Detector sealing

The coupling of the two chamber sides has been allowed by 3 mm pins inserted in the two carbon fiber panels. After the assembly the relative position of bending and non bending plane PCBs has been checked by means of a radiography, which shows an alignment within  $100\ \mu\text{m}$ .

In previous prototypes a final sealing procedure has been chosen. For the present detector a new technique has been proposed and tested: the sealing with silicone. This procedure could be very suitable in presence, for example, of a broken wire or an impurity inside the chamber. In this case the detector could be

easily opened, repaired and then re-sealed. This sealing technique will be used for the final slat chambers.

The used silicone, named EMAX SIL 93, shows particular features for what concerns the adhesiveness to a great number of materials. It is not corrosive, it does not harden, it does not shrink or become brittle as the time goes on. Moreover it is easily removed from the detector in case of re-opening.

In the outer side of the frames there is a 45 ° splay, to allow a better silicone adhesiveness. The deposition has been performed by means of a syringe with a big diameter needle. The drying process lasts about 24 hours. Due to the thin PCB thickness, some plexiglass plates have been interspaced between the two cathode planes, in the region dedicated to the electronics lodging, to reinforce them.

A raw mean radiation length estimate for the whole chamber gives a 0.92 %  $X/X_0$  value. In table 6.1 each material thickness and the corresponding radiation length is reported. The soldering and wires contribution have not been taken into account, but they are negligible.

Material	Thickness (mm)	$X_0$ (mm)	$X/X_0$ (%)
Copper	0.02	14.3	0.14
PCB (FR4)	0.2	194	0.10
Honeycomb	5	10000	0.05
Nomex	0.25	194	0.13
Glue	0.08	194	0.04
Total			0.46

Table 6.1: *Thickness, and corresponding radiation length, of each material used in each chamber plane. The contribution from electronics has not been taken into account.*

### 6.2.5 Checks on mechanical features

After the assembly some checks have been performed in Cagliari laboratories, before the test at CERN PS, in particular for what concerns gas leakage and electrical isolation.

We grounded the cathode planes and we increased the HV anode wires value, up to 2000 V, by means of a CAEN N471A power supply module [N471]. This allows to check the current leakage within 1 nA. The current value gives us some indications about, for example, impurities inside the detector or any broken wire in contact with the cathode plane.

At first, for  $HV = 1700$  Volt, the current value was  $\simeq 300$  nA. After some hours it decreased until 1 nA. Probably at the beginning some impurities were present inside the chamber. The HV dissolved them and they were ejected with the gas. This low current value means a good electrical isolation between anode and cathode planes.

By fluxing Argon inside the chamber and by using a gas leakage detector a good gas tightness was observed.

## 6.3 Test at CERN PS

After the assembly the prototype has been tested in May 2000, for one week, with a 7 GeV/c negative pion beam, at CERN PS.

### 6.3.1 Experimental set-up

The prototype, put in a movable test bench, which allowed the movement in x and y direction, has been located between ten silicon strip detectors [Leo87] located along the z beam axis (fig. 6.7).

They are grouped in five couples to measure the x and y track coordinates (two upstream and three downstream the prototype). They are  $300\text{ }\mu\text{m}$  thick, with 192 strips of  $50\text{ }\mu\text{m}$  pitch. The nominal accuracy in track reconstruction is within  $15\text{ }\mu\text{m}$ .

Figure 6.7: *Experimental set-up.*

The silicon detectors of the same couple are 15 mm apart along the beam



axis. Before the test a mechanical alignment has been performed. A subsequent correction via software will be performed.

Two crossed scintillators pairs are located upstream (overlapping surface =  $2 \times 2 \text{ cm}^2$ ) and downstream (overlapping surface =  $1 \times 1 \text{ cm}^2$ ). The coincidence signal given by the scintillators starts data taking.

The gas mixture, the chosen Ar 80 % and CO<sub>2</sub> 20 %, was furnished by a flowmeter and the gas overpressure (around 2 mbar) kept by a bubbler.

### 6.3.2 The readout system

The prototype used GAS64 boards (containing four  $1.5 \mu\text{m}$  GASSIPLEX chips each), directly plugged onto the detector.

The schematic view of a GASSIPLEX-based operation system is shown in fig. 6.8.

Figure 6.8: *Schematic representation of a GASSIPLEX-based operation system.*

It is composed by the following elements [HMPID]:

1. a trigger/control signal generator used to:
  - set the trigger modes: generator mode for pedestal measurements, or physics mode to record data from any experimental triggering array;

- send the T/H and CLEAR signals to the GASSIPLEX chains using level shifters adapting the logic signal levels to those requested in the chip;
  - start the MPX readout sequence.
2. a multiplexing CAEN Sequencer [V551B] used to:
    - send the CLOCK train to the GASSIPLEX chains and the digitizing units;
    - adjust the frequency, the number of CLOCK signals and the delay between the CLOCK trains.
  3. a 10 bit CAEN C-RAMS [V550A] to perform the analog/digital output conversion, the pedestal subtraction, the zero suppression.

Each chain was followed by a buffer amplifier driving a low impedance cable transporting the analog MPX signal to the counting room where the digitizers and data acquisition were located.

The HAMEG HM7042 modules [HAM] supply the low voltage ( $\pm 3.5$  V) to GASSIPLEX and the level shifters ( $\pm 5$  V).

The Data Acquisition system was based on DATE (Data Acquisition and Test Environment) program [Date], which allowed an on-line check of data taking. This is only a test configuration, due to the lack of the final electronics.

# Chapter 7

## Data analysis

The test performed at CERN PS in May 2000 made possible the study of many prototype features, in particular the spatial resolution (for both bending and non bending plane) and the efficiency as a function of High Voltage. The existence of cross talk effects has also been investigated.

During the test only six GAS64 were available. In fact the GASSIPLEX 1.5  $\mu\text{m}$  chips, on which GAS64 are based, were out of production and the newer GASSIPLEX version (0.7  $\mu\text{m}$ ) was not yet on the market. Thus we installed three cards per plane. It was so possible to study, each time, only 192 strips per plane. Both planes were studied together but it was not possible to test, at the same time, the upper and the lower zone of the cathode planes.

The following data analysis concerns the test of both bending and non bending plane upper region of the central cathode planes. In this zone the strip size is  $5 \times 25 \text{ mm}^2$ , which corresponds to the highest density in the bending plane, while in the non bending plane is  $7.143 \times 25 \text{ mm}^2$ .

### 7.1 Results

#### 7.1.1 Pedestal study

When the T/H signal is set (section 4.4), each output is raised at a constant DC level in the absence of an input signal. This baseline, called *pedestal*, is channel-dependent within the chip and has to be subtracted from the physical signal. The average (PED(i)) and r.m.s. (SIG(i)) values of a pedestal distribution are recorded in the CRAMS modules, to allow both an on-line or off-line pedestal subtraction. It is very important to know exactly the pedestal value and its oscillation since it influences the precision in charge measurement and so in the spatial resolution, since it depends on the signal to noise ratio.

The sigma pedestal can be used to set a fixed threshold value to every channel. This procedure has the advantage to take into account only the events which overcome the threshold and to reject the others (zero suppression).

The threshold of the channel (i) is defined as:  $TH(i) = PED(i) + N \times SIG(i)$ , where N is a selectable constant. This value should be chosen as a good compromise between a complete pedestal rejection and a minimum loss of physical information.

An off-line 3 sigma cut has been performed on CSC signals while for silicon detectors a 4 sigma cut, made on-line, has been used.

During the test some dedicated runs are performed to check the pedestal stability. In fact their value depends on several factors, like temperature fluctuations, low voltage stability and possible detector leakage current. In these runs the trigger signal is given by a pulse generator.

In fig. 7.1 a typical pedestal mean value for both planes, as a function of channel number, is shown. The channels greater than 192 correspond to strips not connected to the electronics.

Figure 7.1: *Pedestal value (in ADC ch.) as a function of channel number, for bending and non bending plane. The channels greater than 192 are not connected.*

The corresponding sigma value, for both planes, is reported in fig. 7.2. In the bending plane the sigma mean value is about 1.8 ADC ch. It is also possible to distinguish three regions, in which the sigma values show different trends. Each region corresponds to 64 channels and so to one GAS64. This means that the noise induced by the readout electronics depends on a strictly way on the particular connected circuit.

Figure 7.2: *Sigma pedestal behaviour as a function of channel number, for both planes. The channels greater than 192 are not connected.*

The non bending plane shows a larger noise ( $\simeq 3$  ADC ch.), probably due to larger strip sizes. In this plane the sigma behaviour shows a periodical oscillating structure. Beyond the noise originated by GASSIPLEX a component coming from the capacitance between connecting lines and strips must be taken into account.

To check this we studied the correlation between the sigma value and line length, for both planes. Results for non bending plane are plotted in fig. 7.3. The channels belonging to each GASSIPLEX (16 ch.) have been represented with the same symbol. These results confirm that longer lines induce more noise and that the behaviour of the noise as a function of line length is linear.

The results concerning the bending plane are displayed in fig. 7.4. Two distinct distributions are now shown. The trend is the same in both cases, i.e. the noise rises as the line length increases, but the sigma mean values are different.

Let's now take into account, as an example, the GASSIPLEX whose channels go from 97 to 112. Fig. 7.4 shows that exactly 8 channels belong to one distribution and the remaining 8 to the other. Also other GASSIPLEX chips show this behaviour. Moreover, the 8 channels belonging to a distribution are ever the even ones and the other 8 are the odd ones. We investigated if this behaviour could be attributed to a bad functioning of readout electronics. In fact, the pins which allow the signal transmission from the connectors soldered on the PCBs to the GAS64 are divided in two lines. They are numbered in such a way that the even ones are all grouped along a line and the odd ones in the other (see fig. 4.20,

Figure 7.3: *Correlation between connecting line length and pedestal sigma (non bending plane) for channels connected to different GAS64.*

Figure 7.4: *Correlation between line length and pedestal sigma (bending plane) for channels connected to different GAS64.*

bottom).

We checked if the GASSIPLEX channels showing this behaviour were the same in all GAS64, but this doesn't happen.

We supposed also a damage in the connectors soldered on the PCBs, but in this case a random (and not so regular) behaviour was expected.

The only possible explanation seems to lie in a bad electronics working, though the specific reason is not yet understood.

This test has been made with a temporary and insufficient electronics. Next test has been made with GASSIPLEX 0.7  $\mu\text{m}$ . This allowed to achieve more reliable results, by using configurations similar to the final ones.

## 7.2 Study of bending and non bending plane response

When a particle crosses the detector a charge is induced on one or more strips belonging to both cathode planes. A group of adjacent hit strips makes a so called *cluster*. The cluster dimension depends on the anode High Voltage, as we will see better later.

The cluster-finding algorithm connects all the close hit strips in the y and x directions [MUOAD] and the cluster position is obtained by using a COG algorithm (section 7.3).

One or more cluster can be produced in an event and each of them can be made by one or more hit. The cluster with the higher amount of deposited charge is defined as *first cluster* (cluster[0] in the following). In the other clusters (second, third and so on) the amount of charge is gradually decreasing.

The following data analysis mainly concerns the study of clusters and number of hit strips, in particular for the first cluster, in bending and non bending plane.

### 7.2.1 Bending plane

Fig. 7.5 (left) shows that in the majority of the events only one cluster is formed. Less than 20 % of total events show two clusters and those with three or four clusters are about 5 %. When in an event more than one cluster is generated only that with the higher amount of charge is due to the particles crossing the chamber<sup>1</sup>.

By increasing the HV value to 1700 V also the number of events with more than one cluster increases.

---

<sup>1</sup>Pile-up effects at PS beam are in fact negligible.



Figure 7.5: *Number of clusters for two HV values.*

In fig. 7.6 the number of hit strips, for the first cluster, is plotted. An increase in cluster dimensions as a function of anode voltage is shown. In fact, as the voltage increases also the charge on cathodes increases, since the gain on the anode wire increases. In this way the number of strips over threshold is higher and now they are measured. At  $HV = 1600$  V, for example, the mean number of fired strips is 3. This number grows up to 3.5 at  $HV = 1700$  V.

In fig. 7.7 the same distribution is plotted for several clusters (up to the fourth) and for two runs (at 1600 V and 1700 V). The second cluster (and followings) is made by only one hit strip and this distribution does not change too much as the voltage increases.

In fig. 7.8 the first cluster charge distribution is plotted for a run at  $HV = 1600$  V. Though this shape well approaches the foreseen Landau distribution, saturation effects cannot be disregarded.

Data taking with different working voltages were performed and for each of them a good approximation of the theoretical distribution has been obtained. As the High Voltage increases saturation effects, due to events with a charge overcoming the ADC dynamical range (overflows), become more and more marked. These effects are less evident for low HV working values, for some of which they disappear at all.

In fig. 7.9 the charge distribution for the first fourth clusters is plotted, for example, for two voltage values (1600 V on left and 1700 V on right). As we can see the amount of charge in the cluster greater than the first is negligible and can be easily rejected.

Figure 7.6: *Number of hit strips, in the first cluster, as a function of High Voltage.*

Figure 7.7: *Hit strip distribution for cluster from first to fourth, for two voltage values (1600 V at left, 1700 V at right).*

Figure 7.8: *First cluster charge distribution ( $HV = 1600$  V).*

Figure 7.9: *Charge distributions for different clusters and different voltages.*

Taking into account only the first cluster we fitted the charge distributions for different HV values with a Landau function. By each fit we obtained the peak value (most probable value) which, plotted as a function of HV, represent the behaviour of the relative gain of the chamber (fig. 7.10).

An anomaly can be observed at  $HV = 1700$  V. In fact two different runs, made at different times, but at the same working voltage, show different charge values. This behaviour could be originated by possible fluctuations in atmospheric pressure, readout electronics, or in HV stability, which can lead to a change in gain.

We also studied the amount of charge induced in each strip of a cluster. We required, at 1600 Volt, a cluster in the bending plane made by three contiguous strips. The strip for which the amount of induced charge is the highest, with respect to the other two, is defined as *first strip*. The fraction of charge deposited in the first strip, with respect to the others, depends on the impact point position. To have an idea about this value we found, by averaging over a run, that about 70 % of total charge is induced on the central strip, while the remaining 30 % is shared by the other two, as shown in fig. 7.11.

The fraction of charge induced in each of the three strips, with respect to the first cluster total charge, has been then evaluated as a function of High Voltage and results are displayed in fig. 7.12. In this figure the first, second and third strip behaviour are displayed, from top to bottom, according to their amount of induced charge. The charge of the first strip decreases as the working voltage increases. This effect is probably due to a saturation effect on the central strip

Figure 7.10: *Most probable value of first cluster charge (in ADC channels) as a function of High Voltage.*

measured charge.

### 7.2.2 Non bending plane

The bending plane features, just presented, have also been investigated for the non bending one.

The number of clusters, at 1600 V, is shown in fig. 7.13. By comparing this plot with fig. 7.5 (left), referring to the same run, we can see that the mean cluster number in the non bending plane is two while in the bending plane is one. This behaviour will be explained later.

The cluster dimension as a function of the operating voltage is plotted in fig. 7.14. The reduced dimension, with respect to the bending plane, is due to the fact that the strips are 1.5 times larger than in the bending.

The correlation between the charge induced in bending and non bending planes has been studied. The behaviour, as expected, well approaches a straight line (fig. 7.15).

## 7.3 Software alignment of silicon detectors

One of the main aims of the test was the evaluation of the prototype spatial resolution in both planes.

To reconstruct particle paths an external tracking system, used as reference, is needed. Its precision in track reconstruction must be better than that expected

Figure 7.11: *Induced charge on the central strip (top) and in the neighbouring two (center and bottom).*

Figure 7.12: *Fraction of charge induced in each of the three strips, with respect to the first cluster total charge, as a function of High Voltage (central strip: top).*

Figure 7.13: *Number of cluster in the non bending plane (HV=1600 V).*

from the prototype.

During the test a telescope system made by ten silicon strip detectors has been used (section 6.3.1). Five of them have been used to measure the x positions, the other five measured the y ones.

To estimate the beam particle coordinates firstly the deposited charge on silicon microstrip has been read and a cluster found. The cluster coordinates in both planes, x and y, have then been calculated by means of a weighted mean of the charge induced on the strips, using a **C**enter **O**f **G**avity algorithm:

$$y_{cog} = \frac{\sum_{i=1}^{3,4,5} y_i Q_i}{\sum_{i=1}^{3,4,5} Q_i} \quad (7.1)$$

where  $y_i$  represents the central position of  $i^{th}$  strip and  $Q_i$  is the induced charge on that strip.

If z is the beam direction it is therefore possible, for each event, to reconstruct the particle path with silicon detectors in each xz and yz planes.

Before the test a rough mechanical alignment has been done and the z position of each silicon plane has been measured. A subsequent check and software correction is made in the following way. The particle path is reconstructed by taking into account four silicon planes each time and by excluding the plane for which we want to check the alignment. The particle trajectory is then recon-



Figure 7.14: *Non bending plane. Number of hit strips in the first cluster.*

Figure 7.15: *Correlation between charge induced in bending and non bending plane.*

structed by means of a linear fit of the positions given by these silicon detectors. This track is projected on the excluded plane and a coordinate is extrapolated from the fit. The position of the cluster, on such plane, can be calculated by means of the COG algorithm. The difference between the measured position and the track projection on such plane is called *residual*. This procedure is iterated for each plane and it allows to know the relative displacement of silicon planes. When all planes are correctly aligned all residual distributions must be centered on zero [Kha99]. This software correction is made for both x and y planes. In fig. 7.16 the x and y displacements of the five planes as a function of their position along the z axis are shown for one event.

In fig. 7.17 the residual distribution for the first silicon plane is plotted. We fitted it with a gaussian function in the  $\pm\sigma$  range, to avoid the tails, due to background. The sigma value resulting from the fit  $((39 \pm 3) \mu\text{m})$  represents the spatial resolution for that plane.

### 7.3.1 Position reconstruction

To determine the impact point position of a particle on the detector the intersection of the straight line (given by the silicon detectors) with the chamber plane is considered. Two coordinates, x and y, are thus extrapolated and represent the *true* position of the track on the detector under test. The extrapolated coordinates are then subtracted by the coordinates of the first cluster position, calculated by means of the COG algorithm. The y cluster position is obtained by the bending plane, the x by the non bending.

In fig. 7.18 the beam shape, extrapolated by silicon detectors and projected onto the chamber plane, is displayed.

Figure 7.16: *Silicon planes displacement from zero position (left: x coordinate, right: y coordinate).*

The x and y beam coordinates, extrapolated from silicon detectors, are plotted in fig. 7.19 (on top). The corresponding coordinates, furnished by the prototype and calculated with the COG algorithm, are shown on bottom. In the non bending plane (left) some peaks, corresponding to the wire structure, are clearly shown. In the bending plane (right) three regions, corresponding to the strip dimensions, are displayed. This implies a position reconstruction dependence on the chamber geometrical parameters (wire pitch, strip dimensions).

The continuous background is due to particles which cross the chamber in a not straight way. The double peaks are due to particles crossing the chamber at right and at left of the anode wire.

In fig. 7.20 the correlation between the track coordinates, extrapolated by silicon detectors and reconstructed by the CSC, is shown.

An influence of wire position in cluster position determination is clearly shown in the non bending plane. The behaviours showed in fig. 7.19 and 7.20 have been already observed by Charpak group [Cha79].

## 7.4 Efficiency

One of the most important features of a particle detector is the efficiency, i.e. the ratio of selected events recorded by the chamber, which get through some selection criteria, to the total number of events.

Figure 7.17: *Residual distribution, in x direction, for the first silicon detector plane.*

Figure 7.18: *Beam projection on to the chamber.*

For what concerns the bending plane we selected the events which satisfy the following criteria:

- events with at least one cluster;
- selection in the number of hit strips;
- overflow rejection.

The first condition simply requires a physical signal in the chamber. It is satisfied in the 99.5 % of events and there is no dependence on the beam impact point on the chamber (fig. 7.21). If there is more than one cluster only the first one will be taken into account.

The overflow rejection is necessary to evaluate in the right way the position reconstructed by means of the COG algorithm. At low operating voltages this cut reduces the total statistics by only 3 %. By attenuating the signal as input to the ADC it should be possible to reduce the inefficiency due to overflows.

To reconstruct with high precision the crossing point of particles through the chamber we have to select clusters made by more than two fired strips. We will show later how efficiency and resolution vary as a function of the number of hit strips involved in their estimation.

Figure 7.19:  $x$  (left) and  $y$  (right) beam coordinates extrapolated from silicon detectors (top). The same distributions, obtained from the CSC, are plotted on bottom.

Figure 7.20: *Correlation between track coordinates extrapolated by silicon detectors and those reconstructed by the CSC. On left: x coordinate (non bending plane), on right: y coordinate (bending plane).*

Figure 7.21: *Events with at least one cluster, as a function of the particle impact point on the chamber.*

In fig. 7.22 (left) the y coordinate distribution (deduced from silicon detectors) is reported. This refers to bending plane and it has been obtained without any requirement on the number of fired strips on the chamber. The plot on right has instead been obtained by requiring a cluster made by more than two hits. By comparing these figures a decreasing of about 21 % of events is noticed.

Figure 7.22: *y coordinate distribution without any requirements on the number of hit strips (left). The same distribution, obtained by requiring a cluster made by more than two fired strips, is showed in the plot at right.*

The ratio of these distributions leads to the result shown in fig. 7.23. This represents the cut efficiency as a function of y coordinate. An efficiency decrease in particular positions can be observed. These minimum values correspond to the interstrip structure.

The behaviour showed in fig. 7.22 can be also represented in a bidimensional way (fig. 7.24).

The tracks crossing the chamber, for different number of hit strips, are here shown. Different colour regions correspond to different track percentage getting through the selection.

For what concerns the non bending plane, the requirement of more than one hit in the first cluster does not affect the x distribution structure (fig. 7.25, on left). The efficiency decreases by 20 % in an uniform way as a function of x (fig. 7.25, on right).

By requiring a cluster with more than two hit strips the percentage of tracks decreases in a considerable way. In the non bending plane, in fact, the strips are longer along the wire direction. This implies less fired strips, in this plane, with



Figure 7.23: *Ratio of events with a cluster made by more than two hits to the events without requirements on hit strips, as a function of y track coordinate.*

Figure 7.24: *Bidimensional view of the coordinate distribution without any cut on fired strip number (left). The same plot, but with the requirement of a cluster made by more than two hit strips, is represented on right.*

respect to the bending one.

Figure 7.25: *x* coordinate distribution, extrapolated from silicon detectors (on left). One hit strip in the cluster has been required. On right: ratio of tracks with more than one strip in the first cluster to all events reconstructed by silicon telescope.

The efficiency depends in a critical way on the anode voltage. In fact, the higher will be the voltage the higher will be the gain and then the signal. This implies an improvement in the signal to noise ratio and then in the efficiency.

The efficiency, as a function of anode voltage, has been evaluated by applying two different cuts:

- $n_{\text{hits}} > 1$  and cut on the overflow events;
- $n_{\text{hits}} > 2$  and no cut on the overflows.

Results are plotted in fig. 7.26. In the first situation the efficiency at low operating voltages is high since also small clusters are accepted. It decreases instead as the voltage increases owing to the larger number of overflow events. To estimate in the right way the resolution these events have to be rejected, leading to an efficiency decrease.

In the second situation the cut on cluster dimension is more strict and the efficiency behaviour is the expected one. At low anode voltage, in fact, the main part of events show clusters with two hit strips. These events are rejected by our requirement and this explains the low values in the rising part of the efficiency curve.

Figure 7.26: *Efficiency curve as a function of high voltage, for two different event selection.*

Both cuts (on hit number and on overflow events) are important to evaluate in the right way the resolution value. The optimal working voltage must be therefore a good compromise between efficiency and resolution.

In fig. 7.27 the efficiency curve, obtained by requiring a cluster with at least three hit strips and the cut on overflows is shown.

The efficiency stays approximately constant ( $\simeq 80\%$ ) in the range between 1600 and 1650 Volt. This suggests to choose the appropriate operating voltage in this interval.

## 7.5 Estimation of spatial resolution and event selection

To evaluate the resolution we have to know the residual distribution, i.e. the difference between the track coordinates given by the silicon telescopes and those given by the CSC and calculated by using a COG algorithm (section 7.3). The spatial resolution is defined as the standard deviation ( $\sigma$ ) of a Gaussian fit to the residual distribution.

We selected the events by excluding the overflows and by requiring a cluster

Figure 7.27: *Reconstruction efficiency as a function of High Voltage. The events have been selected requiring a cluster with, at least, three hit strips and no saturated measured charges (bending plane).*

made by more than three strips. In fact, the goodness of the COG algorithm increases with the number of involved strips. If only one strip is taken into account the position of the cluster is simply given by the center of the strip. At the same time including too many strips in the COG calculation is not a so convenient procedure. While the electronics noise stays constant the signal decreases for peripheral hit strips. This low charge to noise ratio leads to a resolution degradation if such strips are taken into account in the resolution estimation. We will show later the behaviour of the resolution as a function of the number of hit strips.

### 7.5.1 Bending plane resolution

As already explained to evaluate the track position in the chamber the COG method has been used. This introduces a systematic error. The charge distribution, in fact, is not linear. The charge fraction induced on a strip does not depend in a linear way on the impact position on this. Such geometrical effect is shown in fig. 7.28. A correlation between the coordinate, measured by the chamber in the bending plane, and the residual value is displayed.

To correct this error we divided the coordinate range in several intervals. For each of them we evaluated the mean value of the residual. Each distribution has been translated in such a way that the mean value became 0 and the different distributions have been cumulated. An independence of the results on the interval number and on the chosen range has been verified. A gaussian fit has been performed to such a corrected residual. As an example we show the resolution value for a run at 1600 V (fig. 7.29, left). To exclude the tails, due to background, the fit range has been restricted to  $\pm 2\sigma$ . The value obtained from the fit equals  $\simeq 88\ \mu\text{m}$ .

For comparison, in the right part of the same picture the resolution, coming from a gaussian fit on the not corrected residual, is shown. The resolution gets worse and equals  $\simeq 118\ \mu\text{m}$ .

In fig. 7.30 the evolution of the resolution as a function of the High Voltage is shown. This is due to the increase of the induced charge on the strips and so to a signal to noise ratio improvement.

We selected the events by requiring a cluster with three and four hits and we evaluated the resolution value for these two different situations. Fig. 7.31 shows that the best resolution value is achieved by requiring a cluster with three strips. In fact, most of the charge is induced on the central strip and the remaining part is shared between the two adjacent ones (see fig. 7.11). The fourth hit strip is, in general, due to cross talk effects (section 7.6). By taking it into account in the resolution evaluation, a coordinate shift towards its position and, as consequence a  $10\ \mu\text{m}$  worsening, is obtained.

Figure 7.28: *Residual distribution as a function of the coordinate measured by means of the chamber (bending plane).*

Figure 7.29: *Corrected residual distribution (bending plane) fitted to a gaussian fit (on left). The resolution obtained from the gaussian fit to the not corrected residual distribution is shown on right.*

Figure 7.30: *Bending plane resolution as a function of High Voltage.*

Figure 7.31: *Residual distribution for a cluster made by 3 (solid line) or 4 (dashed line) hit strips.*

To evaluate the resolution in a right way non negligible multiple scattering effects suffered by PS beam particles during the test should be included. The impact position is determined by means of a linear fit to the coordinates given by silicon detectors. If there are multiple scattering effects there is a deviation in particle path. This is so not correctly described by a linear fit and the impact point position projected on the chamber is no more right.

We tried to reject the wrong reconstructed events by asking a cut on the  $\chi^2$  fit of the track. The resolution improvement equals only  $5 \mu\text{m}$  (fig. 7.32).

### 7.5.2 Non bending plane resolution

The residual distribution for the non bending plane has been obtained in the same way of the bending. Its behaviour as a function of the x coordinate (fig. 7.33) in this case shows a structure correlated to the wire pitch (the longer strip size is now parallel to wires). The impact point coordinate has been evaluated by using the COG algorithm.

The resolution value, obtained from a non corrected residual, is  $819 \mu\text{m}$  (fig. 7.34) for a run at 1600 Volt.

By applying the correction already explained on the residual distribution an im-



Figure 7.32: *Bending plane resolution after the cut on the  $\chi^2$  fit of the track.*

provement in the spatial resolution has been achieved. Now a great attention must be paid in the choice of the interval pitch in which the distribution is divided. In fact it would be meaningless to choose a range less than the wire pitch  $s$ . The theoretical resolution, for the non bending plane, is in fact correlated to it through the expression  $\frac{s}{\sqrt{12}}$ . The theoretical value is  $\simeq 700 \mu\text{m}$  and the experimental one, after the residual correction, is  $659 \mu\text{m}$  (fig. 7.34).

## 7.6 Cross talk effects

As already explained the cluster due to a physical event (particles crossing the chamber) is one. It is simple to recognize it, since it is characterized by the biggest amount of charge deposited in an event.

Sometimes more than one cluster is present. The percentage of these events, essentially due to noise, rises as the anode voltage increases.

When the particles go across the detector a certain amount of charge is induced on the strips. The signal is transmitted by the connecting lines in the PCB backplane (fig. 6.1) to the readout electronics (GAS64). During this process a fake signal can be induced in the neighbouring strips, lines, GAS64 or even in the connectors soldered in the PCB and in which the readout electronics is plugged.

Figure 7.33: *Residual behaviour as a function of the x coordinate, measured by means of the chamber.*

Figure 7.34: *Residual distribution (not corrected) for the non bending plane (left). On right the same distribution is shown after the correction.*

Thus there is a possible *cross talk* effect due to the capacitive effects between the PCB frontplane and backplane.

Owing to the reduced PCB thickness ( $200\ \mu\text{m}$ ) and the distance between the lines ( $250\ \mu\text{m}$ ) this effect was expected in the detector under study.

To check if the events with more than one cluster are originated by such effect, a run at 1600 Volt (for the bending plane) has been examined. As a result about 23 % of the total events have more than one cluster.

These are formed either by one hit or more than one fired strip. The first situation is the most probable ( $\simeq 72\%$  of events with more than one cluster). In this case the amount of deposited charge is very small (fig. 7.35, right). The following analysis will concern only this kind of cluster.

The correlation between the hit strips in the first and in the second cluster has been studied. Results are shown in fig. 7.36. On average there are three hit strips in the first cluster and one in the second. There are also some events (about the 8 % of total) with a four strip first cluster and a single isolated strip in the second. A small percentage of events (about 6 % of total) shows three hits in the first cluster and two in the second.

To check cross talk effects in the detector the relative positions of the second cluster with respect to the first has been studied. Actually fig. 7.37 (left) shows an accumulation of events in a well defined region.

To understand where the cross talk effect takes place we selected the events by requiring only one hit strip in the first cluster. This strip has been identified

Figure 7.35: *On left the number of hit strips for the second cluster is shown. The charge distribution for the same cluster is presented on right.*

with the number 340 and its coordinate are (58.75, 15.25). In the 19 % of events a signal in the strip 341, whose coordinates are (56.25, 13.25), is induced. They are not contiguous strips since, along the y direction, they are 2 cm apart. The corresponding lines end into close pins in the connector soldered in the PCB for the GAS64 lodging, but they are not one in front of the other, as shown in fig. 7.38.

Since the cross talk effect does not seem to happen in the connector a readout electronics bad working has been supposed.

In any case, the second cluster with one hit strip ( $\simeq 16$  % of events) shows a charge amount negligible with respect to that of first cluster.

The situation in which both clusters contain more than two hit strips has been studied. The relative position of the second cluster, respect to the first, is shown in fig. 7.39. A cluster distribution along the connecting line direction can be clearly observed.

A combination of cross talk between connecting lines *and* between them and the strips has been supposed. This effect could be due to the reduced PCB thickness and could be the cause of such diffused charge distribution.

## 7.7 Summary

In the previous chapter the building of a large size CSC prototype for the ALICE experiment has been presented.

Figure 7.36: *Correlation between the number of hit strips in the first and in the second cluster.*

From the mechanical point of view a good mechanical tolerance in the coupling of the two cathode planes and gas tightness have been achieved. A very good electrical isolation between anode and cathode planes has been obtained.

The analysis of data coming from a test performed at CERN PS with a 7 GeV/c pion beam, discussed in details in this chapter, presented the following results:

- the correlation between the sigma pedestal value and the line length is linear;
- 90  $\mu\text{m}$  spatial resolution in the bending plane and about 650  $\mu\text{m}$  in the non bending;
- 80 % efficiency for  $1600 \leq \text{HV} \leq 1650$ . This low value is due to overflow events;
- in the bending plane 3 % of total events shows a cross talk effect between different electronic channels. Moreover 6 % of total events show a second cluster, with a charge comparable to first.

The electronics has shown an inadequate dynamical range, which leads to saturation effects. This should be solved with the use of 0.7  $\mu\text{m}$  GASSIPLEX

Figure 7.37: *Position of the second cluster with respect to the first (left).*

Figure 7.38: *Pins connector scheme. Each number corresponds to a different line and so to a different strip.*

Figure 7.39: *Position of the second cluster relative to first, when both are made by more than two hit strips.*

version. By attenuating the signal it should be possible to reject the overflows and to achieve a 95 % efficiency value.

The PCB thickness (200  $\mu\text{m}$ ) was too thin with respect to its surface. The thickness will be doubled in next prototypes to increase its mechanical strenghtness and to improve the isolation between the printed circuit frontplane and backplane. This should lead to a noise reduction.

These hints have been taken into account in the construction of a small size prototype and checked during a test performed in Cagliari laboratories and at CERN PS.

This will be the subject of next chapter.





# Chapter 8

## A prototype with large size strips

The CSC prototype building and test, presented in the previous chapter, put in evidence some problems both in the electronics (an insufficient GASSIPLEX dynamical range) and in the PCB (a too reduced PCB thickness).

The R&D phase went on, during 2001 year, with the realization of a small size prototype, made by only one PCB per cathode plane (400 mm  $\times$  400 mm active area). By constructing it we tried to solve the problems showed by the previous prototype.

This detector has been built in Cagliari laboratories and there tested with a  $^{90}\text{Sr}$  source<sup>1</sup>. It has been later in-beam tested at CERN PS.

In the following the main prototype characteristics and the data analysis obtained by using the source will be presented. The main results obtained from PS test will be discussed at the end of the chapter.

### 8.1 Prototype characteristics

The prototype has been designed and assembled between October 2000 and April 2001. The main task was to test, for the first time, the response of large size strips (100 mm long), that will cover the outer region in ALICE slat chamber surface (low density strip region).

The main points to test were:

- noise in long strips compared to the small ones;
- choice of insulator between cathode plane and sandwich panel;
- new PCBs, 400  $\mu\text{m}$  thick instead of 200 (like in the previous prototype);

---

<sup>1</sup>Strontium-90, with a half-life of 29 years, decays in Yttrium-90 by emission of a relatively low-energy beta particle (0.546 MeV maximum).

- test of the new readout electronics based on GASSIPLEX 0.7  $\mu\text{m}$  chips.

Since each detector element has been previously described in details in chapter 6, only the differences with respect to the previous prototype will be put in evidence in the following.

### 8.1.1 Cathode planes

#### Description

The two cathode planes are made by two double sided PCBs. The total area of each of them is  $400 \times 580 \text{ mm}^2$ , with a  $400 \times 400 \text{ mm}^2$  active surface. The dielectric thickness is 400  $\mu\text{m}$ , doubled with respect to the year 2000 prototype. The Cu base layer is 5  $\mu\text{m}$  and  $\simeq 20 \mu\text{m}$  after recharge.

The connecting line from each strip to the corresponding pin in the readout connector is 150  $\mu\text{m}$  large and the minimum distance between lines is 300  $\mu\text{m}$ . The vias diameter is 0.3 mm.

The PCB thickness has been chosen not only to guarantee a better rigidity to the cathodes and an isolation between the two PCB sides. The 400  $\mu\text{m}$  value has, in fact, been also chosen in view of the impedance coupling to the digital bus, when the final readout electronics will be employed.

The LVTTL bus will connect the MANU345 cards of each cathode plane (fig. 8.1). The connection of this bus with the opposite slat chamber side will be probably made by means of Kapton cables in the left or in the right PCB side.

The impedance of the LVTTL bus has been evaluated through the following expression [Cou00]:

$$Z_o = \frac{60}{\sqrt{0.475 \cdot \epsilon_r + 0.67}} \times \ln\left[\frac{4 \cdot h}{0.67 \cdot (0.8 \cdot W + t)}\right] \quad (8.1)$$

The geometrical parameters, involved in this equation, are put in evidence in fig. 8.2.

The obtained impedance value ( $\simeq 64.5 \Omega\text{m}$ ) is too low since it should be close to MARC output ( $\simeq 100 \Omega\text{m}$ ). To increase  $Z_o$  it is possible either to decrease  $W$  (the width of the bus strip) or to increase the PCB thickness ( $h$ ). A  $W$  decrease would cause a mechanical weakening. By increasing  $h$  up to 400  $\mu\text{m}$  the impedance achieves an acceptable value ( $\simeq 89 \Omega\text{m}$ ).

#### Design

The PCBs have been designed at INFN Cagliari, by using the software ALLEGRO from CADENCE package [Cad].

Figure 8.1: *LVTTL and LVDS buses.*

Figure 8.2: *Cross section of a PCB plane. Each geometrical parameters involved in LVTTL impedance calculation is indicated.*

Figures 8.3 and 8.4 show the mapping of the bending and non bending planes respectively.

Figure 8.3: *Bending plane strip array. The two strip dimensions are indicated.*

Most of the active area is covered by large size strips whose dimensions are  $100\text{ mm} \times 5\text{ mm}$  in the bending plane and  $8.33\text{ mm} \times 100\text{ mm}$  in the non bending plane.

Such values correspond to the lowest particle hit density region in the Muon Arm slat chambers. The response for strip  $100\text{ mm}$  long has not yet been tested. The value  $8.33\text{ mm}$  has been chosen to optimize the number of electronics channels. With the present choice in fact ( $7.143\text{ mm}$ )  $3.5\text{ MANU}$  are used in the non bending low density PCB, leaving 32 channels unused. Simulations have been performed

Figure 8.4: *Non bending plane strip array. The two strip dimensions are indicated.*

to evaluate the efficiency to find the hit wire along x direction as a function of strip width [Bal01]. Results show that the efficiency achieves an optimum value even for a 8.33 mm strip width (fig. 8.5). With such a choice the number of readout chip modules will be optimized.

Figure 8.5: *Efficiency to identify the hit wire as a function of strip width.*

There is also a small area in both planes in which we placed small size strips. The strip size in this region is 25 mm  $\times$  5 mm in the bending plane and 25 mm  $\times$  8.33 mm (these dimensions correspond to the highest density). This choice has been made to compare some features like noise, total charge induced on cathode planes and hit number of strips for different strip dimensions in the same prototype and in the same test conditions.

### **Mechanical tolerances**

The cathode planes have been produced by ERMES Technology (Turin, Italy). Since this prototype has only one PCB circuit per cathode plane, geometrical tolerances are not so critical. Nevertheless a careful check on PCB dimensions has been performed to validate the capability of ERMES to reach the required quality for a possible future final production.

To measure the circuits the pointing device has been employed. A good dimensional stability, within 100  $\mu\text{m}$ , has been put in evidence.

### 8.1.2 Sandwich panels

To ensure the planarity and stiffness to cathode planes the same kind of panel (carbon-Nomex honeycomb-carbon sandwich) previously described<sup>2</sup> has been used for this prototype.

A hole is drilled on bending side to connect the HV cable and two are made on non bending side for gas tubes.

### 8.1.3 Insulating foils

A NOMEX foil<sup>3</sup>, 250  $\mu\text{m}$  thick, has been interspaced between the panel carbon skin and the PCB backplane, to ensure an electrical isolation and a reduction in capacitive noise.

To crosscheck our results another prototype, identical to this except the insulator (1 mm Nomex honeycomb), has been assembled at the same time at CEA Saclay.

### 8.1.4 Anode wires

The used wires are the standard W gold plated, reinforced with the addition of 3 % of Rhenium<sup>4</sup>. The diameter is 20  $\mu\text{m}$ .

This time the wires have been manually stretched on a frame provided with 2.5 mm pitch grooves.

Before the closure a check on the chamber has been made by increasing, step by step, the High Voltage.

### 8.1.5 Spacers

As already described in section 6.1.5 the spacer is made by a FR4 comb-shaped circuit on which wires are soldered.

In table 8.6 the large and small prototypes main characteristics have been reported and compared. The doubled FR4 thickness increases the relative detector radiation length by only 0.20 %.

---

<sup>2</sup>See section 6.1.2 .

<sup>3</sup>See section 6.1.3.

<sup>4</sup>See section 6.1.4.

Figure 8.6: *Comparison between the characteristics of the large (2000 year) and the small (2001 year) prototypes.*

### 8.1.6 Assembly and first checks on prototype

The reduced dimensions of this detector simplified the assembly procedure. This is very similar to the previous prototype. The reader is therefore referred back to section 6.2.

A spare detector has also been assembled. The only differences between the two prototypes concern the number of edge wires (two on each side in the first prototype, one on one side and three in the other side in the spare prototype) and in the sandwich panel (honeycomb in the first, Rohacell in the second).

After the assembly a good gas tightness and electrical isolation between anode and cathode planes was checked in Cagliari laboratories.

## 8.2 Test with $^{90}\text{Sr}$ source

The performances of the prototype have been firstly studied by exposing it to a  $^{90}\text{Sr}$  source. The experimental setup is reported in fig. 8.7. The coincidence signal, given by two crossed plastic scintillators (one on top and the other on bottom), starts data taking.

In fig. 8.8 the assembled prototype, between two crossed scintillators, is shown. The source is inside the lead collimator, over the upper scintillator. The electronics is plugged on the outer PCB region.

One filter has been used to reduce the external noise. The readout electronics plugged on the prototype was based on GASSIPLEX 0.7  $\mu\text{m}$  chips. The multiplexed signals from GAS64 were sent to 2 CAEN VME C-RAMS modules, driven by a V551 SEQUENCER. One C-RAMS was equipped with a 12 bits ADC



Figure 8.7: *Schematic view of the experimental setup used in Cagliari laboratories.*

Figure 8.8: *Experimental setup at INFN Cagliari.*

(V550A) and the other with a 10 bits ADC (V550). The range was set in both modules to 1.5 V, which corresponds to 0.4 mV/ch in the first and 1.5 mV/ch in the second. The Sequencer sent the CLOCK, Track & Hold and CLEAR signals to the GAS64. For a detailed explanation of the readout system see section 6.3.2. A buffer amplifier with gain equal to 1, needed for the transmission of the analog multiplexed signal to the readout module, has been used.

Most of the test was performed with 80% Ar and 20% CO<sub>2</sub> but, as will be shown later, we crosschecked our results also with different values of the mixture.

To select the gas mixture (Ar-CO<sub>2</sub>) a system of two digital flowmeters and a digital controller was used. An overpressure of few mb inside the chamber was kept.

The DAQ system, running on Windows 98, was based on Labview 6i software [Lab6i].

The PC was connected to the VME crate by means of a PCI/MXI2 cable.

Root 3.0 [Root] software was used for the whole data analysis.

## 8.3 Data analysis

The test performed at INFN Cagliari with the <sup>90</sup>Sr source allowed us to study many prototype features. Unfortunately a resolution measurement was not possible, owing to the lack of an external tracking system.

An extensive study of the noise, the total charge induced on cathode planes and the number of hit strips for different strip dimensions in the same prototype has been done.

An efficiency study as a function of anode High Voltage and of few quencher different percentages in the gas mixture has been also performed.

### 8.3.1 Electronics noise

To have an idea of the contribution to noise from the various elements of the electronic chain we performed several runs as described in the following. We firstly measured the 10 bit ADC pedestal without source and with no cabled electronics. In fig. 8.9 the pedestal sigma versus the channel number is shown. A  $\simeq 0.1$  mean value is obtained. This is the ADC noise only.

We then repeated a data taking with GASSIPLEX connected, but not plugged onto the detector. Fig. 8.10 shows a sigma pedestal value, for ADC + GASSIPLEX,  $\simeq 0.5$  ADC channels.

It is therefore clear that the main contribution to noise, between these two, is given by GASSIPLEX chips, while the only ADC component is negligible (as illustrated in fig. 8.9).

Figure 8.9: *Sigma pedestal (in ADC channels) for the 10 bit ADC noise only.*

Figure 8.10: *Sigma pedestal (in ADC channels) of the 10 bit ADC + GASSIPLEX chips system.*

Finally we studied also the noise due not only to ADC and GASSIPLEX, but also to the cathode plane and particularly to strip dimensions. We made several runs, with the electronics plugged in, at 1650 V. For this study we used both 10 and 12 bit C-RAMS. The pedestal value is shown, for the two cathode planes, in fig. 8.11 (10 bit ADC C-RAMS) while in fig. 8.12 the sigma pedestal trend, for both bending and non bending plane, is reported.

The bending plane behaviour shows two different regions, one corresponding to small strips and the other to large strips. These induce a larger noise due to their larger area. The lowest recorded values correspond to channels not connected.

Results for the non bending plane are displayed in fig. 8.12 (bottom). Also in this plot a two region structure is clearly evident. In this plane the large strips sigma pedestal seems to be a slightly bigger than in the bending one.

To check if the oscillating trend shown by pedestals depends on strip dimensions we studied the correlation between sigma value and strip area. This study was performed with a 10 bit C-RAMS for both planes. On top of fig. 8.13 the results for bending plane are reported. Two distributions, corresponding to the two different strip x dimensions, are shown. Their sigma values are not so different one from each other and moreover the sigma spread, within each of them, is small. A little variation with the strip area and line length is shown, opposite to the previous prototype behaviour (section 7.1.1).

The same trend is shown by non bending plane. A little difference in sigma values, between the two planes, due to the slightly different strip areas, can be noticed.

## 8.4 Test with source setup

Due to some lack in readout electronic cards only a half detector has been equipped. 320 channels in the bending plane (5 GAS64 cards) and 128 in the non bending plane (2 GAS64 cards) were connected. Also 2 translation cards have been used.

Different chamber regions have been tested with the source (see fig. 8.14 for an example). A study of many features as a function of HV and for different gas proportions has also been done.

### 8.4.1 Charge distribution

For each event we evaluated the total charge, i.e. the sum of the charge induced on all the fired strips.

From online display it is possible to check the chamber region limited by the

Figure 8.11: *Pedestal value (in ADC channels) for the bending plane (top) and non bending plane (bottom).*

Figure 8.12: *Sigma of the pedestal (in 10 bit ADC channels) for the bending (top) and non bending plane (bottom). 1 channel corresponds to 625 electrons.*

Figure 8.13: *Sigma of the pedestal as a function of strip area for bending (top) and non bending plane (bottom). 1 ADC channel corresponds to 625 electrons.*

Figure 8.14:  $^{90}\text{Sr}$  source position in the bending plane large strip region.



source (see fig. 8.15) and possibly to exclude the charge on the strips out of this region. We will show later the effect of such a cut on some analysis results.

Figure 8.15: *Source position (in ADC channel) in bending and non bending plane, from online display.*

In the following, if not specified, we will call as *total charge* the charge induced only in the source region.

In fig. 8.16 the total charge distribution, fitted by a Landau function, is plotted for three High Voltage values. They refer to small strips in the bending plane (left) and non bending plane (right). In fig. 8.17 the same distributions are plotted for large strips.

The Landau peak value, as we can see from fig. 8.16 and 8.17, is strictly depending on HV. This correlation is displayed, for different HV values, in fig. 8.18. The results are reported for both bending and non bending plane small strips (top). Fig. 8.18 (bottom) displays the same study performed for large strips. In both cases the charge induced on bending and non bending plane is nearly the same. The charge for different strip dimension is very similar for low HV values (up to 1650 V, i.e. the standard working HV value). As the HV increases the

Figure 8.16: *Total charge distribution fitted by a Landau function for different HV values (left: bending plane, right: non bending plane).*

Figure 8.17: Total charge distribution fitted by a Landau function for different HV values (left: bending plane, right: non bending plane).

charge induced on small strips is more than on large strips. This behaviour is not yet completely understood.

### 8.4.2 Number of hits

The number of hit strips has been evaluated, without using any cluster-finding algorithm, for the bending and non bending plane small strips. The results are shown in fig. 8.19. As expected the mean value increases as the HV rises.

The same study for large strips has been done and in fig. 8.20 results are plotted. In this situation the mean hit value is lower than in the previous one. In fact, since the area of each strip is larger, the charge is distributed on average on less of them. The mean hit value as a function of HV is plotted in fig. 8.21. As explained before, this value is higher for small strips (fig. 8.21 top) than for large ones (fig. 8.21 bottom). As the HV increases the difference between bending and non bending plane becomes more significative.

## 8.5 Event selection and efficiency study

To estimate the background level in each run, we also checked how many strips, on average, give a signal out of the source zone. Fig. 8.22 shows a different behaviour for small and large strips as a function of HV. Few large strips (both in the bending and non bending plane) are out of range and the trend shown as a function of HV is very flat. In the small strip region instead this value grows up from  $\simeq 0.8$  ch (HV = 1400 V) to  $\simeq 4.4$  ch (HV = 1800 V) for the non bending plane (star symbol in the picture). The behaviour for small strips in the bending plane seems to be more regular, nevertheless its value is bigger than for large strips in the same plane.

The detector efficiency is defined like the ratio of the accepted events by the chamber to the number of triggers.

First of all we calculated the efficiency requiring, at least, one fired strip in the source region without any check on strips outside this area. Results are shown in fig. 8.23 for small (top) and large strips (bottom). In both pictures efficiency increases with the HV. From  $\simeq 1600$  V this value is approximately constant.

We calculated also the efficiency by accepting only events in which at least a strip is hit in the source region and no more than 2 are in the outside region in both bending and non bending planes.

The effect of this event selection is more evident for the detector efficiency in the small strip region (fig. 8.24, top). As already shown (fig. 8.22) the number of small strips outside the source region is not negligible and it increases as the HV increases. This number is instead very low for large strips and weakly depending

Figure 8.18: *Most probable value of total charge (ADC channels) as a function of High Voltage for bending (circle symbol) and non bending (star symbol) plane. On top: small strips, on bottom: large strips.*

Figure 8.19: *Number of hits in the bending (left) and in the non bending plane (right), for small strips.*

Figure 8.20: *Number of hits in the bending (left) and in the non bending plane (right), for large strips.*

Figure 8.21: Mean hit value as a function of High Voltage for bending (square) and non bending (star) plane. On top: small strips, on bottom: large strips.



Figure 8.22: Strips fired outside the source region in different HV runs for bending (square) and non bending (star) plane. On top: small strips, on bottom: large strips.

Figure 8.23: *Detector efficiency as a function of HV (no check on outside strips). On top: small strips, on bottom: large strips.*

on HV.

By requiring a maximum of 2 strips outside the source position the number of good events drops for small strips while it is almost constant for large ones. Such a cut therefore affects the efficiency behaviour for small strips, for High Voltage values, while it does not change the trend for large strips.

## 8.6 Gas study

We studied some prototype features by varying the CO<sub>2</sub> percentage (10 %, 20 %, 30 %). This study has been done without any check on the strips possibly fired outside the source region and only for small strips.

The Landau peak has been evaluated by fitting the total charge distribution by a Landau function for different HV values and for 3 gas mixtures. The results are illustrated in fig. 8.25 for bending plane (top) and non bending plane (bottom). As expected the most probable value of charge increases as the quencher percentage decreases. Also the number of hit strips becomes larger and larger, as shown in fig. 8.26 (top) for the bending plane and for the non bending plane (bottom). The anomalous behaviour shown at 1600 V is probably due to a non complete gas fluxing.

An efficiency study has also been done. In fig. 8.27 (top) results are reported. For a 90 % Ar - 10 % CO<sub>2</sub> a 100 % value is achieved also at low voltage values, while for the other gas mixtures the plateau region starts at about 1600 V.

If we now require the check (described in section 8.5) on strips hit outside the source region we obtain the results displayed in fig. 8.27 (bottom). In this situation the curve for the 90 % - 10 % mixture drops faster than the others, since the number of strips fired outside the source region is bigger. The mixture 70 % - 30 % has, instead, a small number of hit strips which are mostly concentrated in the source region. With the mixture 80 % - 20 % the number of strips hit outside the region delimited by the source is big only for 1800 V. The plateau remains nearly constant in the HV range 1550 V - 1750 V.

A gas mixture composed by 80 % Ar and 20 % CO<sub>2</sub> seems to be a good choice for what concerns total charge, number of hit strips and efficiency.

## 8.7 Main results of the test at CERN PS (June 2001)

After the study previously shown the prototype has been tested with a 7 GeV/c pion beam at CERN PS.

Figure 8.24: *Reconstruction efficiency as a function of HV for small (top) and large (bottom) strips, by requiring 2 hits outside the source region at maximum.*

Figure 8.25: *Most probable value of total charge on small strips for different HV values and quencher percentage.*

Figure 8.26: Mean number of hit strips for small strips for different HV values and quencher percentage (top: bending plane, bottom: non bending plane).

Figure 8.27: *Efficiency as a function of HV and quencher percentage without (top) and with (bottom) check on source region.*

The experimental setup and the readout system have been already described in details (see respectively section 6.3.1 and 6.3.2).

Figure 8.28: *Schematic view of the experimental set-up at CERN PS.*

The CEA Saclay prototype has been placed in front of the Cagliari prototype (fig. 8.28) and tested at the same time. The performances of the two prototypes have been compared, in particular for what concerns the noise. In fact the two detectors only differ for the thickness and material of the dielectric foil. In one case it is a layer of Nomex, 250  $\mu\text{m}$  thick and only the external skin is grounded (Cagliari prototype). In the other it is a 2 mm thick Nomex-air honeycomb foil and the two carbon skins are grounded (Saclay prototype).

In fig.8.29 the pedestal sigma behaviour in the bending plane is shown for both prototypes. As we can see the Saclay prototype sigma noise does not show any structure (fig. 8.29, right) while in the Cagliari chamber an increasing trend is clearly visible (fig.8.29, right) which probably indicates a poorer shielding of the second prototype.

In both cases the noise level is too high (about 3.5 ADC channels, which correspond to about 2200 electrons). This value is around 1 channel higher than that recorded in Cagliari lab (section 8.3.1) and could be attributed to a greater noise of the CERN experimental hall.

The resolution in both planes is affected by this high noise value, but it is critical above all for the bending plane, where a 100  $\mu\text{m}$  value is required. In fig. 8.30 the resolution in this plane (in the small strip region) as a function of High Voltage is displayed. The large noise value leads to unacceptable resolutions for this plane (around 190  $\mu\text{m}$  at best).

In the non bending plane the resolution is around 1 mm, as shown in fig. 8.31, and this value is below the required value ( $\sim 2$  mm).



Figure 8.29: *Pedestal sigma for Saclay (left) and Cagliari (right) prototypes. In this test we used a 12 bits CRAMS with 1.5 V range.*

Figure 8.30: *Resolution in the bending plane as a function of High Voltage (small strip region).*

Figure 8.31: *Non bending plane resolution as a function of High Voltage (small strips).*

The resolution in this plane is not so different for large and small strips, but the capability to identify the hit wire depends on the strip dimensions. In fact in the non bending plane it is possible to identify the hit wire on which the avalanche takes place by means of the cluster position. The probability for a good reconstruction of this position is only 75% for the 8.333 mm wide strips and 88% in the 7.143 mm case, in spite of what predicted by simulations [PRR01]. This last value will be therefore used in the final PCBs.

## 8.8 Summary

A small size prototype, made by only a PCB per cathode plane, has been assembled in Cagliari laboratories.

The previously tested assembly procedures and the reduced prototype dimensions simplified its building.

A preliminary test has been made on this detector by using a  $^{90}\text{Sr}$  source, allowing to study in Cagliari some prototype performances.

The 400  $\mu\text{m}$  PCB thickness seems to show a better rigidity and mechanical resistance to stress. It seems also to better isolate the frontplane from the backplane from the noise point of view. Only a little dependence of noise on strip dimensions has been observed, but no strong correlation with line length has been

shown.

A correlation between the Landau peak position and the HV has been illustrated. Nevertheless, in small strips the induced charge is more than in the large ones.

The number of hit strips increases as the High Voltage rises. There is a small difference between the charge induced in the two planes and it seems to become more evident as the voltage increases. The mean number of hit strips is nearly the same for small and large strips ( $HV \leq 1600$ ) but it stands out for larger voltage values.

The efficiency reaches a  $\simeq 100\%$  value for both small and large strips ( $HV \leq 1600$ ).

A study of some detector features as a function of different  $CO_2$  percentage in the gas mixture has been made. The standard Ar 80 % -  $CO_2$  20 % shows the best working properties for what concerns total charge, number of hit strips and efficiency.

The test at CERN PS put in evidence a too high measured noise which affects the resolution, allowing to achieve only  $190\ \mu m$  in the bending plane, while the resolution in this plane should be better than  $100\ \mu m$ .

An improvement has been achieved with a prototype equipped with the final electronics, as we will show in the next chapter, where the conclusions on this thesis will be eventually drawn.



## Chapter 9

# Last results and conclusions

In May 2001 a slat prototype of the largest size foreseen has been built at SUBATECH-Nantes and in-beam tested at CERN PS in June and October (fig. 9.1). This detector, 2400 mm long, was equipped with a version of the readout electronics almost final, based on MANU345 cards.

From a mechanical point of view the construction of this prototype allowed to refine the assembly procedure, now well tested in view of the final production of all the slat chambers.

From a physics point of view the main performances of the detector have been determined with an electronics configuration similar to the final one, though the electronics calibration has not yet been made.

Figure 9.1: *Test of the prototype at CERN PS.*

The prototype was made by 6 PCBs per cathode plane, the strip size was

$25 \times 5 \text{ mm}^2$  in the bending plane and  $7.143 \times 25 \text{ mm}^2$  in the non bending plane. The dielectric was a Nomex foil,  $250 \text{ }\mu\text{m}$  thick. The  $20 \text{ }\mu\text{m}$  wires this time were glued on special spacers.

The analog signal was elaborated by MANU cards. GASSIPLEX  $0.7 \text{ }\mu\text{m}$  chips were used as preamplifiers, filters and shapers instead of MANAS chips. A 12 bits ADC on board made the analog to digital conversion with a range up to  $3 \text{ V}$ <sup>1</sup>. The gas mixture was Ar (80%)-CO<sub>2</sub> (20%).

## 9.1 Study of the noise

The noise level measured during the test was between 1020 and 1400 electrons. The behaviour of the sigma pedestal for a MANU card in the bending plane and one in the non bending plane (64 channels each) is depicted in fig. 9.2.

Figure 9.2: *Sigma pedestal for a MANU of bending (left) and non bending (right) planes.*

The different behaviour of the noise in the two planes can be explained by considering the different connecting lines structure of the PCB in the two planes. In fact, in the bending plane long and short read-out strips are alternated, in the non bending plane they are divided into groups of 8 lines each with decreasing length, as reflected by the sigma pedestal trend.

This noise has been measured by linking all planes (carbon skins and strips) to a common ground, which has been later insulated by the general ground of the hall.

---

<sup>1</sup>This implies 1270 electrons per ADC channel.

## 9.2 Bending plane performances

The resolution in the bending plane as a function of High Voltage is shown in fig. 9.3.

Figure 9.3: *Resolution in the bending plane as a function of High Voltage.*

The flat region is between 1675 and 1750 Volts with a resolution below  $80\ \mu\text{m}$ , better than the required value of  $100\ \mu\text{m}$ .

### 9.2.1 Gain dependence on position

As already described in section 5.1 gain, in multiwire proportional chambers, depends in a critical way on geometrical parameters. It could change from point to point as a consequence of local mechanical variations, resulting in a large gain variation, which have to be avoided to not deteriorate the spatial resolution and reconstruction efficiency.

During the test we studied the detector response for 4 different positions in the same PCB. The four beam positions on the chamber are shown in fig. 9.4.

By fitting the charge curves for the 4 runs to a Landau function we obtained a MPV value for each run. By plotting these values versus the four positions we can see that the overall gain variation does not exceed a 14 % value (fig. 9.5). If

Figure 9.4: *Beam position on the chamber for 4 runs.*



we suppose that this gain change is entirely due to a gap fluctuation, we can see that it corresponds to  $100\ \mu\text{m}$  (section 5.1.2), a value well within tolerances.

Figure 9.5: *Gain as a function of the 4 positions in the PCB for bending plane.*

Correspondingly we evaluated the resolution in the bending plane. A good resolution value is achieved ( $\sim 80\ \mu\text{m}$ ) and a flat behaviour is observed (fig. 9.6). The gain variation therefore does not affect too much the resolution value.

### 9.2.2 Resolution for inclined tracks

In section 4.3 we saw that spatial resolution depends on the angle  $\alpha$  formed by the track with the  $z$  axis in a vertical plane. During the test 5 runs at a constant  $HV = 1750\ \text{V}$  were made by tilting the chamber from 0 up to 8 degrees.

In fig. 9.7 the behaviour of the bending plane resolution as a function of the vertical angles is shown.

As expected a deterioration of resolution is measured: for  $2^\circ$  it gets worse by the 2 % while at  $8^\circ$  inclination a worsening of 50 % is observed. At this acceptance angles in any case the particle hit density is low (fig. 3.1).

## 9.3 Conclusions and perspectives

The ALICE experiment, which will take place at LHC accelerator starting in 2007, will be devoted to the study of Quark Gluon Plasma signatures. It is a

Figure 9.6: *Bending plane resolution as a function of the four positions on the PCB.*

Figure 9.7: *Bending plane resolution as a function of chamber slope.*

complicated apparatus made by many sub-detectors.

This thesis has been mainly dedicated to the experimental study of the tracking system of the Muon Arm Spectrometer. It is a complicated ensemble of detectors based on multiwire proportional chambers which required and will require an intense phase of research and development before the assembly of final devices will be possible.

This phase is based on theoretical studies, simulations, and construction of prototypes to verify if the required physics performances are achieved.

In this thesis a simulation study of some detector features has been made. Well tuned programs like Garfield, Maxwell and Magboltz have been used to describe the slat chamber behaviour in particular conditions. This work has been important since some features are difficult to be studied experimentally.

The study of the gain variation as a function of several geometrical parameters gave us useful indications on the technical parameters and configurations to be adopted in the final detectors.

A study of the electric field near chamber edges (upper and lateral) has been made and helped us in the choice of edge wire configuration and on spacer shape. A study of gain near the border, which will be made in 2002 on a slat prototype, will help to check the validity of this study.

From the experimental point of view during the last years some prototypes have been designed, assembled and studied both at CERN and in Cagliari labs with a source. In this thesis three of them were considered.

The assembly technique for slat chambers must be carefully checked since mechanical tolerances are critical. Moreover, since the slat modules will be assembled in four laboratories (Cagliari, Nantes, Saclay, Gatchina), it is necessary to guarantee the same performances to the different series.

The construction of prototypes with different sizes, from one to six Printed Circuit per cathode plane, allowed to tune and refine the assembly procedure. In particular the gluing and closure of chambers have been validated.

Anode wires have been soldered at first and later glued. This procedure is faster and ensures a good electrical isolation between cathode planes and wires and an accurate wire positioning. The validity of this procedure has been also confirmed by simulations, which suggested the use of non gold plated wires to limit gain variations.

Three kinds of readout electronics (GAS-64 with  $1.5\ \mu\text{m}$  GASSIPLEX chips, GAS-64 with  $0.7\ \mu\text{m}$  GASSIPLEX chips, MANU345 with  $0.7\ \mu\text{m}$  GASSIPLEX chips) have been used to test the performances of prototypes.

In particular we studied:

- the noise and the correlation of sigma pedestal with strip length and dimensions;

- the gain, efficiency and resolution of both cathode planes as a function of High Voltage and of different gas mixtures;
- the gain at constant HV in different cathode plane points;
- resolution as a function of inclined tracks.

To summarize we report hereafter the main conclusions which can be drawn after several tests spanning three years.

The electronic noise is satisfactory (about 1020-1400 electrons) and it is almost independent on connecting lines length and strip dimensions. This study is very useful since the design of the final cathode planes is now in progress.

The gain as a function of High Voltage is linear in both planes, as expected in a multiwire chamber in proportional regime and the detector efficiency is higher than 95% in both planes. Best results are obtained with a gas mixture made by Ar (80 %) and CO<sub>2</sub> (20 %).

The spatial resolution in the bending plane is better than 80  $\mu\text{m}$ , lower than 100  $\mu\text{m}$  needed to separate heavy resonances. The non bending plane resolution is about 500  $\mu\text{m}$ , lower than the required value (2 mm).

The chamber gain, evaluated in 4 different PCB regions, is nearly constant. The maximum gain variation (14 %) corresponds at worst to 100  $\mu\text{m}$  gap difference, a value within planarity tolerances on carbon fiber panels that doesn't appreciably affect the spatial resolution.

The bending plane resolution as a function of the vertical chamber inclination deteriorates by 50 % for a 8° angle.

These results confirm therefore that satisfactory physics performances have been achieved.

During 2002 other prototypes will be assembled and tested to study the detector response of rounded shape slats, which will surround the beam pipe. A reduced size prototype of each Station will be also built to test the simultaneous response of all chambers.

The production of all detector elements (cathode planes, carbon fiber panels, spacers, ect) will start at the end of 2002 and the assembly of final detectors will begin in 2003.

# Bibliography

- [Abr99] Abreu et al. (NA50 coll.), Physics Letters B 466 (1999) 408
- [Abr00] Abreu et al. (NA50 coll.), “Evidence for deconfinement of quarks and gluons from the  $J/\Psi$  suppression pattern measured in Pb-Pb collisions at the CERN-SPS”, Physics Letters B 477 (2000) 28
- [Abr01] Abreu et al. (NA50 coll.), “The dependence of the anomalous  $J/\psi$  suppression on the number of participant nucleons”, CERN-EP-2001-069, Subm. to Phys. Lett. B
- [Adc01] K. Adcox et al. (PHENIX Collaboration), Phys. Rev. Lett. 86 (2001) 3500
- [AER] Aeroforme Internet Site <http://www.aeroforme.com/>
- [Alb95] T. Alber et al. (NA49 Collaboration), Phys. Rev. Lett. 75 (1995) no.21, pp.3814-3817
- [ALIAD] ALICE: The forward muon spectrometer, Technical Proposal Addendum 1, CERN/LHCC/96-32 LHCC/P3 Addendum 1 (1996)
- [ALITP] ALICE Technical Proposal CERN/LHCC 95-71 LHCC/P3 (1995)
- [And99] E. Andersen et al. (WA97 Collaboration), Phys. Lett. B449 (1999) 401
- [Ant00] F. Antinori et al. (NA57 Collaboration), CERN-EP-2000-002
- [Ant01] F. Antinori, Summer Student Lecture Programme 2001, CERN August 2001, <http://webcast.cern.ch/Projects/WebLectureArchive//a01/a01443s4t1/sync/f001.htm>
- [App98] H. Appelshauser et al. (NA49 Collaboration), Eur. Phys. Journ. C2 (1998) 661

- [App01] H. Appelshauser et al. (CERES Collaboration), “New results from CERES”, Quark Matter 01, Proc. Int. Conf. on Ultra-Relativistic Nucleus-Nucleus Collisions, Stony Brook, 2001
- [Arn00] R. Arnaldi, “Etude de la suppression du  $J/\Psi$  dans les collisions Pb-Pb au SPS du CERN en fonction de la centralite mesuree avec le calorimetre a zero degree”, Ph.D Thesis, Clermont-Ferrand University (2000)
- [Bac01] B. Back et al. (PHOBOS Collaboration), nucl-ex/0105011
- [Bal99] A. Baldisseri et al., “Pad segmentation for stations 4 and 5 of the ALICE Muon Spectrometer CPC’s” ALICE/99-37 Internal Note/DIM (1999)
- [Bal01] A. Baldisseri, “Status Report on Saclay activities”, ALICE International Collaboration Meeting on Dimuon Spectrometer, May 12-18 2001, Villasimius (Italy)
- [Bea98] I.G. Bearden et al. (NA44 Collaboration), Nucl. Phys. A 638 (1998) 103c
- [Bek97] H. Beker et al., “Multipurpose analog multiplexed read out system for pad/strip detectors: description and instruction manual”, CERN report, 24 January 1997
- [Bjo83] J. D. Bjorken, Phys. Rev. D 27 (1983) 140
- [Bra99] P. Braun-Munzinger et al., Phys. Lett. B 465 (1999) 15
- [Bre77] A. Breskin et al., “High accuracy, bidimensional read-out of proportional chambers with short resolution times”, Nucl. Instr. and Meth. 143 (1977) 29
- [Bro90] F.R. Brown et al., Phys. Rev. Lett. 65 (1990) 2491
- [Brun94] R. Brun et al., CERN Program Library Long Write-up W5013, GEANT Detector Description and Simulation Tool (1994)
- [Cad] Cadence Internet Site <http://www.pcb.cadence.com/>
- [Cel84] T.Celik, J.Engels and H.Satz, Z. Phys. C 22 (1984) 301
- [CERN] CERN Press Release,  
<http://press.web.cern.ch/Press/Releases00/PR01.00EquarkGluonMatter.html>
- [Cha68] G. Charpak et al., “The use of multiwire proportional counters to select and localize charged particles”, Nucl. Instr. and Meth. 62 (1968) 235

- [Cha73] G. Charpak and F.Sauli, “High-accuracy, Two-Dimensional Readout In Multiwire Proportional Chambers”, Nucl. Instr. and Meth. 113 (1973) 381
- [Cha79] G. Charpak et al., “High-accuracy localization of minimum ionizing particles using the cathode-induced charge centre-of-gravity read-out”, Nucl. Instr. and Meth. 167 (1979) 455
- [Che00] B. Chenys et al., “For a V0 detector dedicated to the  $pp \rightarrow 2 \mu + X$  physics in ALICE”, ALICE/00-30 Internal Note (2000)
- [Chi83] J. Chiba et al., “Study Of Position Resolution For Cathode Readout MWPC With Measurement Of Induced Charge Distribution”, Nucl. Instr. and Meth. A 206 (1983) 451
- [Chia01] E. Chiavassa et al., “Results from heavy ions experiments at the CERN SPS: from hadronic to deconfined matter”, Nuclear Physics B (Proc. Suppl.) 99 (2001) 237
- [Cho74] A. Chodos et al., Phys. Rev. D9 (1974) 3471
- [Ciba] Ciba-Geigy Internet Site <http://www.ciba.com/>
- [Cou99] P. Courtat et al., “A Full-scale prototype for the tracking chambers of the ALICE muon spectrometer. Part II-Electronics: Preamplifier, Read-out prototype”, IPN Orsay, IPNO 99-01 (1999)
- [Cou00] P. Courtat et al., “Station 3/4/5: Bus electronique”, IPN-Orsay/SEP (2000)
- [Cus97] J. P. Cussoneau et al., “Test of a MICROMEGAS detector for the Muon Tracking Chambers of ALICE”, ALICE/97-28, Internal Note/DIM (1997)
- [Cus98] J. P. Cussoneau et al., “An integration of MICROMEGAS based Muon Tracking Chambers in ALICE”, ALICE/98-54, Internal Note/DIM (1998)
- [Date] “ALICE DATE V3 User’s Guide”, ALICE Internal Note/DAQ 98-44 (1998)
- [Dia91] M. Dialinas, “Technologie des chambres a fils”, Internal Report LAL/RT 91-03 (1991)
- [Dia01] M. Dialinas, private communication (2001) “VNIIEF Status Report”
- [Dup] Dupont Internet site <http://www.dupont.com>

- [Eli01] D. Elia et al. (NA57 Collaboration), “Results on cascade production in lead-lead interactions from the NA57 experiment”, hep-ex/0105049
- [Esk94] K.J. Eskola et al., “Multiplicities for LHC Nuclear Collisions Using HERA Structure Functions”, Phys. Lett. B332 (1994) 191
- [Eng90] J.Engels et al., Phys. Lett. B252 (1990) 625
- [Fen95] H. Fenker et al., “Precision Interpolating Pad Chambers”, Nucl. Instr. and Meth. A 367 (1995) 285
- [Fil01] K. Filimonov et al., “New Results on Pb-Au Collisions at 40 AGeV from the CERES/NA45 Experiment”, nucl-ex/0109017
- [Gar] R. Veenhof, “Garfield, simulation of gaseous detectors”  
<http://consult.cern.ch/writeup/garfield/>
- [Gat79] E. Gatti et al., “Optimum Geometry For Strip Cathodes Or Grids in MWPC For Avalanche Localisation Along The Anode Wires”, Nucl. Instr. and Meth. 163 (1979) 83
- [GEP] General Plastics Internet Site <http://www.geoplastics.com/>
- [Ger99] V. Gertsenstein et al., “Stations 4 and 5 of the ALICE Muon Spectrometer: Modular Approach” ALICE/99-41 Internal Note/DIM (1999)
- [Gol60] G. Goldhaber et al., Phys. Rev. 120 (1960) 300
- [HAM] Hameg Internet site <http://www.hameg.de>
- [Ham56] R. Hambury-Brown and R. Q. Twiss, Nature 178 (1956) 1046
- [Hee] I. Smirnov “Heed: Interactions of particles with gases”  
<http://consult.cern.ch/writeup/heed/>
- [Hei] U. Heinz, hep-ph/9902424
- [Hein] U. Heinz and M. Jacob, hep-ph/0002042
- [Hei99] U. Heinz, Proceedings of Quark Matter 1999, Turin (Italy), Nucl. Phys. A661 (1999)
- [Hei00] U. Heinz and M. Jacob,  
<http://cern.web.cern.ch/CERN/Announcements/2000/NewStateMatter/science.html>
- [HMPID] ALICE High Momentum Particle Identification Detector Technical Design Report, CERN/LHCC 98-19, ALICE TDR 1 (1998)



- [Kac99] Kaczmarek O. et al., “Heavy Quark Potentials in Quenched QCD at High Temperature”, hep-lat/9908010
- [Kar] F. Karsch, hep-lat/9909006
- [Kha99] L. Kharmandarian “Etude de chambres de trajectoire du spectromètre dimuons de l’expérience ALICE auprès du LHC”, Ph.D. Thesis, IPN Orsay, IPNO-T 00-02 (1999)
- [Khar96] D. Kharzeev and H. Satz, Phys. Lett. B 366 (1996) 316
- [Kho94] N. Khovansky et al., “Spatial resolution of profile-based detectors with external pick-up strips”, Nucl. Instr. and Meth. A 351 (1994) 317
- [Kow85] T. Z. Kowalski, Nucl. Instr. and Meth. in Phys. Res. A234 (1985) 521
- [Has81] P. Hasenfratz et al., Phys. Lett. 95B (1981) 199
- [ITS] ALICE Inner Tracking System Technical Design Report, CERN/LHCC 99-12, ALICE TDR 4 (1999)
- [Lab6i] Labview 6i Internet Site  
<http://digital.ni.com/productpages/nilabview.nsf/main?readform>
- [Lan44] L. Landau, J. Phys. (USSR) 8 (1944) 201
- [Lee95] T. D. Lee, “RHIC and QCD: an overview”, Nucl. Phys. A590 (1995) 11c
- [Len99] B. Lenkeit, Proceedings of Quark Matter 1999, Turin (Italy), Nucl. Phys. A661 (1999) 23c
- [Leo87] W. R. Leo, “Techniques for Nuclear and Particle Physics Experiments”, Springer-Verlag (1987)
- [LHC] “Large Hadron Collider Internet Site”  
<http://lhc.web.cern.ch/lhc/general/gen-info.htm>
- [Li95] G. Li et al., Phys. Rev. Lett. 75 (1995) 4007
- [Luma] Luma Metall Internet Site <http://www.luma-metall.se>
- [Mag] S. Biagi, “Magboltz: Transport of electrons in gas mixtures”  
<http://consult.cern.ch/writeup/magboltz/>
- [Mat86] T. Matsui and H. Satz, Phys. Lett. B 178 (1986) 416
- [Maw93] R.D. Mawhinney, Nucl. Phys. B (Proc. Suppl.) 30 (1993) 331

- [Max] “Maxwell Field Simulator” <http://wwwinfo.cern.ch/ce/ae/Maxwell/ansoftem.html>
- [MUO] Dimuon Forward Spectrometer Technical Design Report, CERN/LHCC 99-22, ALICE TDR 5, 13 August 1999
- [MUOAD] Dimuon Forward Spectrometer Addendum, CERN/LHCC 2000-046, Addendum 1 to ALICE TDR 5, 15 December 2000
- [N471] CAEN N471 Internet Site <http://www.caen.it/nuclear/product.asp?id=240>
- [NA60] “NA60: Study of Prompt Dimuon and Charm Production with Proton and Heavy Ion Beams at the CERN SPS”, NA60 Proposal, CERN-SPSC-2000-010 ; SPSC-P-316. - Geneva : CERN , 7 Mar 2000
- [Ors01] F. Orsini and P. Hardy, private communication.
- [Orsi01] F. Orsini, “Stations 3-4-5 : Status report on Cooling and Frames design”, ALICE International Collaboration Meeting on Dimuon Spectrometer, May 12-18 2001, Villasimius (Italy)
- [Pei99] T. Peitzmann et al., Nucl. Phys. A 661 (1999) 191c
- [PHOS] ALICE PHOton Spectrometer Technical Design Report, CERN/LHCC 99-4, ALICE TDR 2 (1999)
- [PMD] ALICE Photon Multiplicity Detector Technical Design Report, CERN/LHCC 99-32, ALICE TDR 6 (1999)
- [PRR01] Production Readiness Review of Slat 3,4 and 5 (9th November 2001)
- [Raf82] J. Rafelski et al., Phys. Rev. Lett 48 (1982) 1066
- [Rap97] R. Rapp et al., Nucl. Phys. A 617 (1997) 472
- [Rit61] D. Ritson, “Techniques of high-energy physics” Interscience, New York (1961)
- [Root] The ROOT System Home Page <http://root.cern.ch/>
- [San99] J.C. Santiard et al., “The GASSIPLEX 0.7-2 Integrated Front-End Analog Processor for the HMPID and Muon Tracker of ALICE’, LEB99, CERN/LHCC 99-033, 431 (1999)
- [Sau77] F. Sauli, “Principles of operation of multiwire proportional and drift chambers”, CERN Yellow Report 77-09 (1977)

- [Shu92] E. Shuryak, “Two-stage equilibration in high energy heavy ion collisions”, Phys. Rev. Lett. 68 (1992) 3270
- [Sta99] J. Stachel, Nucl. Phys. A654 (1999) 119c
- [SY1527] CAEN SY1527 Internet Site <http://www.caen.it/nuclear/syproduct.asp?id=122>
- [TOF] ALICE Time Of Flight Technical Design Report, CERN/LHCC 2000-12, ALICE TDR 8 (2000)
- [Tom] B. Tomasik et al., nucl-th/9907096
- [Tou01] A. Tournaire, private communication (2001)
- [Tow47] J. Townsend, “Electrons in gases”, Hutchinson, London, 1947
- [TPC] ALICE Time Projection Chamber Technical Design Report, CERN/LHCC 2000-001, ALICE TDR 7 (2000)
- [TRD] ALICE Transition Radiation Detector Technical Design Report, CERN/LHCC 2001-021 , ALICE TDR 9 (2001)
- [V550A] CAEN V550A Internet site <http://www.caen.it/nuclear/product.asp?id=166>
- [V551B] CAEN V551B Internet site <http://www.caen.it/nuclear/product.asp?id=60>
- [Web01] F. Weber, J. Phys, G 27 (2001) 465
- [Wig] “Energy loss of particles in dense matter-calorimetry” Proceedings / Ed. by C. W. Fabjan and J. E. Pilcher, World Sci., Singapore, 1988 - 41- 14
- [Won94] C. Y. Wong, “Introduction to High-Energy Heavy-Ion Collisions”, World Scientific Publishing (1994)
- [Wur97] R. Wurzinger et al., “Monte Carlo studies on Cathode Strip/Pad Chambers for the ALICE Di-Muon Arm”, ALICE Internal Note/97-10 DIM (1997)
- [ZDC] ALICE Zero Degree Calorimeter Technical Design Report, CERN/LHCC 99-5, ALICE TDR 3 (1999)
- [Zhu94] D. Zhu, Nucl. Phys. B (Proc. Suppl.) 34 (1994) 286